Photodynamic therapy using morpholine substitutedporphyrins in the presence of cancer specific molecules linked to graphene quantum dots

By

Ngwanabjala Bridged Magaela

A thesis submitted in fulfilment of the requirements for the degree of

MASTER OF SCIENCE

AT

RHODES UNIVERSITY

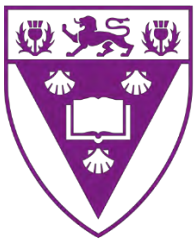

RHODES UNIVERSITY

Where leaders learn

December 2022

Acknowledgements

I would like to express my deepest appreciation to my supervisor Distinguished Professor Tebello Nyokong, thank you for all the guidance and support.

Special thanks to my mentors; Dr Refilwe Matshitse and Dr Muthumuni Managa you guys have made this journey so easy for me. Thank you to Miss Gail Cobus for all the administrative work and support. My gratitude also goes to Dr B Babu, S22 colleagues, Rhodes university, also Mintek and Desmond Goddard for funding.

I am also grateful for my family and friends who supported me throughout this journey. My mom Mamela Magaela and my grandmother Makgwale Manyaka, your prayers kept me going and your support is what kept me pushing “kea leboga ba bina phuti”.

Abstract

This thesis reports on the synthesis, characterization, photophysiochemical properties of morpholine substituted symmetrical and asymmetrical porphyrins. The synthesized porphyrins are conjugated to cancer selective biomolecules (folic acid and biotin) which are linked to nitrogen doped graphene quantum dots, as potential photosensitizers for photodynamic therapy (PDT). The symmetrical morpholine porphyrin complexes **2** (Sn(IV) 5,10,15,20 tetra-4-morpholinyl porphyrin) and **3** (Zn 5,10,15,20 tetra-4-morpholinyl porphyrin) had the same substituent but different central metals, and they were both conjugated to biotin decorated nitrogen doped graphene quantum dots (B-NGQDs), however complex **2** (Sn(IV)5,10,15,20 tetra-4-morpholinyl porphyrin) was conjugated to B-NGQDs through an ester bond and complex **3** (Zinc 5,10,15,20 tetra-4-morpholinyl porphyrin) through π-π stacking. The effect of asymmetry was studied by comparing complex **3** (Zn 5,10,15,20 tetra-4-morpholinyl porphyrin) and complex **5** (Zn 5- bromophenyl-10-15-20-(tris-4-morpholinyl) porphyrin). Complex **5** (Zn 5- bromophenyl-10-15-20-(tris-4-morpholinyl) porphyrin) was an asymmetric porphyrin with morpholine and bromine as substituents. It was observed that asymmetry enhances singlet oxygen quantum yield and PDT activity. It was alsoobserved that folic acid is a better targeting biomolecule when compared to biotin, and this was studied by comparing complex **3** conjugated to B-NGQDs and complex **3** conjugated to folic acid decorated nitrogen doped graphene quantum dots (FA-NGQDs). **3**-FA-NGQDs had a better cellular uptake and PDT activity.

Table of contents

List of abbreviations

B-NGQDs	Biotin decorated nitrogen doped graphene quantum dots
DLS	Dynamic light scattering
EDX	Energy dispersive X-ray spectroscopy
FA-NGQDs	Folic acid decorated nitrogen doped graphene quantum dots
FT-IR	Fourier-transform infrared spectroscopy
HOMO	Highest occupied molecular orbitals
ISC	Intersystem crossing
LED	Light-emitting diode
LUMO	Lowest unoccupied molecular orbitals
MALDI-TOF	Matrix-assisted laser desorption ionization- Time of flight
MCF-7	Michigan Cancer Foundation- 7
MW	Microwave
PDT	Photodynamic therapy
PS	Photosensitizer
PDI	Polydispersity index
^{1}H-NMR	Proton Nuclear Magnetic Resonance
ROS	Reactive oxygen species
RT	Room temperature
TCSPC	Time Correlated Single Proton Counting

TEM	Transmission electron microscope
UV-Vis	Ultraviolet-visible spectroscopy
XPS	X-ray photoelectron spectroscopy
XRD	X-ray powder diffraction

List of symbols

α	Alpha
β	Beta
τ_F	Fluorescence lifetime
ϕ_F	Fluorescence quantum yield
ε	Molar extinction coefficient
*S	Singlet excited state
S_0	Singlet ground state
ϕ_Δ	Singlet oxygen quantum yield
T_3	Triplet excited state
τ_T	Triplet lifetime
λ	Wavelength
ζ	Zeta potential

Problem statement

Photodynamic therapy (PDT) has been developed over the past decades as an alternative treatment for cancer, as it has many advantages compared to traditional therapies like chemotherapy **[1]**. This technique requires a photosensitizer (e.g. porphyrins), visible light of the appropriate wavelength to produce reactive oxygen species that eradicate diseased cells

In this thesis, porphyrins will be conjugated to nitrogen doped graphene quantum dots decorated with cancer selective biomolecules (folic acid and biotin) with the aim of reducing aggregation, enhancing solubility and physicochemical characteristics. At present, PDT is being tested in the clinics to treat cancers of the head and neck, brain, lung, pancreas, breast, prostate, and skin **[2]**. However, in this thesis PDT will be tested on Michigan Cancer Foundation -7 (MCF-7) breast cancer line.

CHAPTER 1

INTRODUCTION

1.1 Photodynamic therapy (PDT) background

Photodynamic therapy (PDT) is a minimally invasive treatment modality for diseased cancer cells, which uses laser light of appropriate wavelength (ideally at the maximum absorption of the photosensitizer), and a viable photosensitizer (PS) (such as porphyrin) to generate cytotoxic reactive oxygen species (ROS, including singlet oxygen) that eradicate diseased cells **[3, 4].** A good PS for PDT must possess the following properties: minimum dark toxicity, be able to generate singlet oxygen and other ROS, be selective to cancer and have strong absorption with high extinction coefficient in the red/ near infrared region of the electromagnetic spectrum (600-800 nm) to allow deeper tissue penetration by light **[5]**.

The mechanism behind porphyrin photosensitization during PDT is shown **Fig. 1.1** The PS is introduced to the tumour cells, followed by irradiation with light of appropriate wavelength (at λ_{max} of the PS). Upon the irradiation, the PS in the ground state (S_o) absorbs energy to occupy the first excited state ($^*S_1$).

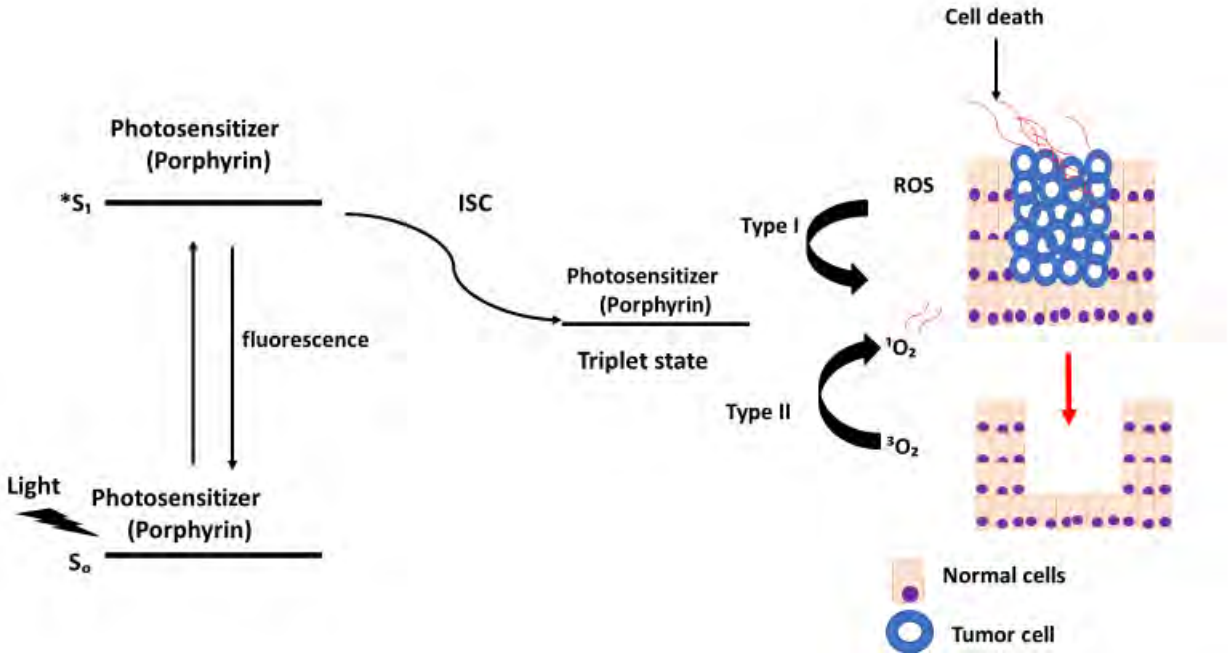

Fig. 1.1. Schematic illustration of photodynamic therapy on cancer cell. S_0 ground state, $*S_1$ first excited state, ISC = intersystem crossing, ROS = reactive oxygen species, $^1O_2$ singlet oxygen, $^3O_2$ ground state molecular oxygen.

The PS in the $*S_1$ may fluoresce back to S_o or may undergo Intersystem crossing (ISC) to occupy triplet state. The PS in triplet state may generate ROS through either type I or type II reactions. Type I reaction involves direct transfer of electron or proton from the PS or biomolecule in the triplet state to an oxygen molecule which results in the formation ROS. Type II reaction involves the transfer of energy from PS in the triplet state to the ground state molecular oxygen ($^1O_2$) resulting in the generation of singlet oxygen. Type II is assumed for PDT. In this work porphyrins will be used as photosensitisers.

1.2 Porphyrins

1.2.1 Background

The word porphyrin is derived from Greek porphura meaning purple **[6]**, and in 1912 the first structure of porphyrin was proposed by Küsher **[7]**. A porphyrin is a heterocyclic macrocyclic organic compound that is made of 4 pyrroles that are joined at their alpha (α) carbon atom by methane bridge (=CH-), as shown in **Fig. 1.2.** There are a total of 26 π electrons in porphyrins, of which an extended conjugated 18 π-electrons form a planar continuous system responsible for its aromatic behaviors **[8]**. Porphyrins are stable molecules that can coordinate metals. There are different types of substitution points on a structure of a porphyrin (**Fig. 1.2**), the β- α, and meso positions.

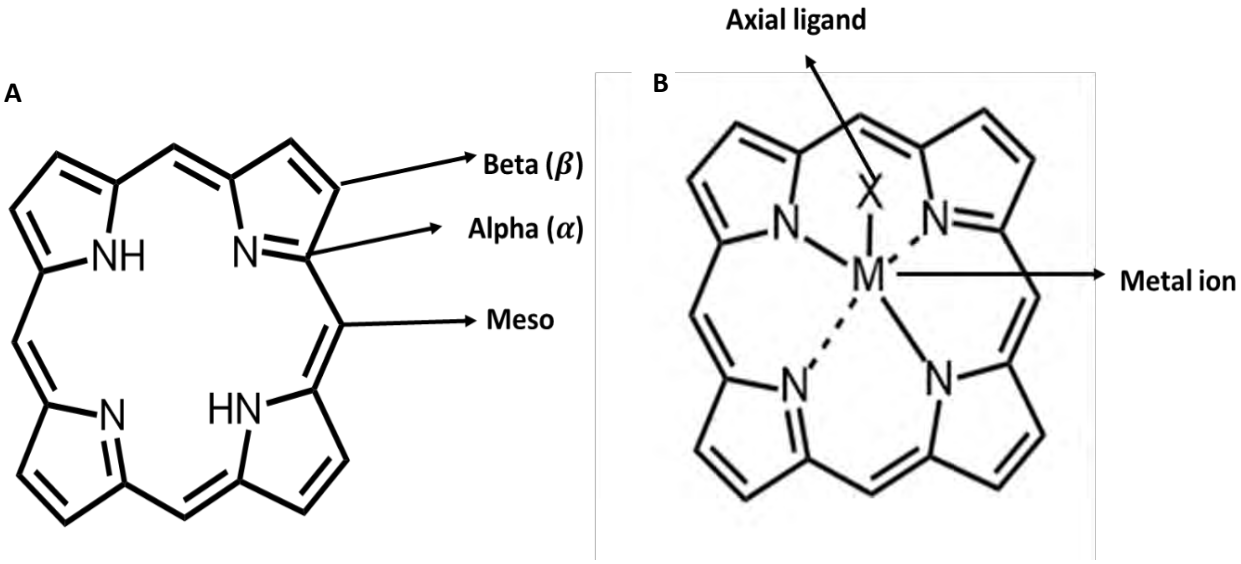

Fig. 1.2. Schematic representation of (A) free base porphyrin macrocycle with beta (β), alpha (α) and meso structural positions and (B) metalated macrocycle with an axial ligand.

The β- substituted porphyrin closely resemble naturally occurring porphyrins, α and the meso substituted porphyrin have no direct biological counterparts but have found wide applications as biomimetic models and as useful components in material chemistry **[9]**. The choice of substituent on a porphyrin depends on the application. Synthetic porphyrins can be used for clinical applications such as in PDT and photodynamic antibacterial chemotherapy (PACT)

agents **[10]**, in catalysts for bleaching of industrial dyes **[11]**, and as protective agents in nonlinear optical limiting, etc **[12]**. In this study novel morpholine porphyrins are employed for PDT to address the issues associated with specificity and selectivity of porphyrins.

1.2.2 Synthesis

There are several methods for synthesising porphyrins which will be discussed below and are shown in **Scheme 1.1**.

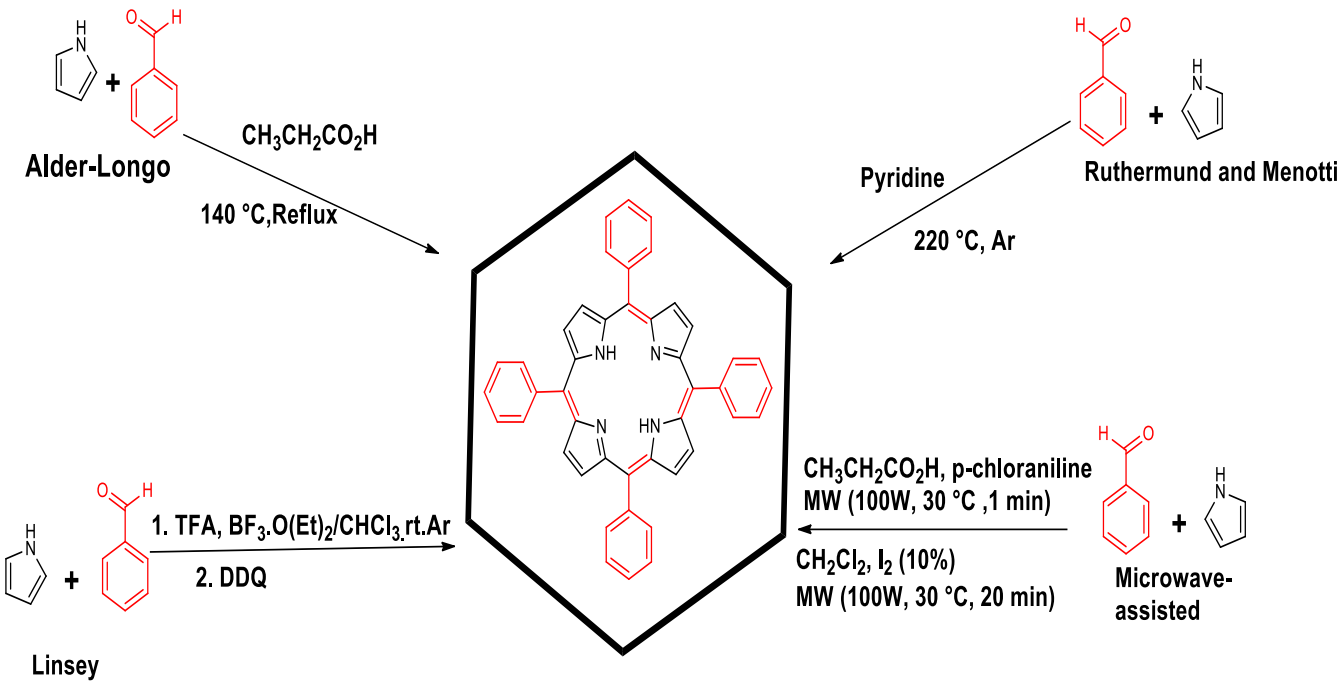

Scheme 1.1. Schematic representation of synthesis of a free-base porphyrin using different methods under different reaction conditions; MW = microwave, r.t. = Room temperature, Ar = Argon, TFA = Trifluroacetic acid, DDQ = 2,3-dichloro-5,6-dicyanobenzoquinone.

1.2.2.1 Rothermund and Menotti

In 1935 Ruthermund and Menotti were the first to synthesize meso-substituted porphyrin by reacting pyrrole with benzaldehyde at high temperature for 24 h **[13,14]**. The conditions of this synthesis resulted in low yields (approximately 10%).

1.2.2.2 Adler and Longo

To overcome the low yield challenge, in mid-1960's Adler and co-workers modified the Ruthermud reaction by allowing the pyrrole and benzaldehyde to react for 30 min in refluxing propanoic acid (141 ℃) in air **[15,16]**. This resulted in porphyrin yields of up to 20%, however not all types of aldehydes can be used with this method as some aldehydes are sensitive to acids. Aldehydes that had acid sensitive functional groups like hydroxyl, thiol and amino group did not form desired product with this method **[17]**. This method was used in this thesis to synthesize a symmetric porphyrins.

1.2.2.3 Lindsey and co-workers

Lindsey and co-workers developed the synthesis of porphyrin under mild conditions that can accommodate aldehydes with acid sensitive functional group **[18]**. In this method equal amounts of pyrrole and benzaldehyde are employed in the presence of acid catalyst usually trifluoroacetic acid (TFA) or boron trifluoride etherate ($BF_3.OEt_2$) and using dichloromethane as a solvent at room temperature under an inert atmosphere to form porphyrinogen intermediate. The porphyrinogen intermediate is converted to a stable aromatic porphyrin by an addition of oxidant normally *p*-chloranil or 2,3-dichloro-5,6-dicyno-1,4-benzaquinone (DDQ) **[19]**. This method was in this thesis to synthesise an asymmetric porphyrin.

1.2.2.4 Microwave-assisted and other methods

Zurroaki and co-workers developed microwave assisted synthesis for meso substituted porphyrins. This method is performed by reacting pyrrole, benzaldehyde, in dichloromethane (DCM) in 10% molar equivalent of iodide in a microwave, followed by addition of p-chloranaline **[20]**. The method resulted in an increased of yield (approximately 47%) and decrease in reaction time **[21]**. Various microwave-assisted and solvent-free synthetic procedures have been reported and possess relative high yields within a short period of time without condensation or distillation processes **[21,22].**

1.2.2.5 Synthetic methods employed in this thesis

Symmetrical meso substituted porphyrins are popular and easy to prepare, and the general synthetic route involves condensation of pyrrole in the presence of the desired aldehyde to form the tetra-substituted porphyrin (symmetrical porphyrin). In this work Alder-Longo method was employed for synthesis of symmetric porphyrin. Asymmetrical meso substituted porphyrin follows the same synthetic route as the symmetric porphyrin but employs two types of aldehydes (A and B) and pyrrole in **Scheme 1.2**. The molar ratios of the two aldehydes usually used are 1:3 (A: B) **[23,24]**, this type of molar ratio reduces the probability of forming symmetrical porphyrin. However, there is a probability of forming six porphyrin derivatives (**Scheme 1.2.**) when using this molar ratio, but various separation techniques such as column chromatography can be used to extract the porphyrin of interest from the crude product. In this work, 1:3 molar ratio of aldehydes was used to synthesise meso substituted asymmetrical porphyrin. Lindsey method was employed in this work to synthesise asymmetric substituted porphyrin.

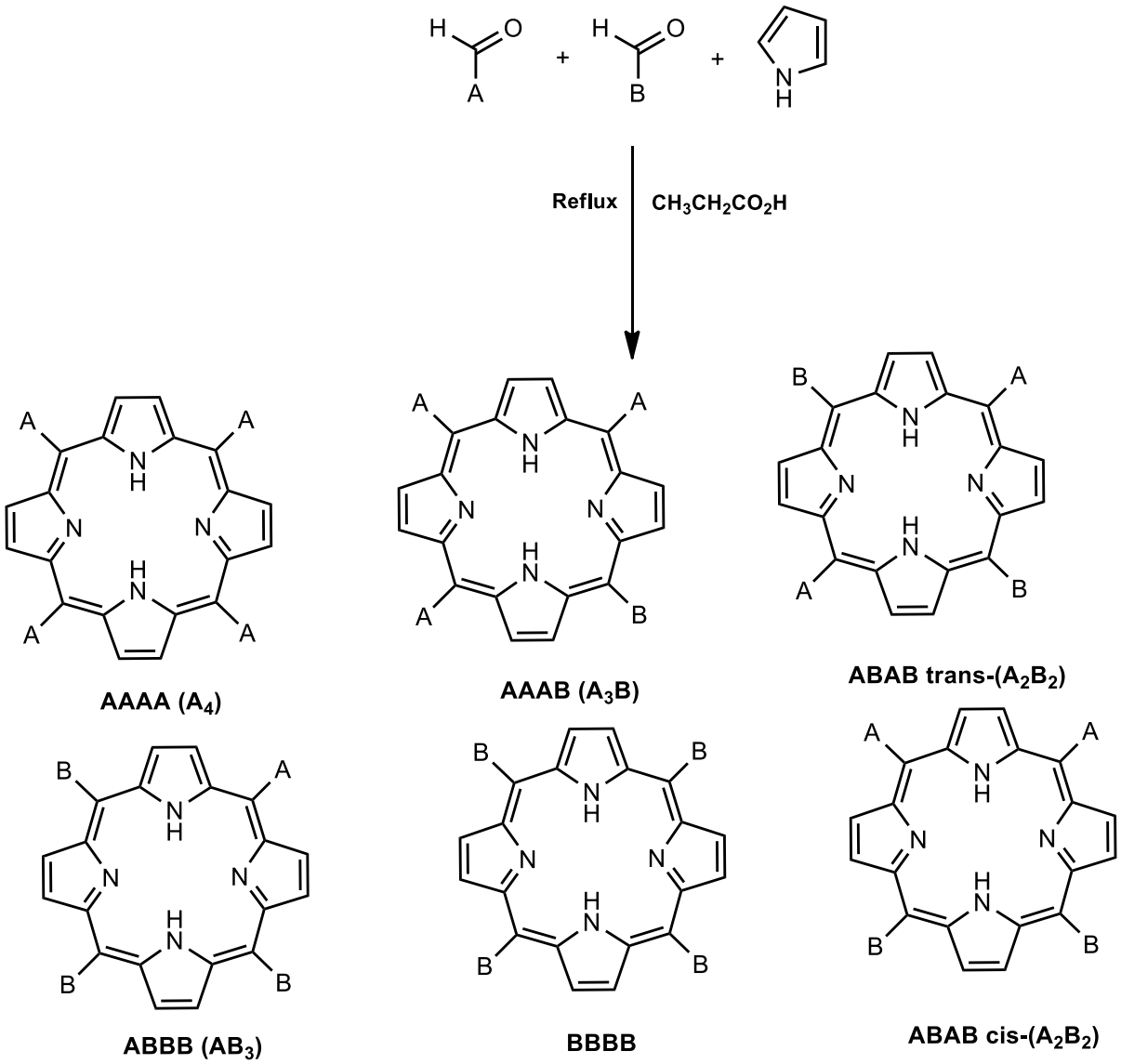

Scheme 1.2. General types of asymmetric porphyrins and their analogues

1.2.3 Electronic absorption spectroscopy

The UV-visible spectra of porphyrins consist of two different regions.

Porphyrins are characterized by two types of bands the Soret (B) band and Q bands. The absorption of Soret band ranges from 380-500 nm. The Q-bands show peaks in the range 500-700 nm. In the presence on central metal the four Q bands of free base porphyrin collapse and merge to two **[25].** The typical UV-Visible absorption spectrum of a porphyrin is represented by the **Fig 1.3** (A).

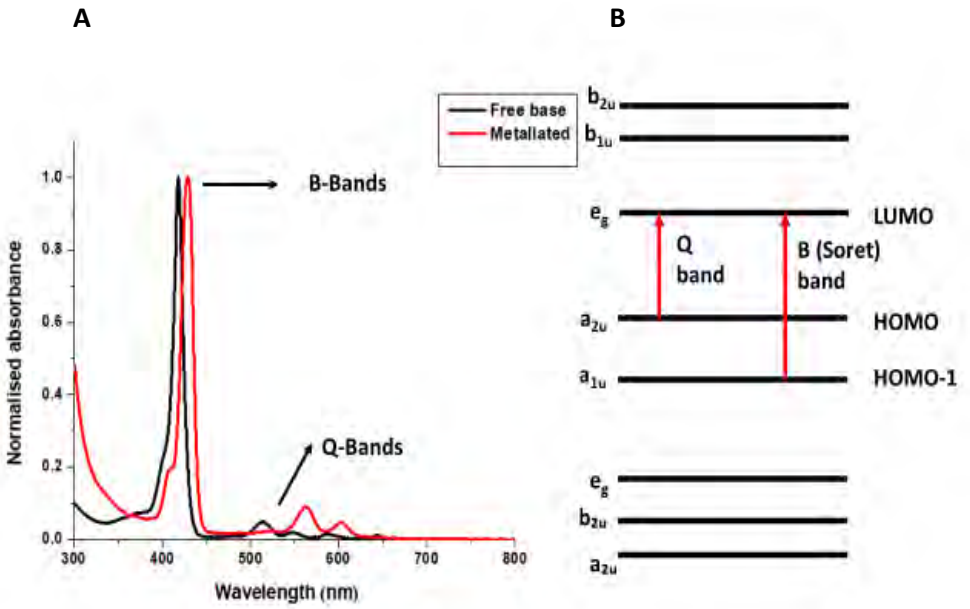

Fig. 1.3 UV-Visible spectra of a free base and metallated porphyrin (A) and (B) electronic transitions showing the origin of B (soret) and Q band of porphyrin.

According to Gouterman's theory **Fig 1.3**, (B), absorption bands in porphyrins are due to transitions between two highest occupied molecular orbitals (HOMOs), and lowest unoccupied molecular orbital (LUMO). The Soret band is from a_{1u} to e_g, and the Q band from a_{2u} to e_g **[26]**.

1.2.4 Photophysical and photochemical parameters of porphyrins

Photophysical and photochemical properties are important in determining the potential applicability as PS for PDT.

1.2.4.1 Fluorescence quantum yield and lifetime

The fluorescence quantum yield (ϕ_F) can be defined as the ratio of the number of photons emitted through fluorescence to the number of photons absorbed **[27,28] Equation 1.1**.

$$\phi_F = \frac{\text{number of photons emmited}}{\text{number of protons absorbed}} \qquad \textbf{Equation 1.1}$$

However, in this work a comparative method (**Equation 1.2**) was used to determine fluorescence quantum yields as reported in literature **[29]**, using zinc tetraphenylporphyrin (ZnTPP) as a standard with (ϕ_F^{std} = 0.303) in DMSO **[30]**.

$$\phi_F = \phi_F^{Std} \times \frac{F\, A^{std} n^2}{F^{std} A\, (n^{std})^2} \qquad \textbf{Equation 1.2}$$

Where ϕ_F^{std} is the fluorescence quantum yield of the standard, F and F^{std} are the areas under the fluorescence curve for sample and standard, respectively. A and A^{std} are the absorbance of the sample and standard, respectively. n and n^{std} are the refractive indices of solvent used for sample and standard, respectively. Fluorescence lifetimes (τ_F) can be defined as the average time the excited photon takes to relax back to the ground state through fluorescence. τ_F values were determined using time-correlated single photon counting (TCSPC).

1.2.4.2 Singlet oxygen

The magnitude of singlet oxygen quantum yield (ϕ_Δ) depends on the efficiency of molecule to transfer the absorbed energy to ground state molecular oxygen (^1O) to generate singlet oxygen ($^1O_2$). Singlet oxygen is one of the most reactive intermediates involved in chemical and biochemical process of various reactions and is responsible for light induced oxidative destruction of malignant cells **[31]**.

In this work, the chemical method was used for the determination of ϕ_Δ, using 9,10-dimethylanthracene (DMA) as a quencher. The ϕ_Δ was calculated using **Equation (1.3) [32]**, using ZnTPP (ϕ_Δ= 0.53) as a standard **[33]**.

$$\phi_\Delta = \phi_\Delta^{Std} \times \frac{B.I^{Std}}{B^{Std}.I} \qquad \textbf{Equation 1.3}$$

where ϕ_Δ and ϕ_Δ^{Std} are the singlet oxygen quantum yield of the sample and standard respectively, B and B^{Std} are the photobleaching rates of the singlet oxygen quencher (DMA) in the presence of the photosensitizer (porphyrin) and the standard, respectively. I and I^{Std} are the rates of light absorption by the sample and standard, respectively.

1.2.4.3 Triplet lifetimes (τ_T)

Triplet lifetimes (τ_T) can be defined as the amount of time the excited molecules exist in the triplet excited state. In this work, τ_T were obtained by exponential fitting the kinetic curves using the ORIGIN 8 professional software.

1.2.5 Different ways of enhancing photo-physiochemical properties

Several modifications can be done on porphyrins to enhance their photo-physiochemical properties.

1.2.5.1 Central metal

The use of central metals such as (tin, zinc, indium, and etc.) can improve the photo-physiochemical properties through heavy atom effect which stimulate intersystem crossing to triplet excited state **[34]**. In this work, Sn and Zn are employed as central metals.

1.2.5.2 Substituents

The substituents on the porphyrin also contribute to the photo-physiochemical properties, substituents such as bromide and sulfur are reported to have internal heavy atom effect and they increase the rate of intersystem crossing (ISC) which leads to higher singlet oxygen quantum yields **[35]**. In this work Br is employed in the asymmetric porphyrin to enhance ISC.

1.2.5.3 Asymmetry

Asymmetrically substituted porphyrins also result in higher singlet oxygen quantum yield as the asymmetry enhances triple state population **[36]**. Asymmetry enhances intersystem crossing and consequently improve singlet oxygen quantum yields, hence asymmetrical porphyrin is employed in this thesis.

1.2.5.4 Use of carbon nanomaterials

Carbon nanomaterials such as graphene quantum dots (GQDs) can generate singlet oxygen and other ROS **[37]**, and they also contain electron donating groups which are known to increase the intersystem crossing in porphyrins-like complexes **[38]**. In this work carbon based nitrogen doped graphene quantum dots (NGQDs) nanoparticles are employed with porphyrins for PDT.

1.2.6 Porphyrins used in this work

All the porphyrins that were synthesized and used in this work are outlined in **Table 1.1** and will be discussed below.

Table 1.1: Porphyrins employed in this work for PDT

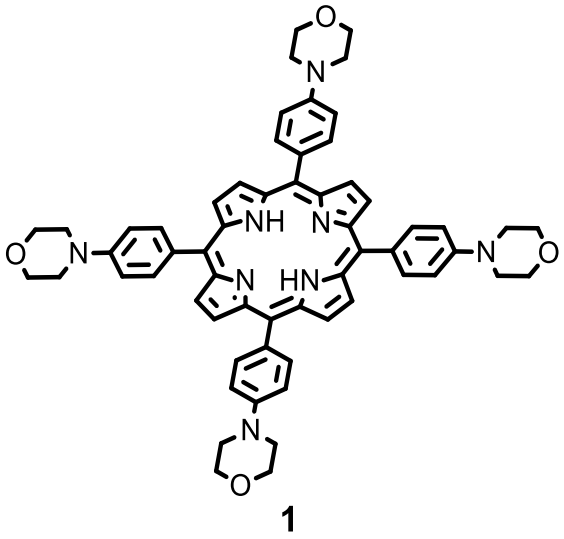 **1** **New**	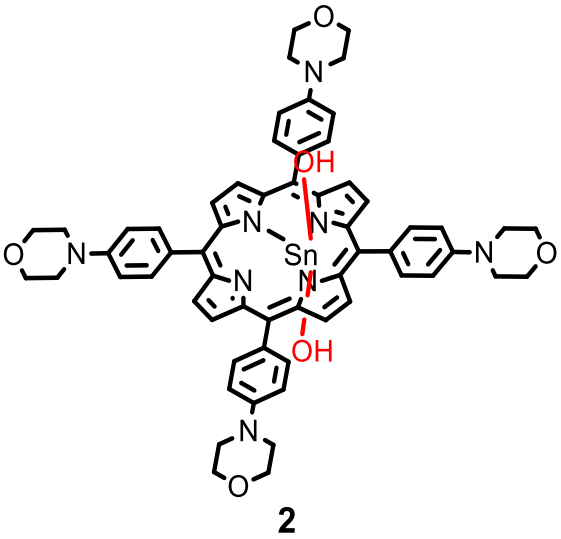 **2** **New** Physicochemical and PDT
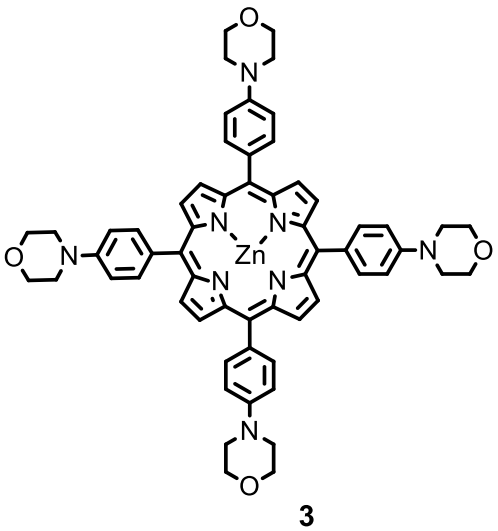 **3** **New** Physicochemical and PDT	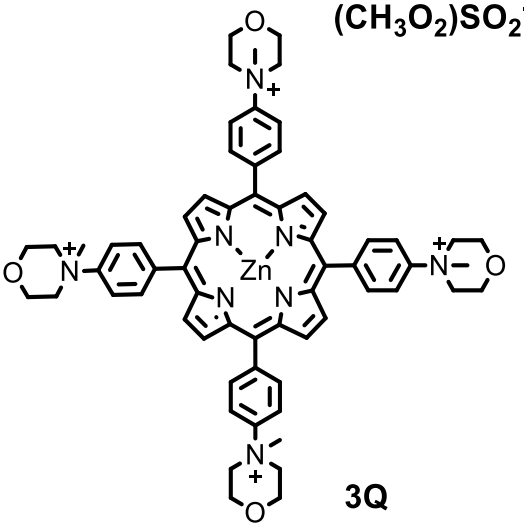 **3Q** **New** Physicochemical and PDT

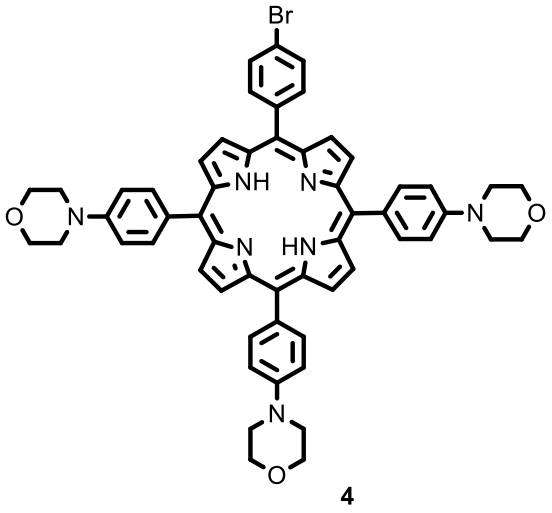

4

New

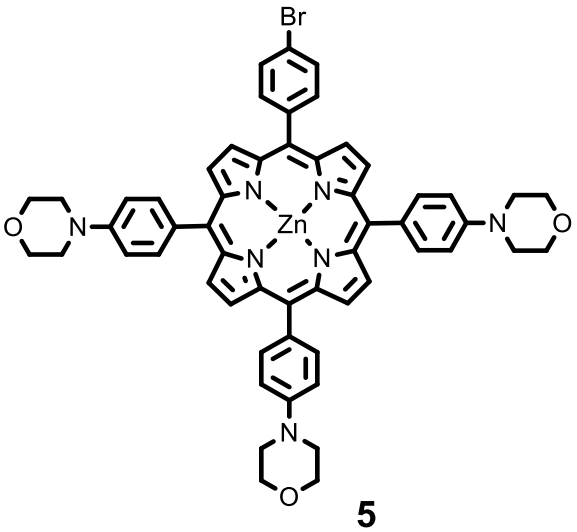

5

New

Physicochemical and PDT

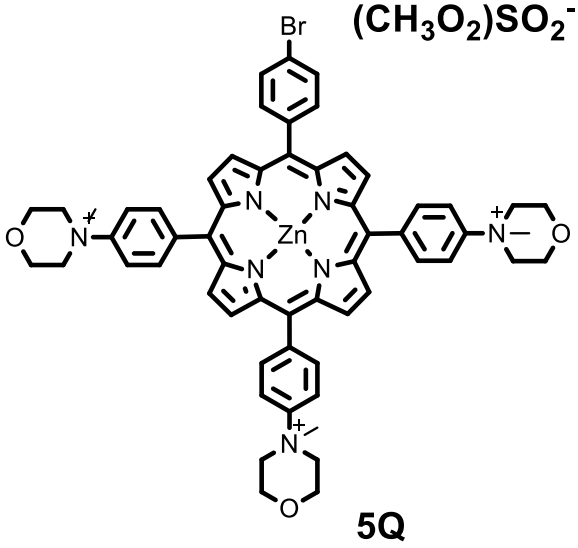

5Q

New

Physicochemical and PDT

1.3 Graphene quantum dots (GQDs)

Graphene quantum dots (GQDs) are carbon-based nanomaterials that are photostable, biocompatible, soluble in aqueous and non-aqueous solvents, minimally toxic, photoluminescent, and are excellent electron donors **[39].** The presence of carboxyl and

hydroxyl groups on GQDs surface, and edges enable covalent attachment, electrostatic interactions and hydrogen bonding with other suitable moieties **[40]**. GQDs have been extensively used for targeting and delivery of therapeutic agents to the tumor sites **[41].** Doping the GQDs with a heteroatom like nitrogen enhances the properties of GQDs. Doping GQDs with nitrogen to form NGQDs not only increases the charge mobility of the graphitic lattice, but also lowers the energy band gap **[42]**, hence in this work the GQDs were doped with nitrogen to form NGQDs.

The general structure of nitrogen doped graphene quantum dots (**Fig 1.4**) consists of different types of nitrogen **[43]**. NGQDs are reported to show high surface area and high number of aromatic rings which enhances their π system **[44]**, and this will permit strong $\pi - \pi$ stacking interaction with the porphyrins leading to enhanced drug delivery in PDT.

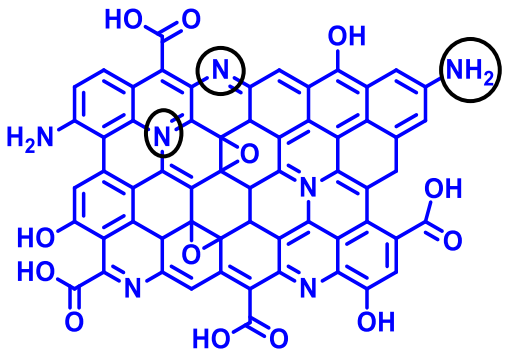

Fig 1.4. Schematic structure of nitrogen doped graphene quantum dots highlighting different positions of nitrogen's on the structure.

1.3.1 Synthesis

GQDs can be synthesized using two different methods, top-down method, and bottom-up method.

Top-down method involves the use of bulk materials such as graphite, graphene oxide etc. that are subjected to harsh treatment to convert them to nanoscale, **Scheme 1.3**. Various approaches may be used to form GQDs in top-down method such as hydrothermal, solvothermal cutting process etc. **[45]**.

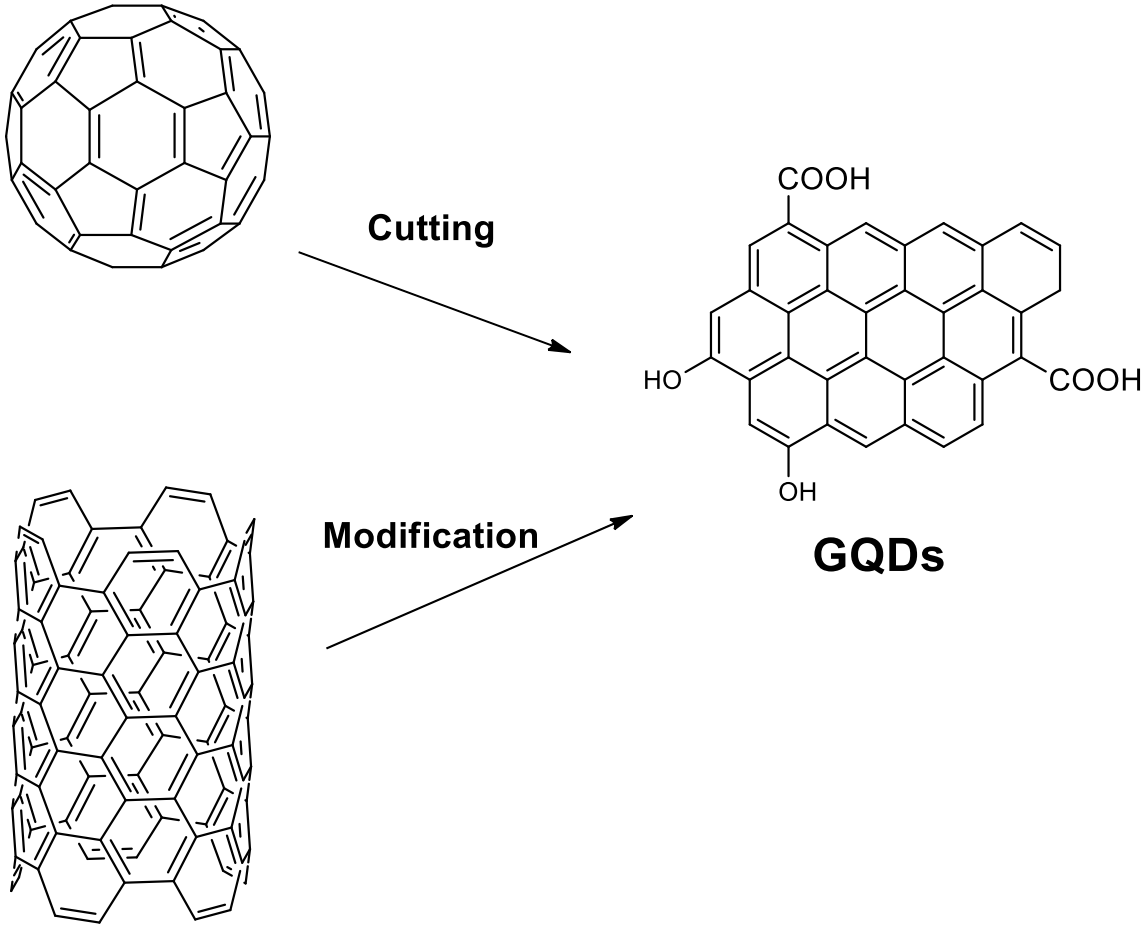

Scheme 1.3. Schematic representation of GQDs synthesized using top-down approach

Bottom-up method involves the use of small molecules as the starting material such as citric acid, fructose and, etc. Various approaches may be used in bottom-up for these small molecules to assemble and form GQDs such as microwave pyrolysis, hydrothermal treatment and, etc (**Scheme 1.4**). The bottom-up method enables better control of size and shape of GQDs **[46]**. In this work bottom-up method was used to synthesize the GQDs using citric acid as starting material, and urea as doping material to form NGQDs **[47]**.

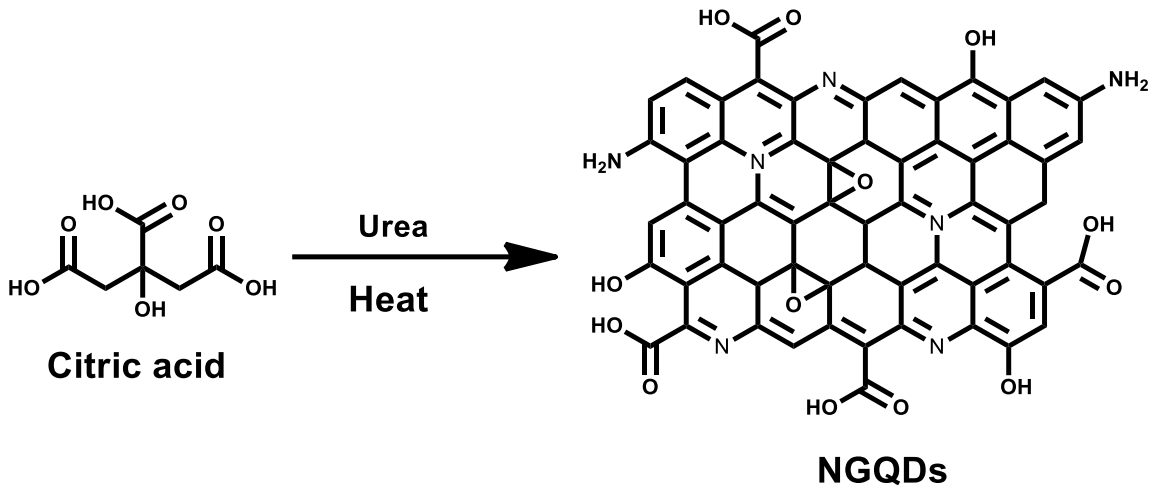

Scheme 1.4. Schematic representation of synthesis of nitrogen doped graphene quantum dots using bottom-up method.

1.3.2. Bio-functionalized NGQDs

To improve the selectivity towards cancerous cells and drug efficacy, NGQDs can be functionalized with biomolecules that have high selectivity. Hence in this work NGQDs were functionalized with biotin and folic acid.

1.3.2.1 Biotin

Biotin is a micronutrient that is responsible for cell growth, but the demand for biotin is higher in cancer cells than in normal cells, because of the abnormal growth and proliferation of cancer cells **[48]**. Therefore, attaching biotin to NGQDs helps the drug to locate the cancer cells. In addition, biotin receptors serve as promising biomarkers for cancer diagnosis and specific therapy **[49]**.

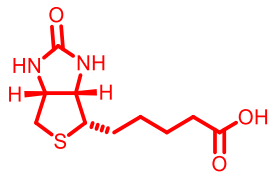

Fig 1.5. Schematic structure of biotin.

1.3.2.2 Folic acid

Folic acid (FA) is a cancer targeting agent, allowing drug endocytosis via folate receptor (FR) **[50]**, therefore decorating the photosensitizer with folic acid will improve selectivity **[51]**. Folic acid receptor is overexpressed in epithelial cancer cells including lung, brain, kidney, breast, and colon cancers. The properties of FR such as high binding affinity and small molecular size enables it to deliver other types of complexes to cancer cells without causing harm to normal tissues **[52]**. Conjugation of folic acid to macromolecules (e.g porphyrin) has been shown to enhance their delivery to folate receptor-expressing cancer cells **[53]**.

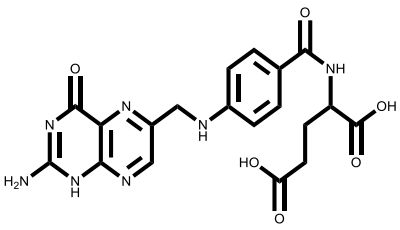

Fig 1.6. Schematic structure of folic acid.

1.3.3 Conjugation of porphyrins to NGQDs/Biotin/Folic acid

The combination of porphyrin and GQDs has been reported to enhance cancer treatment **[54]**. Porphyrins can be conjugated to NGQDs either through the formation of covalent bond or non-covalent attachment. Covalent bond conjugation involves the use of functional groups on the edges of the NGQDs to form a bond with suitable functional groups on the porphyrins. For non-covalent attachment the porphyrins are loaded on the surface of NGQDs through π-π interactions.

Table 1.2 shows porphyrins (asymmetric and symmetric) which have been linked to folic acid, biotin, and graphene quantum dots for PDT studies in literature **[54-60]**. The table shows that mainly metal free porphyrins were employed. In addition, there are no studies on cationic porphyrins that are linked to either of the biomolecules or GQDs. Cationic porphyrins can electrostatically interact with the negative charges present on the tumor cell membranes, facilitating penetration through membranes giving better results in PDT **[61]**. Hence cationic porphyrins are employed in this work. Axially ligated porphyrins are covalently linked to the biomolecules, or NGQDs for the first time in this thesis. The biomolecules employed: folic acid and biotin are selective and specific PDT agents, as stated above.

Table 1.2 List of porphyrins conjugated to biomolecules or graphene quantum dots applied in PDT before.

Porphyrin	Nanoparticle/ Biomolecule	Bond	REF
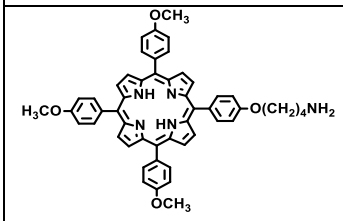	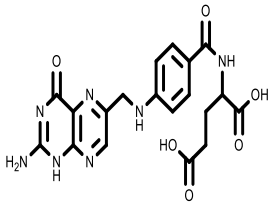 Folic acid	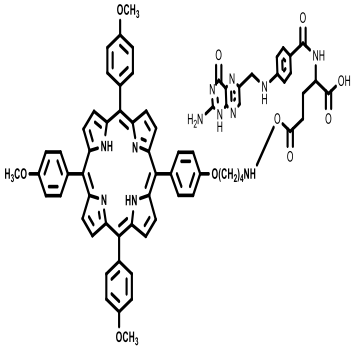 **Covalent**	**[55]**
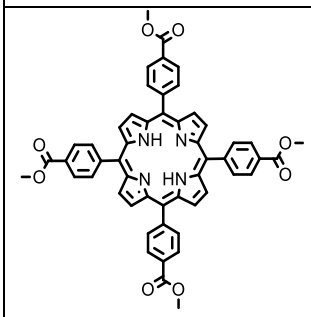	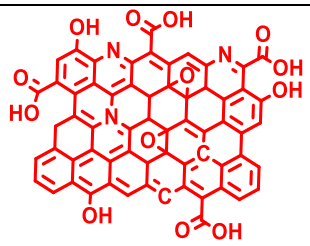 Graphene quantum dots (GQDs)	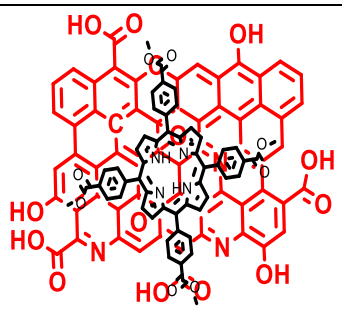 **π π**	**[54]**
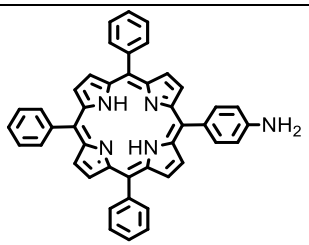	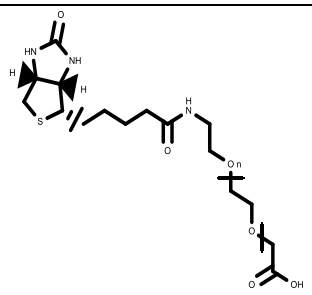 PEG-Biotin	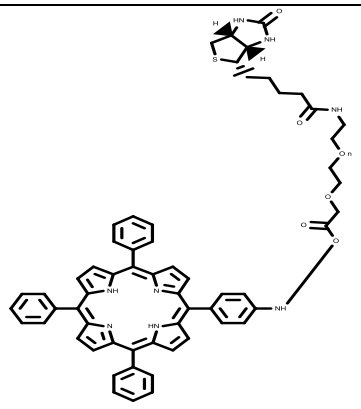 **Covalent**	**[56]**

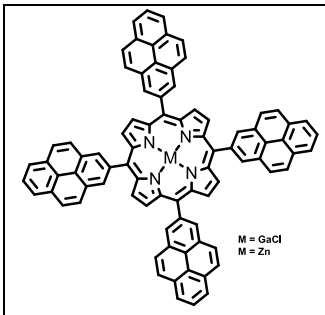	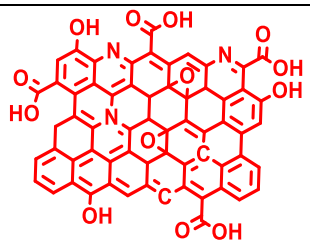 GQDs	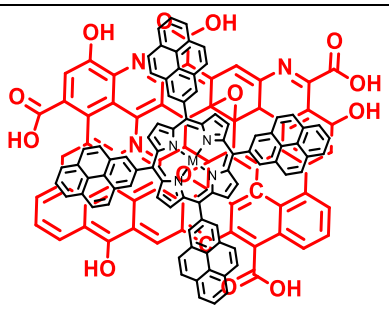 **π π**	**[57]**
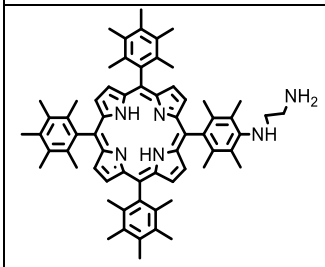	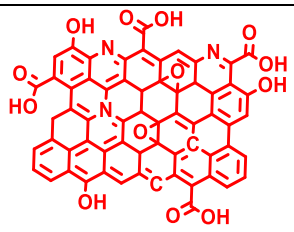 GQDs	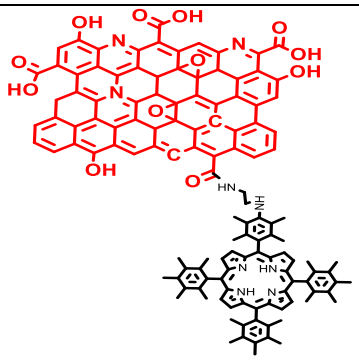 **Covalent (amide bond)**	**[58]**
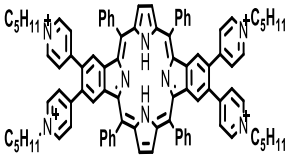	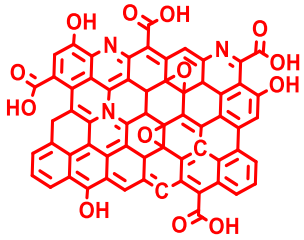 GQDs	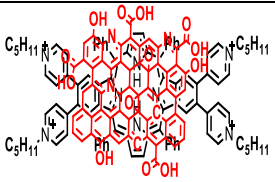 **π π**	**[59]**
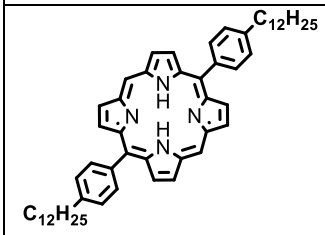	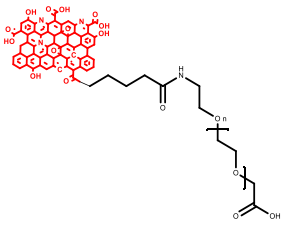 PEG-GQDs	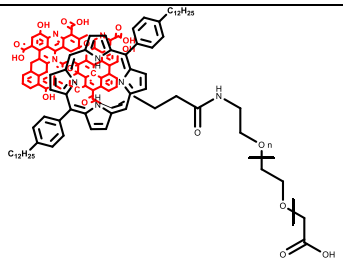	**[60]**

1.3.4 Porphyrins and their corresponding conjugates used in this work

In this work symmetric and asymmetric porphyrins were synthesized and metalated with tin or zinc to enhance their intersystem crossing to the triplet state. Biotin (B) was linked to NGQDs by amide bond to form B-NGQDs, also folic acid (FA) was linked to NGQDs by amide bond to form FA-NGQDs. The synthesized porphyrin complexes were further conjugated to B-NGQDs and/ FA-NGQDs to enhance their target delivery towards cancerous cells. **Tables 1.1**, and **1.3** outline all the porphyrins used in this work and their conjugates, and all the complexes used in this work are new.

Table 1.3 Porphyrins and corresponding conjugates used in this work. All studied for PDT.

Conjugate	Biomolecule/Nanoparticle	Interaction with porphyrin
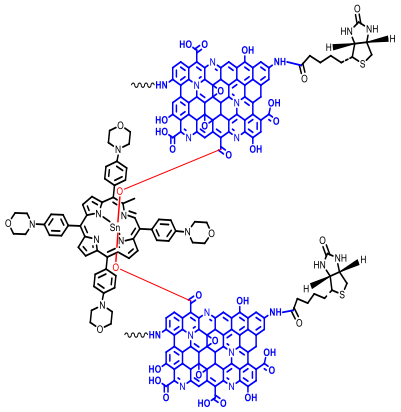 **2**-B-NGQDs **(New)**	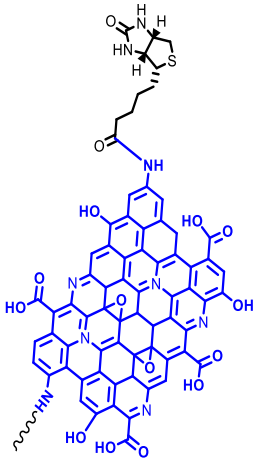 Biotin- Nitrogen doped graphene quantum dots (B-NGQDs) **(New)**	**Covalent (amide) bond**
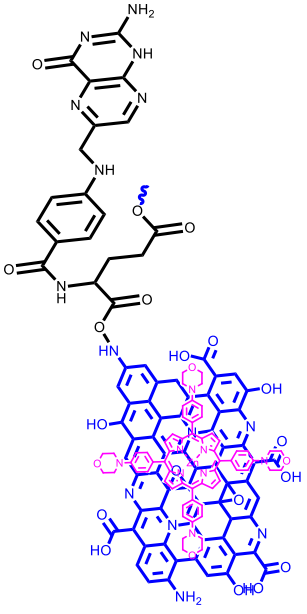 **3**-FA-NGQDs **(New)**	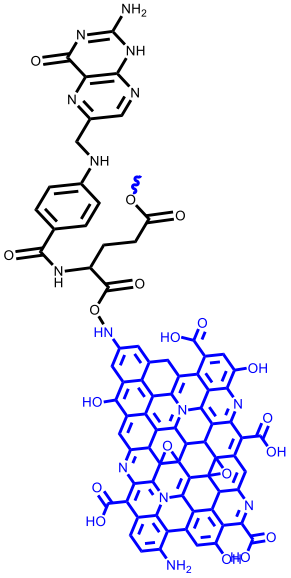 Folic acid-NGQDs (FA-NGQDs) **(New)**	**π π**

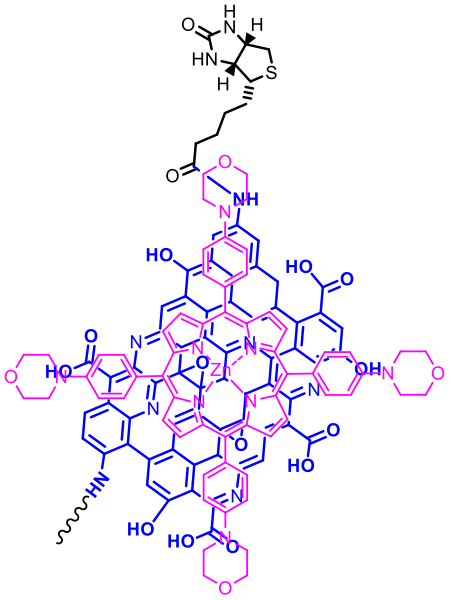 **3**-B-NGQDs **(New)**	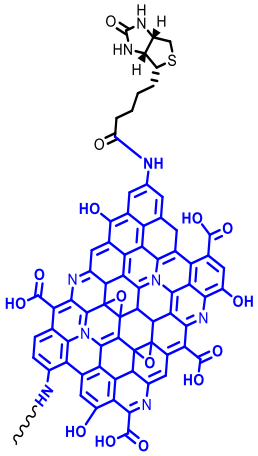 B-NGQDs	
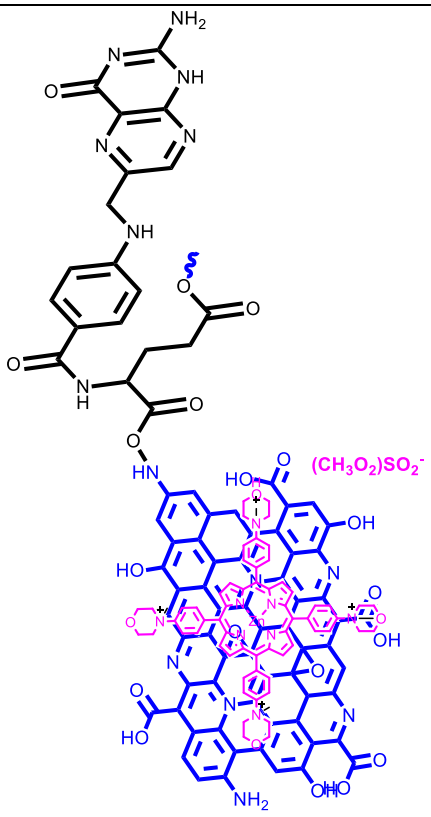 **3Q**-FA-NGQDs **(New)**	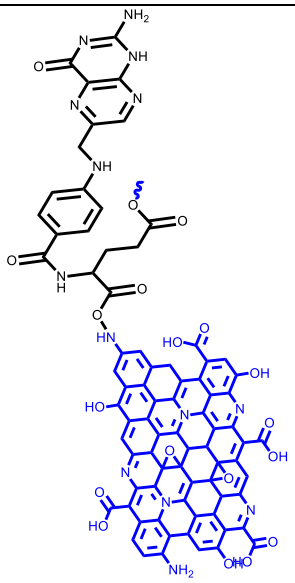 FA-NGQDs	**π π**

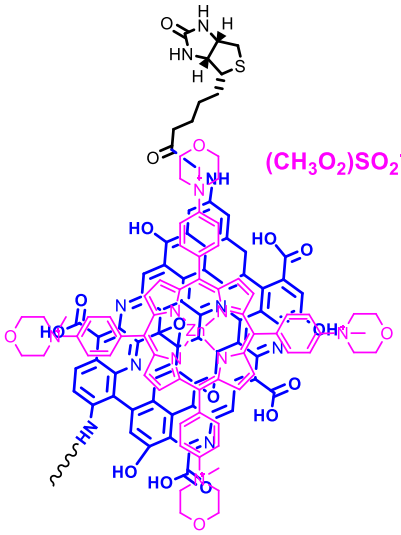 **3Q**-B-NGQDs **(New)**	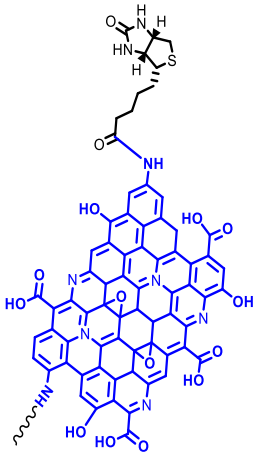 B-NGQDs	**π π**
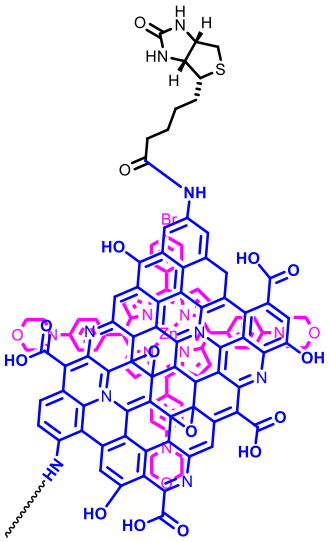 **5**-B-NGQDs **(New)**	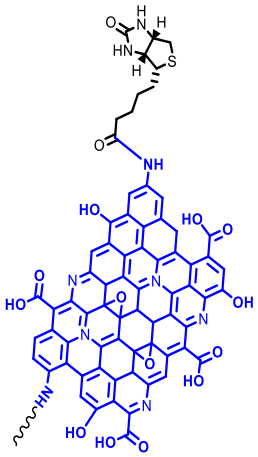 B-NGQDs	**π π**
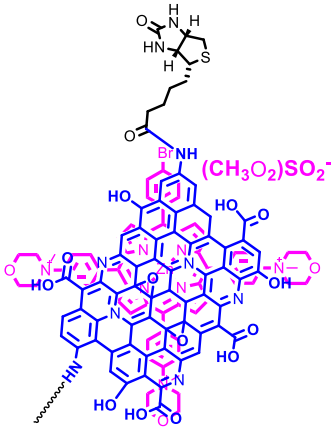 **5Q**-B-NGQDs	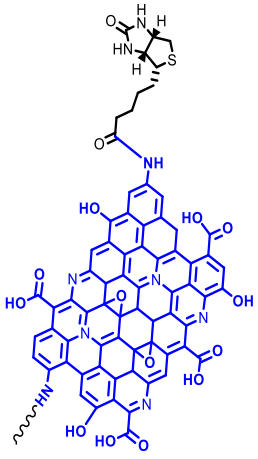	**π π**

(New)	B-NGQDs	

1.4. Rationale

The effect of different factors that influences or enhances the PDT activity and photo-physiochemical properties of the complexes were studied as follows:

- The effect of central metal was determined by comparing complex **2** and **3**.
- The effect of positive charge was determined by comparing **3** with **3Q** and **5** with **5Q.**
- The effect of asymmetry was determined using **3** and **5**.
- The effect of heavy atom of Br substituent was determined using **3** and **5**.
- Biotin was compared with folic acid to determine which has better efficacy of delivery of drugs in cancer cells, by comparing **3Q**-B-NGQDs and **3Q**-FA-NGQDs.
- Complexes **1** and **4** were employed as precursors.

Chapter 2

Experimental

2.1. Materials

2.1.1 General reagents and solvents

N-N dimethyl formamide (DMF), dimethyl sulfoxide (DMSO), methanol (MeOH), ethanol (EtOH), chloroform, and sulphric acid were purchased from Merk. Ultra-pure water obtained from the installed purifying system from ELGA, Veolia water PURELAB, Flex system (Marlow, UK). Chloroform, hydrochloric acid, alpha-cyano-4-hydroxycinnamic acid, and sodium hydrogen pellets were purchased from Sigma-Aldrich.

2.1.2 Reagents for porphyrin synthesis

Propanoic acid, dimethyl sulfide, 4-bromobenzaldehyde, 4-(4-morpholinyl) benzaldehyde, tin (IV) chloride, 4-amino phenol, ammonia, deuterated chloroform ($CDCl_3$), zinc acetate dihydrate, 4-formylbenzoic acid, pyrrole, pyridine, trifluoroacetic acid (TFA), 2,3-Dichloro-5,6-dicyano -1,4- benzoquinone (DDQ), silica gel 60 (0.04-0.063 mm), were purchased from Sigma-Aldrich. The synthesis of NGQDs has been reported **[62].**

2.1.3 Reagents for bio-functionalized nitrogen doped graphene quantum dots

N,N-Dicyclohexylcarbodiimide (DCC), 4-dimethylamino pyridine (DMAP), biotin, urea, citric acid, 1-ethyl-3-(3-dimethylamonopropyl)-carbodiimide (EDC), N-Hydroxysuccinimide (NHS), and folic acid were purchased from Sigma-Aldrich. Phosphate buffer saline (PBS, 10 mM) pH 7.4 was prepared using appropriate amounts of Na_2HPO_4 and NaOH.

2.1.4 Reagents for photo-physiochemical studies

Zn 5,10,15,20-tetraphenyl-21H,23H-porphine (ZnTPP), 9,10 dimethylanthracene (DMA), LUDOX HS-40 colloidal silica, and quinine sulfate were purchased from Sigma-Aldrich.

2.1.5 Reagents for cell studies

Human breast adenocarcinoma MCF-7 were purchased from Cellonex®. The Dulbecco's phosphate-buffer saline (DPBS), Dulbecco's modified eagle's medium (DMEM, containing 4.5 g/ L-glucose with L-glutamine) with and without phenyl-red were purchased from Lonza®. The heat-inactivated fetal bovine serum (FBS, 10 % (v/v)) and the 100 µg/ mL-penicillin:100 unit/

mL-streptomycin-amphotericin-B-mixture (PSA), as well as the neutral red cell proliferation water soluble tetrazolium (WST) reagent were all purchased from Biowest®.

2.2 Instrumentation

1. Ultraviolet-visible spectroscopy was used to record optical absorption spectra at room temperature using a **Shimadzu UV 2550 spectrophotometer**, using wavelength range 300-800 nm in a 1 cm path length cuvette.
2. Fluorescence emissions and excitation spectra were recorded on a **Varian Eclipse spectrofluorometer**.
3. Mass spectra (MS) data were collected on a Bruker AutoFLEX III Smart-beam TOF/TOF mass spectrometer using α-cyano-4-hydrocinnamic acid as the matrix.
4. Elemental compositions of the NPs and the conjugates were qualitatively determined using energy dispersive X-ray spectroscopy (EDS), **INCA PENTA FET** coupled with the **VAGA TESCAM** operated at 20 kV accelerating voltage.
5. The Raman spectra were collected using the Burker Vetex 70-Ram II Raman spectrometer, with a 1064 nm Nd:YAG laser and a germanium laser cooled with liquid nitrogen.
6. Fourier-transform infrared spectroscopy (FT-IR) spectra were obtained using a **Bruker Alpha model** FT-IR spectrometer with a **Platinum-ATR** with a range 500-4000 cm^{-1}.
7. The transmission electron microscope (TEM), ZEISS LIBRA model 120 operated at 90 kV and TEM software was used for TEM micrographs processing.
8. X-ray powder diffraction (XRD) patterns were recorded on a **Bruker D8, discover instrument** equipped with a **Lynx Eye Detector**, using Cu Kα radiation (λ = 1.5405 A, Ni filter).
9. Dynamic light scattering (DLS) was used for hydrodynamic diameter (Dh) and Zeta potential (ζ) of the nanoparticles and nanoconjugates; measurements were done using a **Malvern Zetasizer Nanoseries, Nano-ZS90**, using disposable cuvettes and Zeta cell.
10. Singlet oxygen quantum yields were done using **Ekspla NT 342B-20-AW laser** with an Nd:YAG that pumps a 420-2300 nm optical 30 parametric oscillator (OPO) (355 nm,

2.0 mJ/7 ns, 20Hz) to provide monochromatic light at a crossover wavelength for the standard and sample. A Thermo Scientific Evolution 350 spectrometer was used to record degradation of singlet oxygen quencher (DMA) at a specific time intervals.

11. X-ray photoelectron spectroscopy (XPS) analysis was measured using an **AXIS UltraDLD (supplied by Kratos Analytical)** with an Al (monochromatic) anode equipped with a charge neutralizer.
12. Merck Eppendorf centrifuge 5810 was used for precipitates extraction.
13. The triplet state lifetimes spectra were recorded in DMSO at 470 nm using an Edinburgh Instruments LP980 spectrometer and an Ekspla NT-342B laser equipped with an OPO to provide an excitation wavelength (2.0 mJ excitation energy, 7 ns pulse duration and a 20 Hz repetition rate). The solutions were degassed with nitrogen for 20 min prior to measurement, and the absorbances were maintained at ca. 1.5 for the Soret band. Exponential curve fitting of the decay curve using OriginPro 8 software provided the triplet lifetimes.
14. Bruker AMX 400 MHz and 80 MHz benchtop NMR spectrometers were used to obtain ^{1}H-NMR data. The spectra were obtained at ambient temperature using deuterated solvents ($CDCl_3$ and DMSO-d_6).
15. Synergy 2 multi-mode microplate reader (BioTek®) was used to measure cell viability for PDT.
16. Thorlabs M625L3 LED (625 nm) was used for PDT studies.
17. SpectraMax M3, Molecular Devices multi-well-plate reader from Separations using the SoftMax Pro6.4 programme was used to read absorbance intensity for cellular uptake studies.

2.3 Synthesis

2.3.1 Synthesis of 5,10,15,20 -tetra (4-Morpholinyl) porphyrin (1), Scheme 4.1

Propanoic acid (150 mL) was refluxed in the presence of 4-(-4 morpholinyl) benzaldehyde (2 g, 0.01 mol) at 120 ℃ for 5h. This was followed by the addition of pyrrole (1mL) and the mixture was allowed to reflux for 3h, then cooled to room temperature to precipitate the porphyrin. The product was then flittered and washed with methanol and air dried to give complex **1** ($C_{60}H_{58}N_8O_4$) as purple solid. Yield = 78%. FTIR (cm^{-1}): 2995 (Ar, C-H), 2800(-C-H), 1600 (Ar, C=N), 1200 (C-O-C). ^{1}H NMR ($CDCl_3$): δ ppm 8.43 (d, 4H, Ar, pyrrole), 8.31 (s, 4H, Ar, pyrrole), 7.44(d, 8H, Ar, phenyl) 7.34 (d, 8H, Ar, phenyl), 3.45 (m, 16H, CH_2), 1.20 (m, 16H, CH2). UV/Vis (DMSO), λ_{max} nm (log ε): 428 (5.65), 522 (5.22), 562 (5.09), 598 (4.98), 652 (4.87). MALDI-TOF MS, calc 954.46, found 956.46 $[M+2H]^+$.

2.3.2 Synthesis of Sn (IV) 5,10,15,20- tetra (4-Morpholinyl) porphyrin (2), Scheme 4.2

The 5,10,15,20 tetra-4-morpholinyl porphyrin (**1**) (0.1 g, 0.0001 mol) and tin(IV) chloride (0.2 g, 0.001 mol) were added to pyridine (20 mL) and allowed to reflux for 3 h. The mixture was cooled down to room temperature, and ammonia (50 mL) was added to the reaction followed by stirring for 1 h at room temperature. The mixture was then flittered and washed with water and air dried to give $Sn(OH)_2$tetra-4-morpholinyl porphyrin (complex **2**) as a green solid**,** alumina neutral column with MeOH/$CHCl_3$ (1:9) as eluent was used to obtain a pure complex **2** ($C_{60}H_{58}N_8O_6Sn$). Yield = 62%, FTIR (cm^{-1}) 2900 (Ar, C-H), 2800 (C-H), 1661 (Ar, C=N), 1221 (C-N), 1150 (C-O-C). ^{1}H NMR ($CDCl_3$): δ ppm 9.20 (s, Ar,4H, pyrrole), 9.14 (s, Ar, 4H, pyrrole), 8.25 (s, 8H, Ar, phenyl), 7.35 (d, 8H, Ar, phenyl), 4.0 (m, 16H, CH_2), 1.8 (m,16H, CH_2). UV/Vis (DMSO), λ_{max} nm (log ε):445 (5.79), 568 (5.23), 625 (4.95). MALDI-TOF MS, calc 1106.35, found 1105.35 $[M+H]^+$.

2.3.3 Synthesis of Zn 5,10,15,20- tetra (4-Morpholinyl) porphyrin (3), Scheme 4.3

In a 100 mL round bottom flask containing chloroform (10 mL), complex **1** (0.8 g, 0.00083 mol) was added followed by excess amount of zinc acetate dihydrate (2.4 g, 0.010 mol) in MeOH (8 mL). The mixture was allowed to reflux for 2h, the metalated crude was poured into water (100 mL) and the organic layer was collected and dried followed by the purification with aluminium oxide neutral column chromatography with chloroform as eluent to obtain pure complex **3.** Yield = 70 %. FTIR (cm^{-1}) 3076 (Ar,C-H), 1546 (Ar,C=N), 1413 (C-N), 1147 (C-O-C).

^{1}H NMR ($CDCl_3$): δ ppm 7.47 (s, 4H, Ar, pyrrole), 7.29 (d, 4H, *J*= 2.0 Hz, Ar, pyrrole), 7.09 (d, 8H, *J*= 3.4 Hz Ar, phenyl), 7.05 (d, 8H, *J*=2.5 Hz, Ar, phenyl), 2.65 (m, *J*= 3.4 Hz, 16H, CH_2), 1.20 (m, *J*= 3.4 Hz ,16H, CH_2). UV/Vis (DMSO) λ_{max} nm (log ε): 432 (4.14), 563 (3.42), 610 (3.32). MALDI-TOF MS. Calc 1016.37, found 1017.92 $[M+H]^+$.

2.3.4 Quaternization of Zn 5,10,15,20- tetra (4-morpholinyl) porphyrin 3Q, Scheme 4.5

Complex **3** (0.3 g, 0.00023 mol) was dissolved in 5 mL of DMF, followed by the addition of dimethyl sulfate (3 mL). The reaction was allowed to reflux for 30 min, the compound was centrifuged and washed with EtOH to remove excess DMF and the unquaternized species, complex **3Q**, was then obtained. Yield = 62%. FTIR (cm^1) 3419 (Ar,-CH_3), 3054 (Ar, C-H), 1657 (Ar, C=N), 1446 (C-N). ^{1}H NMR (DMF): δ ppm 8.30 (s,4H, Ar, pyrrole), 8.05 (s, 4H, Ar, pyrrole) 7.80 (d, 8H, *J*= 1.7 Hz, Ar, phenyl) 7.70 (d, 8H, *J*=5.1 Hz, Ar, phenyl), 4.01 (s, 3H, CH_3O), 3.25 (m, 16H, *J*=10.1 Hz, CH_2), 2.85 (s, 12H, quaternized methyl-H), 2.40 (m, 16H, *J*=10.2 Hz, CH_2). UV/Vis (DMSO) λ_{max} nm (log ε): 436 (4.36), 568 (3.72), 612(3.51). MALDI-TOF MS. Cal 269, found 266 $[M+3H^+]$.

2.3.5 Synthesis of 5-(4-bromo) 10,15,20-tris (4-morphlinyl) porphyrin (4), Scheme 4.4

4-4 (Morpholinyl)benzaldehyde (0.5g,0.002 mol) was dissolved in 200 mL of DMF stirring at temperature under inert atmosphere, and this was followed by the dropwise addition of pyrrole (0.23 mL) and the reaction was allowed to stir for 4h. To this mixture, 4-bromobenzaldehyde (0.16g, 0.0008 mol) and TFA (1.19 mL) were added and, the mixture was stirred for overnight. Then DDQ (2.36g) was added and the mixture was allowed to stir again for 24h to convert the porphyrinogen intermediate formed to a stable aromatic porphyrin. Silica chromatography was used to purify the compound using chloroform/petroleum ether (1:9) as eluent to give a purple solid, and the resulting compound (complex **4**) was air dried in fumehood. Yield = 72%. FTIR (cm^{-1}) 2977 (Ar, CH), 1500 (N-H), 1417 (C-N).^{1}H NMR ($CHCl_3$): δ ppm 8.89 (d, 2H, Ar), 8.56 (s, 6H, Ar), 8.03 (d, 2H, Ar), 6.42 (s, 4H, Ar-pyrrole), 5.95 (s, 6H, Ar),5.16 (s, 4H, Ar-pyrrole), 3.66 (m, 12H,CH_2), 1.23 (m, 12H, CH_2). MALDI-TOF MS (m/z). Cal 947.32 found 946.04 $[M+H^+]$. UV/Vis (DMSO) λ_{max} nm (log ε): 432 (4.10), 522 (2.92), 563 (2.88), 602 (2.77), 650 (2.53). MALDI-TOF MS. Cal 947.32, found 946.04 $[M+H^+]$.

2.3.6 Synthesis of Zn 5-(4-bromo) 10,15,20-tris (4-morphlinyl) porphyrin (5), Scheme 4.3

In a 100 mL round bottom flask containing chloroform (10 mL), complex **4** (0.8 g, 0.00083 mol) was added followed by excess amount of zinc acetate dihydrate (2.4 g, 0.010 mol) in MeOH (8 mL). The mixture was allowed to reflux for 2h, the metalated crude was poured into water (100 mL) and the organic layer was collected and dried followed by the purification with aluminium oxide neutral column chromatography with chloroform as eluent to obtain pure complex **5**. Yield = 68 %. FTIR (cm^{-1}) 2977 (Ar, CH), 1673 (Ar, NH), 1417 (C-N). ^{1}H NMR ($CHCl_3$): δ ppm 11.01 (s, 2H, Ar-Br), 10.56 (s, 2H, Ar-Br), 10.17 (s, 4H, Ar-CH), 9.81 (s, 4H, Ar-CH_2), 8.92 (s, 2H, Ar-CH_2), 8.60 (s, 2H, Ar-CH_2), 5.62 (s, 1H, Ar-pyrrole), 5.46 (s, 1H, Ar-pyrrole), 5.37 (s, 1H, Ar-pyrrole), 5.30(s, 1H, Ar-pyrrole), 4.76 (s, 4H, Ar-pyrrole), 4.50 (m, 12H, -CH_2), 3.75 (m, 12H, -CH_2). UV/Vis (DMSO) λ_{max} nm (log ε): 427 (3.89), 560 (3.03), 605 (2.85). MALDI-TOF MS. Cal 1011.23, found 1011.68.

2.3.7 Quaternization of Zn 5-(4-bromo) 10,15,20-tris (4-morphlinyl) porphyrin (5Q), Scheme 4.5

Complex **5** (0.3 g, 0.00023 mol) was dissolved in 5 mL of DMF, followed by the addition of dimethyl sulfate (3 mL). The reaction was allowed to reflux for 30 min, the compound was centrifuged and washed with EtOH to remove excess DMF and the unquaternized species,and complex **5Q** was obtained. Yield = 58%. FTIR (cm^{-1}) 3489 (Ar, -CH_3), 2931 (Ar, CH), 1673 (NH), 1429 (C-N). ^{1}H NMR (DMSO): δ ppm 9.17 (s, 4H, Ar-CH_2), 9.08 (s, 2H, Ar-Br), 8.87 (s, 4H, Ar-CH_2), 6.22 (s, 2H, Ar-Br), 5.5-5.29 (d, 1H, Ar-pyrrole), 4.94 (s, 1H, Ar-pyrrole), 4.79-4.75 (d, 1H, Ar-pyrrole), 4.71-4.67 (d, 1H, Ar-pyrrole), 4.54 (s, 2H, Ar-CH_2), 4.50 (s, 2H, Ar-CH_2), 4.36 (s, 2H, Ar-pyrrole), 4.05 (s, 2H, Ar-pyrrole), 3.74 (m, 12H, Ar-CH_2), 2.64 (m, 12H, Ar-CH_2), 2.01 (m, 12H, quaternized methyl-H). UV/Vis (DMSO) λ_{max} nm (log ε) 429 (3.79), 557 (3.17), 598 (3.06). MALDI-TOF MS (m/z). Cal 451.23 found 567.48 $[M+(DMSO.2H_2O)]^+$.

2.3.8. Preparation of Biotin-NGQDs, Scheme 4.6 (A)

Biotin (40 mg, 0.16 mmol) was dissolved in DMF (5mL) and to this solution DCC (23 mg, 0.18 mmol) and DMAP (20 mg, 0.16 mmol) were added and the mixture was stirred at room

temperature for 24h. NGQDs (0.2g) were added to water (2mL) followed by sonication for 30 min. The biotin solution (0.012 mol/mL) was then added to the NGQDs solution. The mixture was stirred for 24h at room temperature, the biotin-NGQDs (**B-NGQDs**) mixture was suspended in ethanol and then collected by centrifugation to remove the non-conjugated biotin, NGQDs, DCC and DMAP **[63]**.

2.3.9. Preparation of folic acid-NGQDs, Scheme 4.6 (B)

Folic acid (40 mg) and PBS (30 mL) were added to the beaker, and the mixture was stirred for 2 h at room temperature to allow folic acid to dissolve. Then, EDC (0.14 g, 0.0009 mol) and NHS (0.10g, 0.0009 mol) were added under magnetic stirring in the dark for 24 h. The NGQDs were added to the solution followed by further stirring for 24 h. Finally, dialysis was carried out for one day using a dialysis membrane and freeze drying was carried out to obtain folic acid-conjugated nitrogen-doped graphene quantum dots (**FA-NGQDs**) **[64]**.

2.3.10 Formation of conjugates

2.3.10.1 Covalent conjugation (ester bond) complex 2 to B-NGQDs, Scheme 4.7

Complex **2** (40 mg, 0.03 mmol) and B-NGQDs (20 mg) were dissolved in dry DMF and sonicated for 4h. The mixture was then refluxed with continuous stirring in the dark for 72h. The conjugate was precipitated using ethanol and collected by centrifugation and thereafter dried in vacuum **[65]**. **2**-B-NGQDs was then formed through an ester bond.

2.3.10.2 π-π stack conjugation to FA-NGQDs, Scheme 4.8

Complex **3 (**0.1 g, 0.00009 mol) and **3Q** (0.1 g 0.00092 mol) were dissolved separately in 10 mL of DMF, then FA-NGQDs (0.8g) were added to the mixtures followed by stirring in the dark at room temperature for 48 h. The product obtained (**3**-FA-NGQDs and **3Q**-FA-NGQDs) was centrifuged and washed with EtOH to remove unreacted species.

2.3.10.3 π-π stack conjugation to B-NGQDs, Scheme 4.8

Complexes **3** (0.1 g, 0.00092 mol), **3Q** (0.1g, 0.000085 mol), **5** (0.1 g, 0.00009 mol), and **5Q** (0.1g, 0.000086 mol) were dissolved separately in 10 mL of DMF. B-NGQDs (20 mg) was added

to the mixtures followed by stirring in the dark in room temperature for 48 h. The conjugates obtained were centrifuged and washed with EtOH to remove the unreacted species.

2.4 Cell studies

2.4.1 Tissue culture studies

For cell studies, the human breast cancer MCF7-cells were cultured in 75 cm^2 vented flasks (or 96-well plates, for cytotoxicity studies) in a 37 °C incubator from HealForce® with a ~5% CO_2 humidified atmosphere in culture media (DMEM containing 4.5 g/ L-glucose with L-glutamine and phenol red, supplemented with 10% FBS and 5% PSA), and were grown to 100% confluency. All the cell studies were performed in triplicate.

2.4.2 Dark and PDT studies

The complexes and their conjugates were inoculated into 96 well plates at different concentrations: 2.5, 5, 10, 20, and 40 µg/mL in culture media with 1% DMSO solution. The cells were incubated in dark for 24h, and thereafter they were washed with DPBS. Then the DMEM without phenyl red was added to the wells.

For PDT studies the cells were irradiated with Thorlabs M625L3 LED (625 nm) for 30 min. The DMEM without phenyl red was thereafter decanted, and the cultured media was added. The cells were re-incubated in growth conditions. For dark toxicity studies, cell samples similar to those prepared for PDT studies were prepared. The cells were however kept in the dark for 24 h. The cell viability assay using WST was performed to quantify viable cells.

The dark and PDT cell viability was measured after 24h using WST assay on a synergy™ 2 multi-mode microplate reader BioTek at 450nm. Equation **2.1**

$$\textbf{Cell viability} = \frac{\textbf{Absorbance of sample}}{\textbf{Absorbance of control}} \times 100\% \qquad \textbf{Equation 2.1}$$

2.4.3 Cellular uptake

To determine drug content in cell samples in 24h, the cells were grown in 96 well plates and inoculated with the NGQDs, B-NGQDQs and FA-NGQDs, porphyrin complexes and their conjugates at the similar concentrations to that of PDT. The plates were incubated at 37 °C

under ~5% CO_2 humidified atmosphere for 24 h. The media was then decanted, and the cells were washed with DPBS to remove complexes/conjugates that have not been absorbed into the cells. The DMEM with no phenyl-red was added and absorbances of the samples were obtained at the λ_{max} of the porphyrin for the porphyrin complexes and their conjugates, and λ_{max} of the NGQDs for NGQDs and B-NGQDs, and FA-NGQDs. To correct the absorbance of the samples, the average absorbance of the control sample (MCF-7 cells with no compounds) was subtracted from the average absorbance of the test samples. The graph of corrected absorbance against the corresponding concentration for each test compound was plotted. The absorbance were obtained using the SpectraMax M3, Molecular Devices multi-well-plate reader from Separations using the SoftMax Pro6.4 programme.

Chapter 3

Failed attempted synthesis

3.1 Conjugation of complex 2 to NGQDs through an amide bond using modified axial ligand, Scheme 3.1

Complex **2** was heated at reflux in $CHCl_3$ for 4h with two equivalent of 4-amino phenol to yield axially ligated complex **6**. Complex **6** was then purified by neutral alumina column chromatography with $CHCl_3$: MeOH (9:1) as eluent. The carboxy moiety of NGQDs was activated by EDC and DMAP for 24h in DMF, then Complex **6** was added to activated NGQDs with an aim to conjugate NGQDs and Complex **6** through an amide bond, but the axial ligand was not stable.

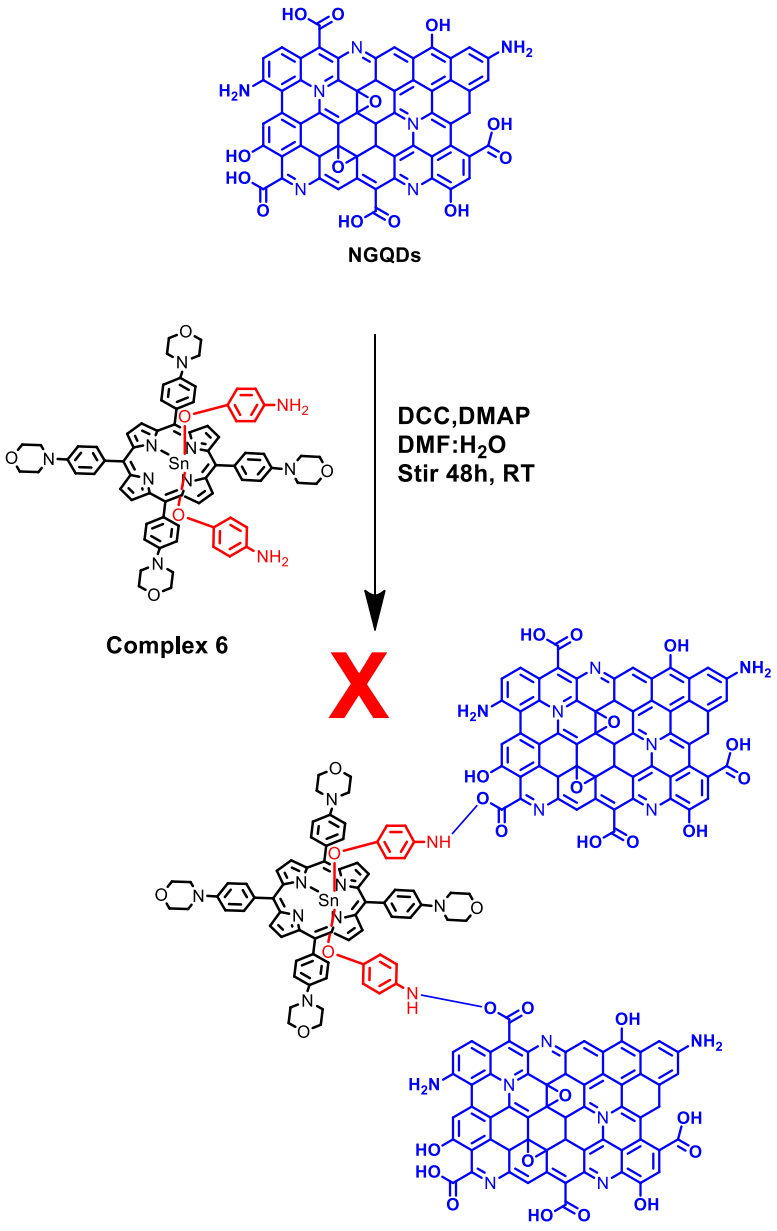

Scheme 3.1. Schematic representation of failed conjugation for complex **6** to NGQDs.

3.2 Synthesis of Complex 7, Scheme 3.2

An attempt to synthesize ABAB porphyrin complex **7** was carried out following the synthetic route reported **[65]** with few modifications. In a 250 mL round bottom flask 4-(-4 morpholinyl) benzaldehyde (0.5g, 0.002 mol) was added to distilled pyrrole (1mL) under an inert atmosphere. Trifluoroacetic acid (TFA) (1.5mL) was added to this mixture which was allowed to stir at room temperature for 30 min. The mixture was poured in water (5 mL) and extracted with dichloromethane (DCM) (3 x 5mL). The organic layer was washed with saturated sodium bicarbonate (3 x 5 mL), followed by water (3 x 5 mL). The organic layers were dried over sodium sulfate and air dried to give 5-(4-morpholinyl) -2-dipyrromethane (DP-morpholinyl). The obtained (DP-morpholinyl) was added to 4-bromobenzaldhyde (0.37g, 0.002 mol) in DCM, to this mixture boron trifluoride etherate ($BF3.OEt_2$) was added and the mixture was allowed to stir for 4h at room temperature under an inert atmosphere. DDQ (2.36g) was further added followed by stirring for 30 min to convert the porphyrinogen intermediate formed to a stable aromatic porphyrin. However, the porphyrinogen intermediate formed converted into a corrole and not a porphyrin.

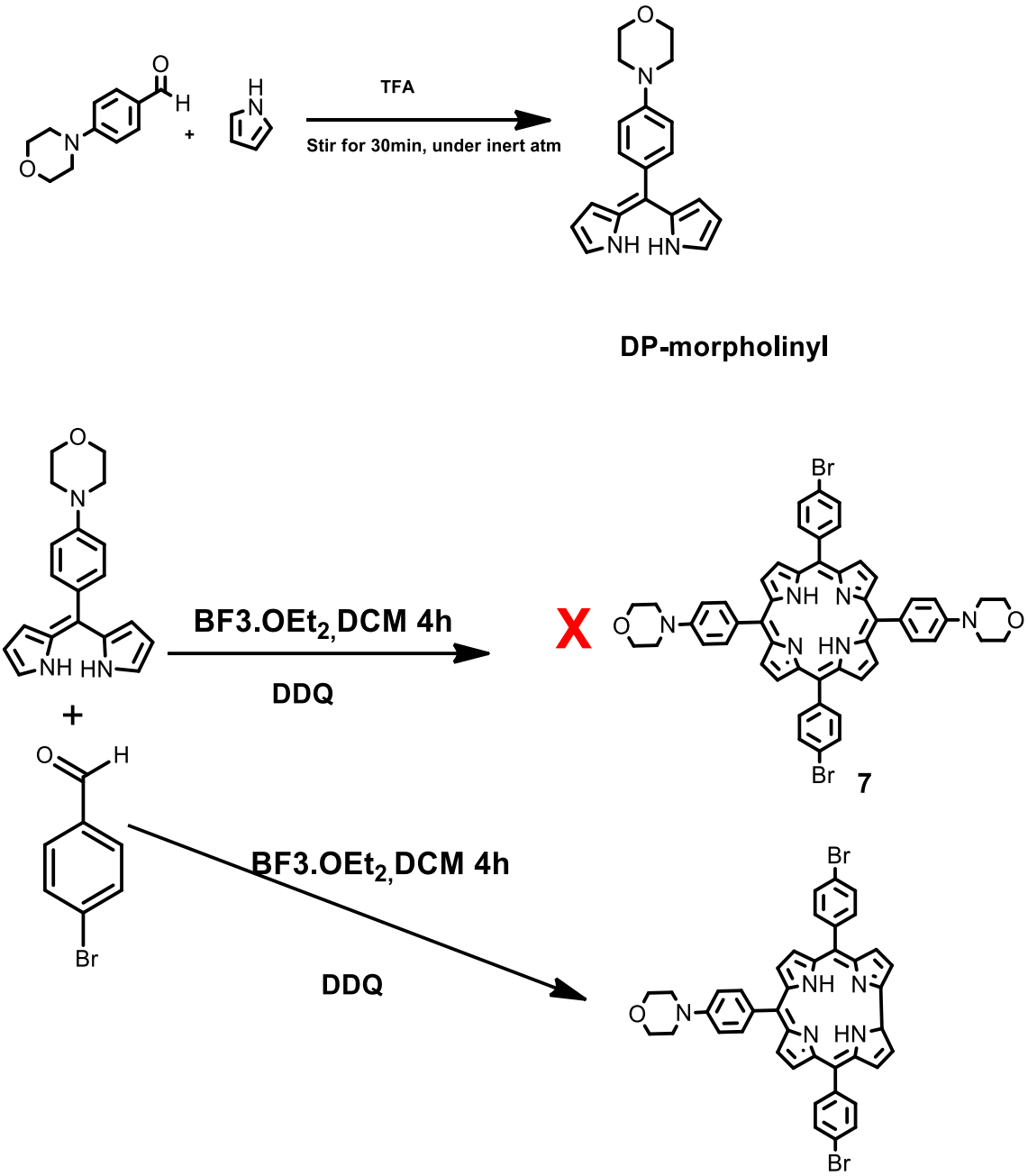

Scheme 3.2. Schematic representation of failed synthesis of ABAB porphyrin.

3.3 Rationale behind the synthesis

The rationale behind the conjugation of complex **6** to NGQDs through functionalized axial ligand was to enhance its photophysiochemical properties and PDT. The rationale for complex **7** was to study the effect of symmetry between tetra (complex **3**), mono (complex **5**) and di (complex **6**) porphyrin and its activity on PDT.

Results and Discussion

PUBLICATIONS

The results discussed in this thesis (chapter 4 and 5) have been published in the following peer reviewed journals.

N. Bridged Magaela, Refilwe Mashitse, Balaji Babu, Muthumuni Managa, Earl Prinsloo, Tebello Nyokong. Sn (IV) porphyrin-biotin decorated nitrogen doped graphene quantum dots nanohybrids for photodynamic therapy. Polyhedron, 213 (2022) 115624.

N. Bridged Magaela, Refilwe Mashite, Tebello Nyokong. The effect of charge on Zn tetra morpholine porphyrin conjugated to folic acid nitrogen doped graphene quantum dots for photodynamic therapy studies. Photodiagnosis and photodynamic therapy, 39(2022) 102898.

N. Bridged Magaela, Refilwe Mashite, Muthumuni Managa, Tebello Nyokong. The effect of asymmetry and conjugation of biotin decorated nitrogen doped graphene quantum dots on morpholine porphyrin for photodynamic therapy. Journal of Coordination Chemistry. IN PRESS.

Side publications

N. Bridged Magaela, C. Lekgowa Makola, Muthumuni Managa, Tebello Nyokong. Photodynamic activity of novel cationic porphyrins conjugated to graphene quantum dots against staphylococcus aureus. Journal of Porphyrins and Phthalocynanines. 26 (2022) 392-402.

Mahlatse Mokgaetjie Ledwaba, **N. Bridged Magaela**, Knowledge Siyabonga Ndlovu, John Mack, Tebello Nyokong, Muthumuni Managa. Photophysical and in vitro photoinactivation of Escherichia coli using cationic 5,10,15,20-tetra(pyridin-3-yl) porphyrin and Zn(II) derivative conjugated to graphene quantum dots. Photodiagnosis and photodynamic therapy 40 (2022) 103127.

N. Bridged Magaela, Knowledge S. Ndlovu, Charmaine S. Tshangana, Adolph A. Muleja, Bhekie B. Mamba, Tebello Nyokong, Muthumuni Managa. Photodegradation of ibuprofen using 5-10-15-20-tetrakis(4-bromophenyl) porphyrin conjugated to graphene quantum dots. Optical Materials. Part A. 134 (2022)113147.

Chapter 4

4.1 Synthesis and characterization of porphyrin complexes

Free base porphyrin complex **1** was synthesized following Alder and Longo method (Scheme **4.1**). The metalation of complex **1** was done with two different metals tin (IV) chloride to give complex **2** (Scheme **4.2**) and zinc acetate dihydrate to give complex **3** (Scheme **4.3**).

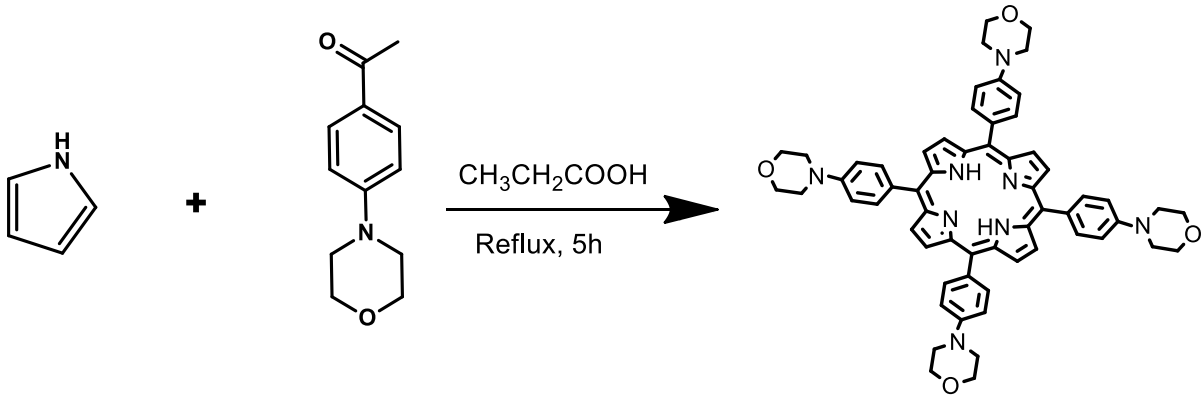

Complex **1**

Scheme **4.1.** Synthetic route of complex **1**

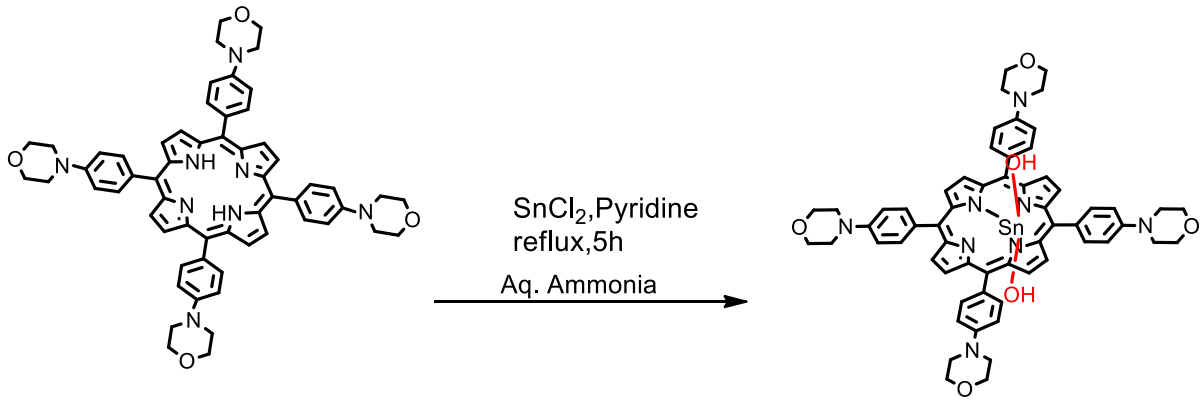

Complex **1**

Complex **2**

Scheme **4.2.** Metalation route for complex **2** using tin (IV) chloride as metal salt

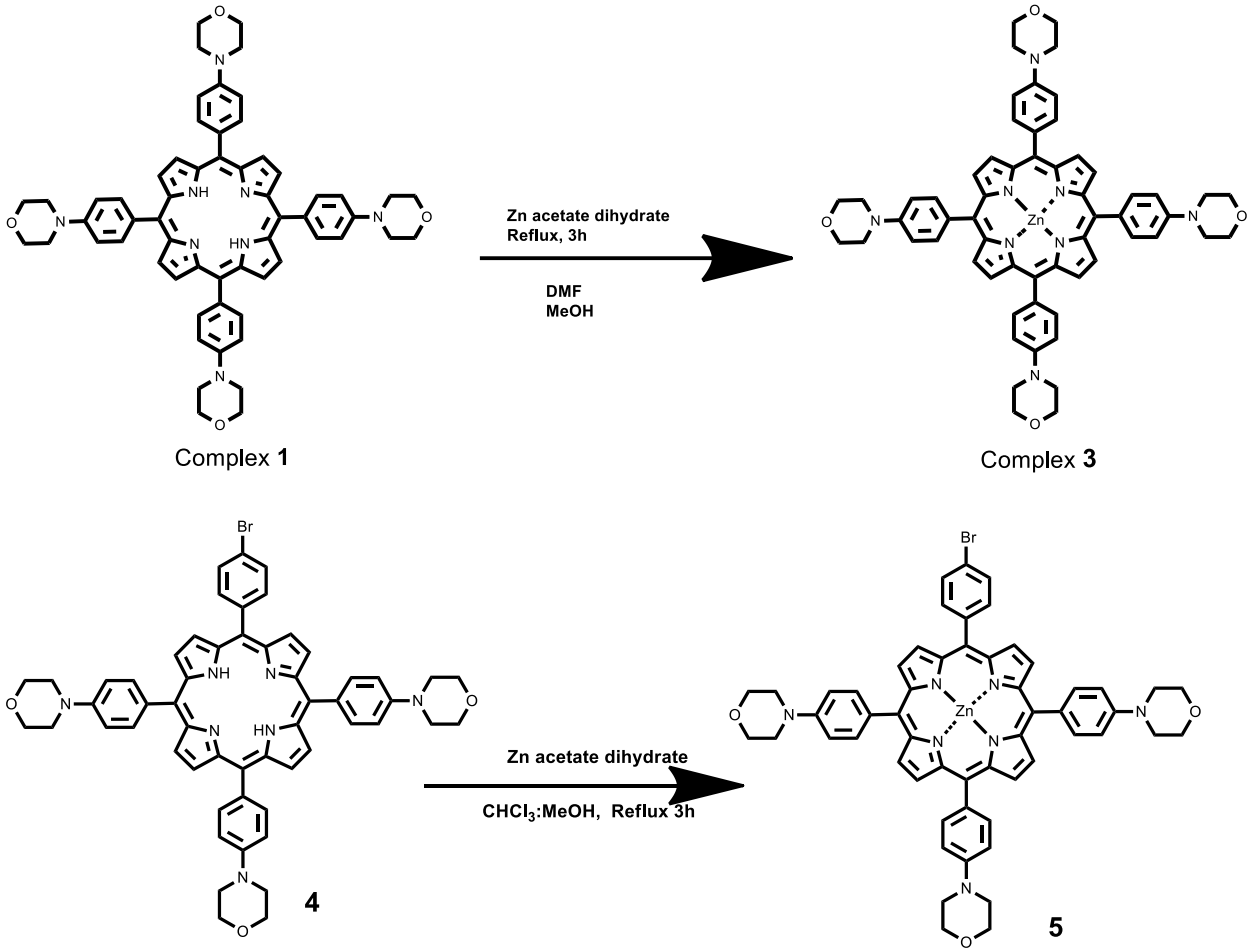

Scheme **4.3.** Metalation route for complex **3** using, zinc acetate dihydrate as a metal salt.

The asymmetric freebase porphyrin complex **4** (Scheme **4.4**) synthesized in this thesis followed the Lindsey method. The metalation of complex **4** to form complex **5** followed the synthetic route in Scheme **4.3** as it was also metalated with zinc acetate dihydrate**.**

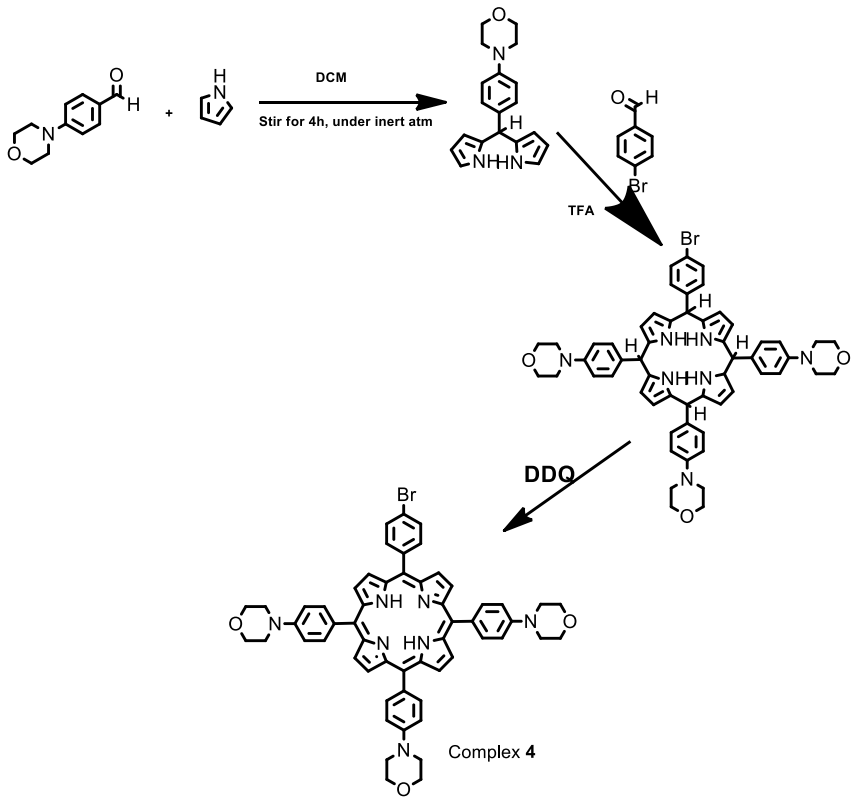

Scheme **4.4.** Synthetic route of complex **4**

All the cationic porphyrins (**3Q** and **5Q**) were synthesized from their respective metalloporphyrins (**3** and **5**) following the reported synthetic procedure **[34]** with slight modification. Dimethyl sulfate was used as a quaternizing agent for the quaternization of both **3Q** and **5Q** as shown in Scheme **4.5**.

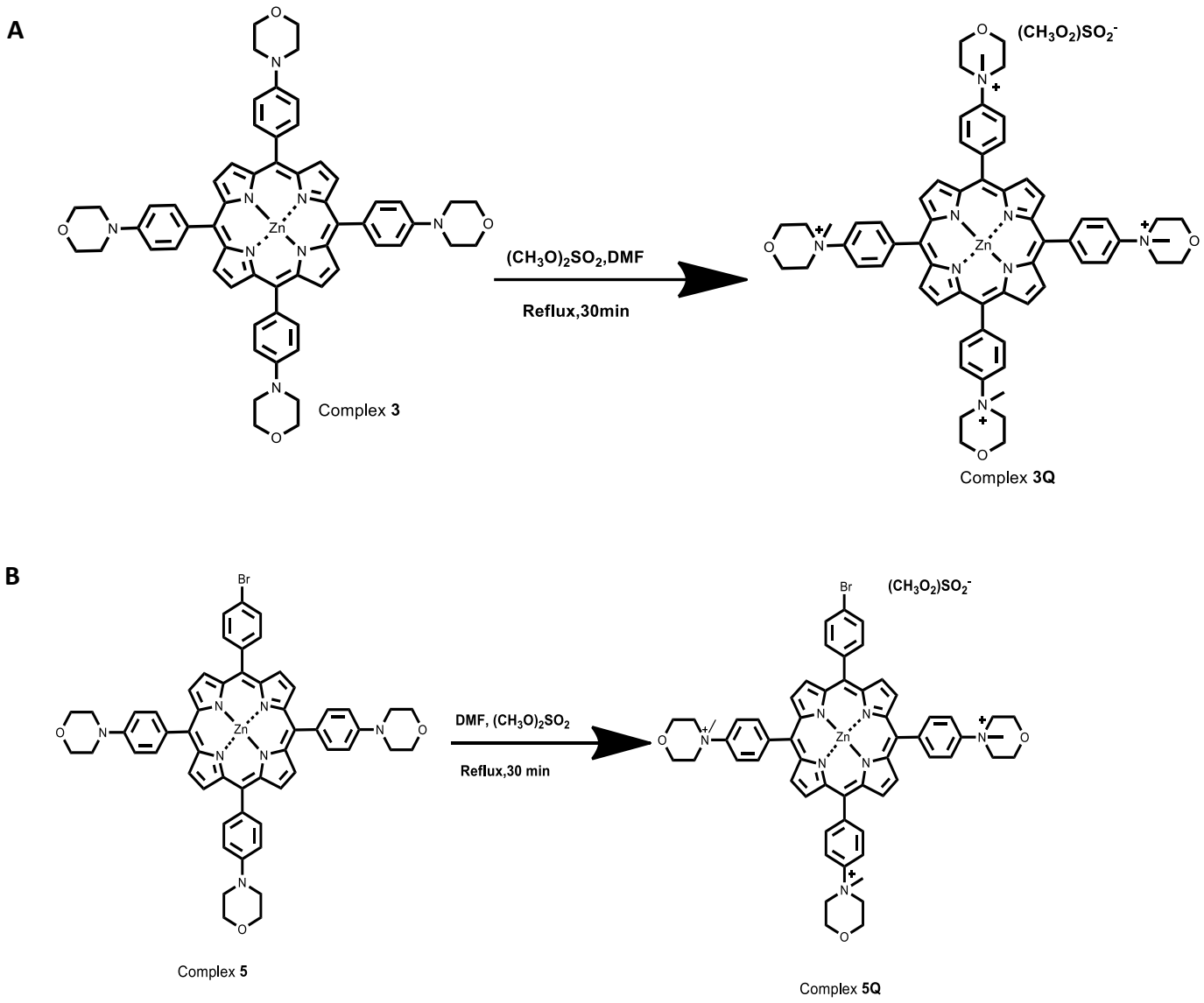

Scheme 4.5. Quaternization of porphyrin complexes (A) **3** and (B) **5** to cationic complexes **3Q** and **5Q.**

All the porphyrin complexes were characterized using MALTI-TOF mass spectra (Appendix 1-7), ^{1}H proton NMR (Appendix 8-14), Fourier-transform infrared spectroscopy (FT-IR), and UV-Visible spectroscopy. ^{1}H NMR spectrum for complex **1** showed 56H that is -2H of what was expected, these 2H are from the inner NH protons, and it is reported in literature that usually

the inner NH protons of porphyrins are strongly shielded due to the ring currents, reflecting the aromaticity of porphyrins **[67]**. For complex **2** the number of protons obtained was 56H being shot of 2H from the axial ligand and this is due to the fact that they are highly shielded **[68]**. Complex **3** gave 56H as expected, and for complex **3Q** the number of protons obtained were 71H as expected. NMR spectrum of complex **4** gave 48 H, but the expected number of protons was 50H where the 2H (NH) from the core of porphyrin were not observed on the NMR spectrum due to strong shielding **[67]**. Complex **5** gave 48H as expected, and the spectrum of **5Q** resulted in 57H as expected this was with addition of 9H when compared to complex **5** which are from the methyl groups from the quaternizing agent. From the MALTI-TOF, the molecular peak ion was observed at m/z = 956.12 for complex **1** that is $[M+2H]^+$of what was expected, and at m/z = 1105.35 for complex **2** that is $[M+H]^+$ of what was expected. The molecular peak ion was observed at m/z = 1017.93 for complex **3** that is $[M+H]^+$of what was expected, complex **3Q** m/z the expected mass was 269 and the mass obtained was 266 which is $[M+3H]^+$. The calculated MALDI-TOF MS of complex **4** was 947.32 and found was 946.04 $[M+H^+]$ which was short of 1H, and for complex **5** the calculated mass was 1011.23, and found was 1011.68 as expected. Complex **5Q**, the calculated mass was 451.23, and the mass found was 567.48 $[M+(DMSO.2H_2O)]^+$ where the expected mass of 451.23 had an addition of water and DMSO, and the mass was run in DMSO **[69]**.

The UV-vis spectra of all the porphyrin complexes were performed in DMSO. The free base porphyrins complexes (**1** and **4**) spectra showed Soret bands and four less intense Q -bands, Fig 4.1. The Soret band of complex **1** absorbed at 428 nm and for complex **4** at 426 nm, Table 4.1. Complex **1** was slightly red shifted when compared to complex **4**, because it contains two electron rich elements which are nitrogen and oxygen on all the substituents of the porphyrin that result in red shift of the absorption band **[70]** as shown in Fig 4.1, Table 4.1.

Table 4.1 UV-vis maximum absorbance of the complexes and conjugates in DMSO.

Complexes	λ_{max}**(nm)**[(a)] **Soret band**
NGQDs	(337)
B-NGQDs	(331)
FA-BGQDs	(356)
1	428
2	445
3	432
3Q	435
4	426
5	427
5Q	429
3-FA-NGQDs	437 (346)
3Q-FA-BNGQDs	419 (346)
2-B-NGQDs	441 (314)
3-B-NGQDs	437 (331)
3Q-B-NGQDs	429 (331)
5-B-NGQDs	430 (331)
5Q-B-NGQDs	419 (331)

[(a)] Values in brackets are for NGQDs

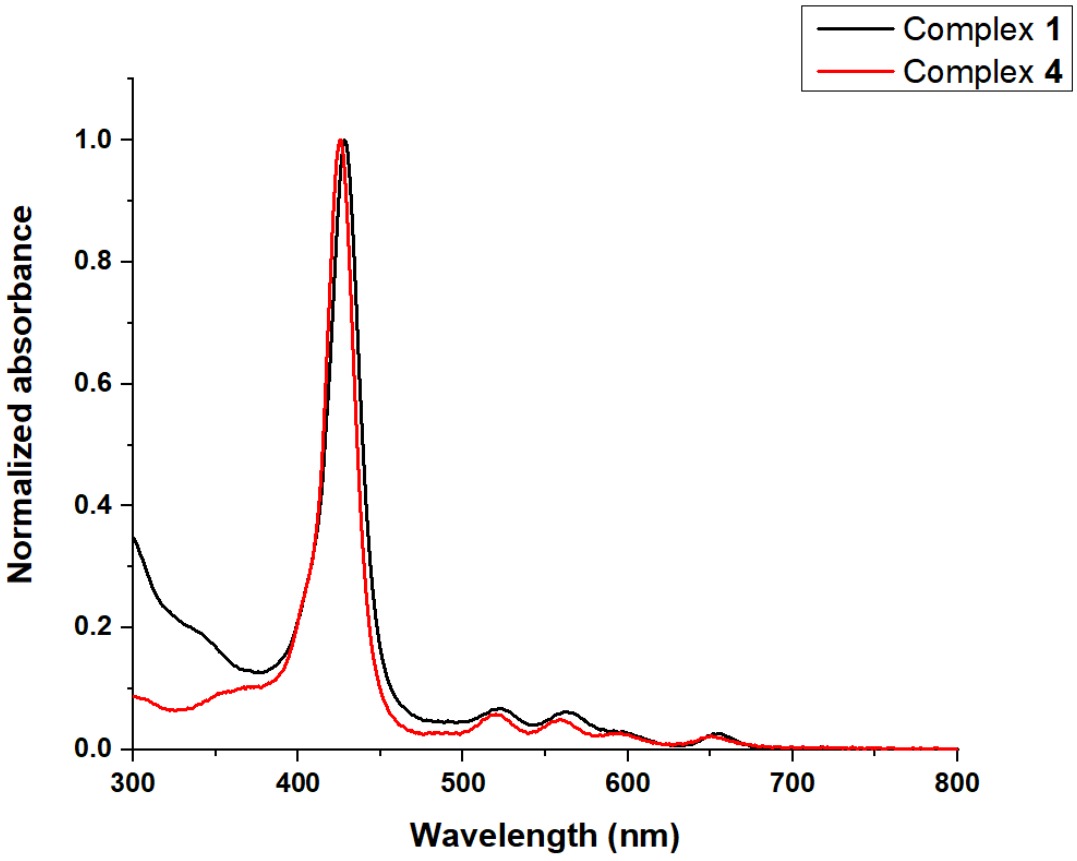

Fig 4.1. Uv-vis spectra of complexes **1** and **4**.

Upon metalation of complex **1** to give complexes **2** and **3**, it was observed that the four Q-bands of complex **1** merged into two and the Soret band was red shifted. Introduction of heavy metals results in degree of perturbation and electron delocalisation within the porphyrin macrocycle, resulting in red shift of the Soret band **[71]**. Complex **2** was red shifted compared to complex **3** as Sn is heavier metal than Zn with observed wavelengths of 445 nm and 432 nm respectively at the Soret band (Fig 4.2**.** (A)), Table 4.1. Slight red shift was also observed upon quaternization of complex **3** to **3Q** (436 nm), and complex **5** to **5Q** (429 nm) this is due to the presence of heavy atom sulfur from the quaternizing agent (Fig 4.2. (B)).

A

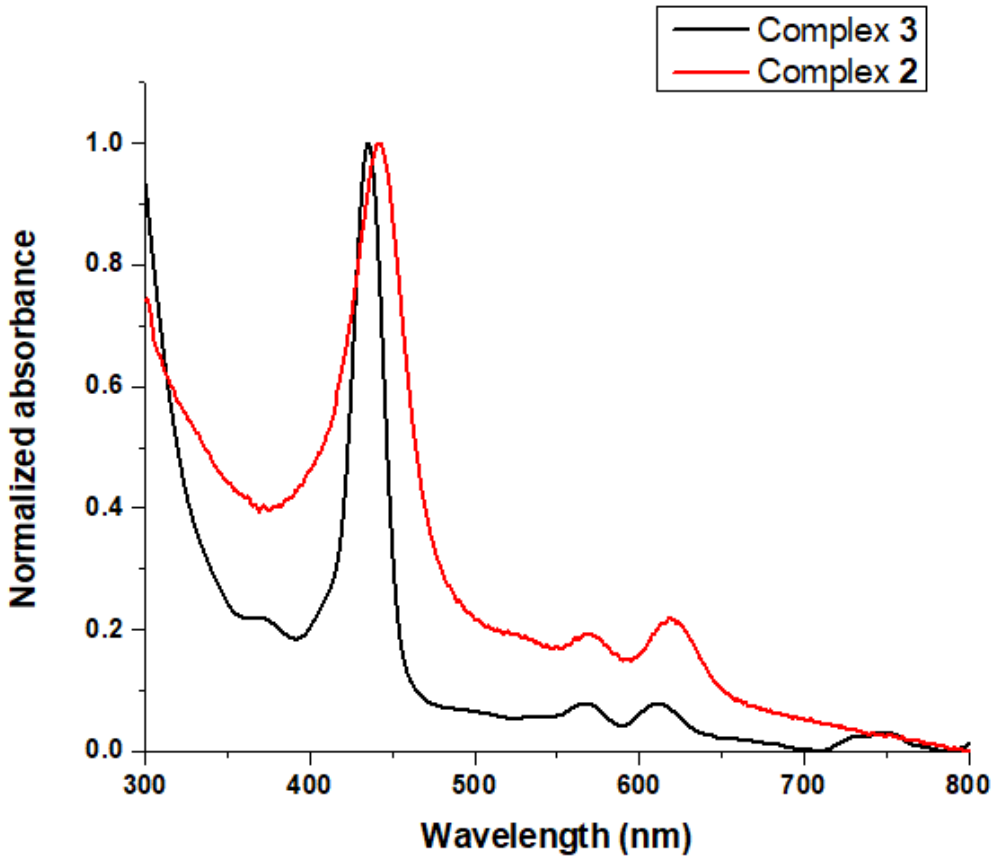

B

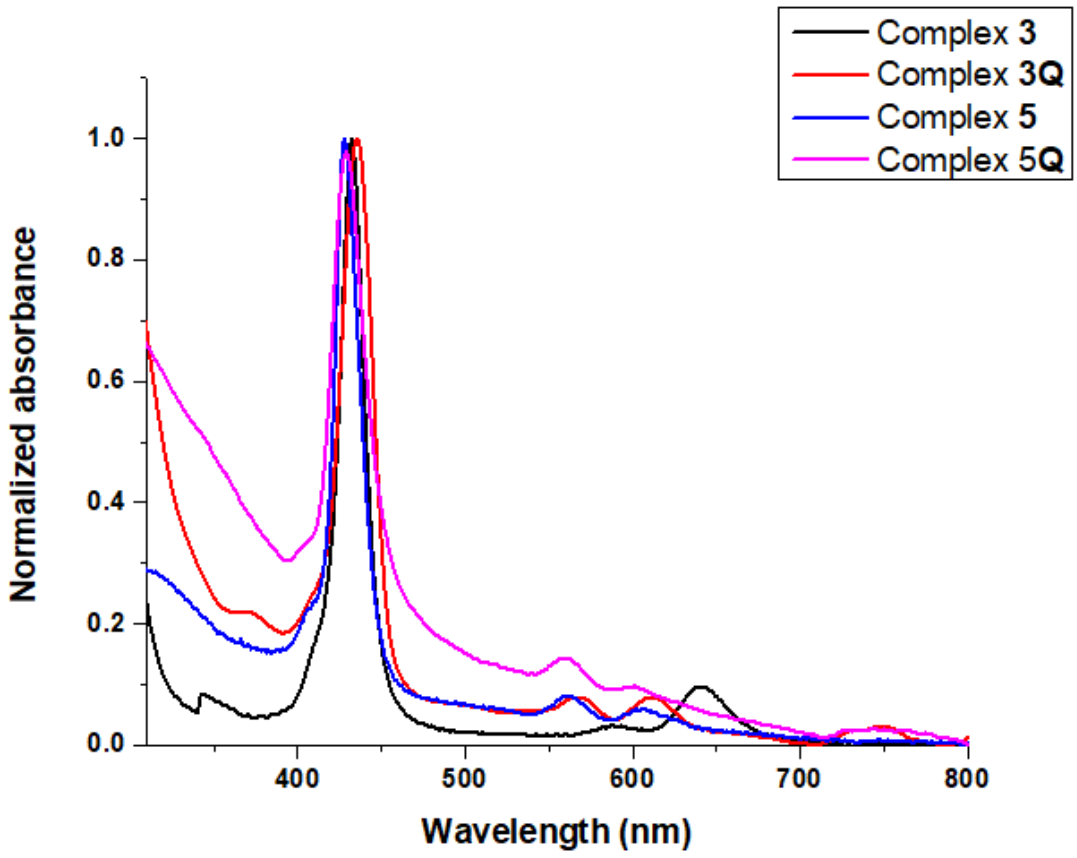

Fig 4.2. Uv-Vis spectra of complexes (A) **2** and **3**, (B) **3**,**3Q**,**5**, and **5Q**.

4.2 Formation of conjugates

4.2.1 Amide bond formation of B-NGQDs and FA-NGQDs

The presence functional groups on the surface and edges of the NGQDs enable different types of bonds to form with other suitable moieties. The NGQDs were functionalized with two different biomolecules through an amide bond using the NH_2 from the NGQDs to bond with COOH moiety from the biomolecules. The first biomolecule used was biotin where its carboxy moiety was activated using DCC and DMAP in DMF by stirring at room temperature for 4h. To this mixture NGQDs were added and allowed to stir to further 48h to form B-NGQDs, Scheme 4.6 (A). Folic acid was also used to bond with NGQDs through an amide bond, the similar procedure from the above was followed with slight modifications as outlined in chapter **2** to form FA-NGQDs, Scheme 4.6 (B).

A

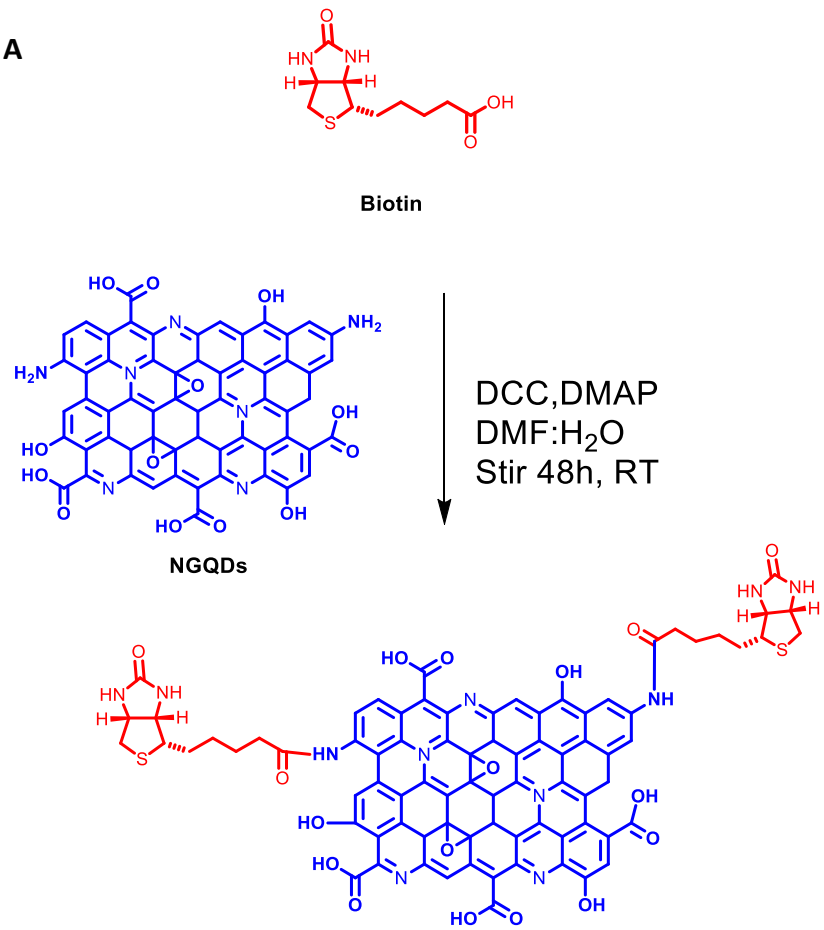

B

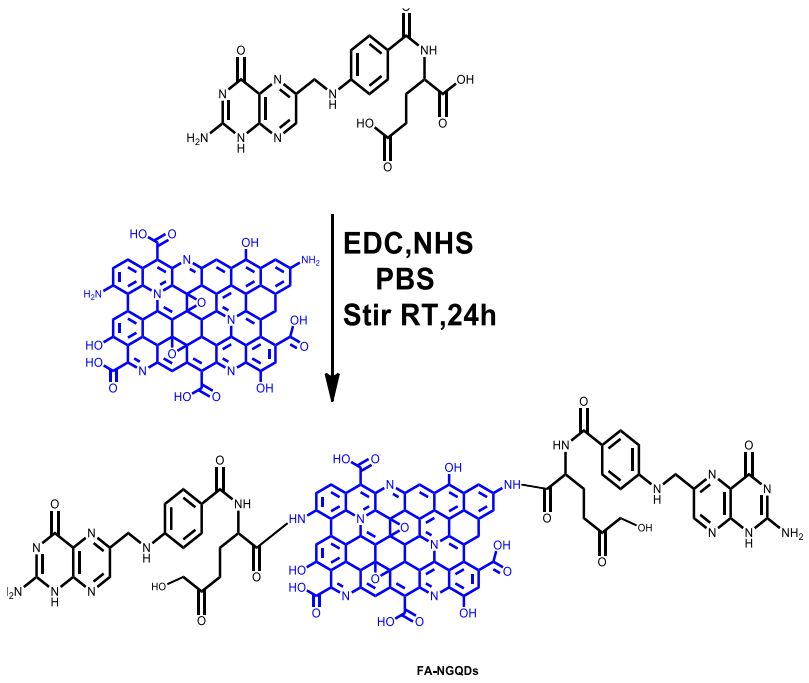

Scheme 4.6. Synthetic pathway of (A) B-NGQDs, and (B) FA-NGQDs

4.2.2 Ester bond for complex 2 to B-NGQDs

The conjugation of complex **2** to B-NGQDs was performed following the method reported **[65]**, where both compounds were refluxed for 72h in DMF to form an ester bond between the COOH moiety of the B-NGQDs and the OH of complex **2**. This resulted in conjugation of **2**-B-NGQDs (Scheme 4.7).

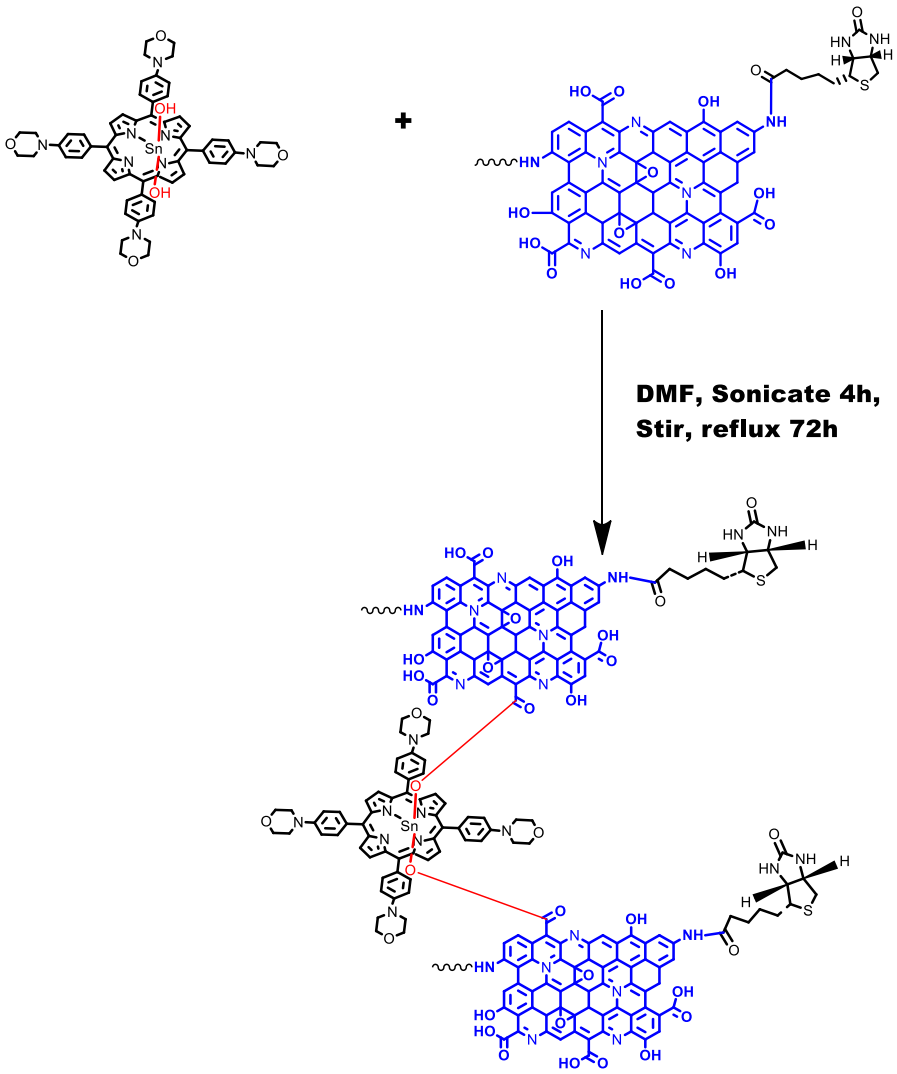

Scheme 4.7. Synthetic pathway of **2**-B-NGQDs through an ester bond

4.2.3 π-π stacking

NGQDs have the π system which enable $\pi - \pi$ stacking with molecules containing π electrons. Therefore, FA-NGQDs were conjugated to **3** and **3Q** through $\pi - \pi$ stacking as porphyrins are also π system molecules to give **3**-FA-NGQs and **3Q**- FA-NGQDs (Scheme 4.8 (A)). The prepared B-NGQDs were also conjugated to complexes **3**, **3Q**, **5**, and **5Q** through π-π stacking (Scheme 4.8 (B)).

A

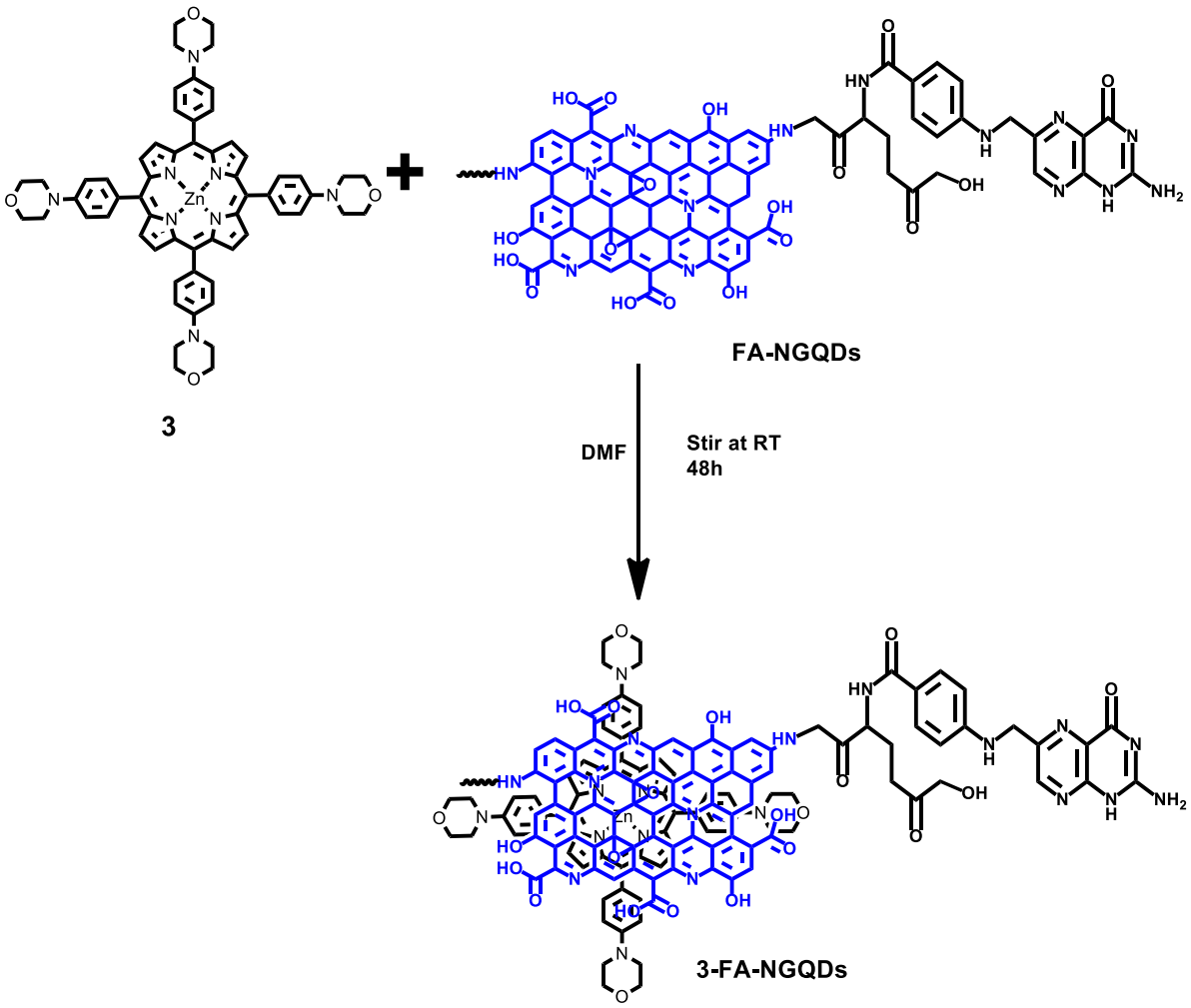

B

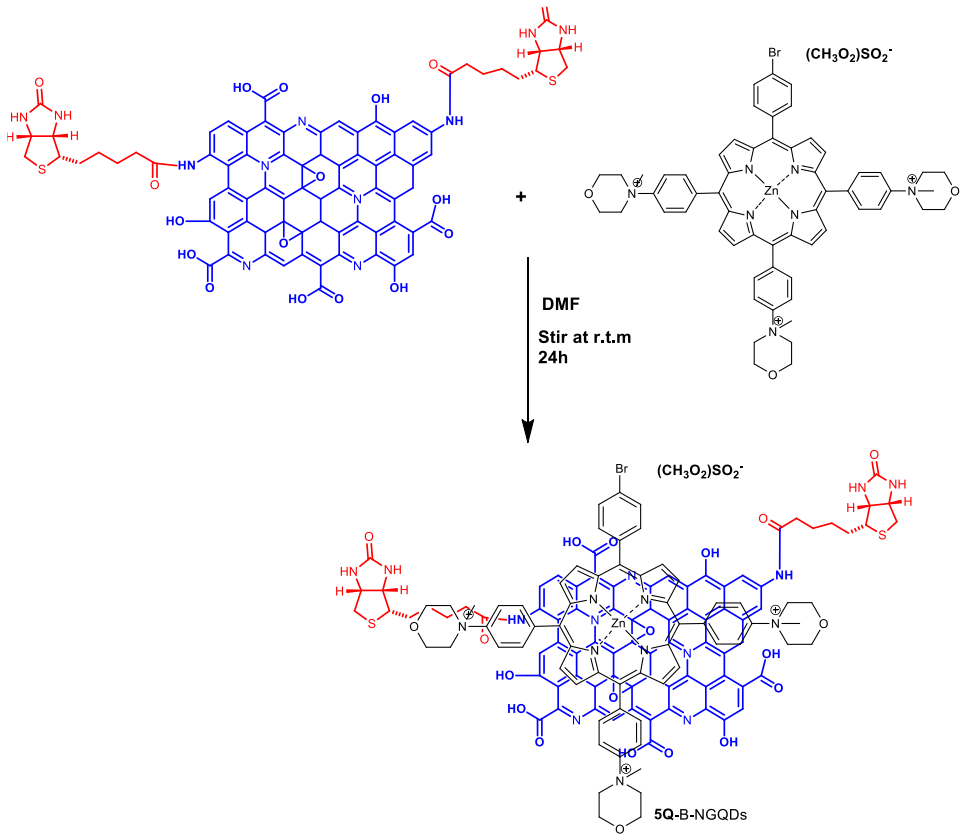

Scheme 4.8. Representation of the ππ stacking using (A) complex **3** as an example with FA-NGQDs to form **3**-FA-NGQDs and (B) complex **5Q** as an example with B-NGQDs to form **5Q**- B-NGQDs.

4.3 Characterization of conjugates

The conjugates were characterized with the following characterization techniques: ultraviolet-visible spectroscopy (Uv-vis), transmission electron microscope (TEM), dynamic light scattering (DLS), energy dispersive spectroscopy (EDS), Fourier transform infrared (FT-IR), Raman spectroscopy, X-ray diffraction (XRD), and X-ray photoelectron spectroscopy (XPS).

4.3.1 Ultraviolet-visible spectroscopy

NGQDs had absorption at 337 nm, and after covalent linking NGQDs to biotin the absorption of biotin decorated NGQDs (B-NGQDs) was observed at 331 nm which is blue shifted by 6 nm when compared to NGQDs alone (Fig 4.3 (A)), Table 4.1. Moreover, upon conjugation of NGQDs to the folic acid (FA-NGQDs) the peak shifted to 356 nm (Fig 4.3 (A)). This red shift is caused by an increase in sp^2 C (C-C/C=C) from the folic acid **[64]**. The conjugate, **2**-B-NGQDs had a peak at 314 nm that was from B-NGQDs which is blue shifted by 17 nm compared to B-NGQDs at 331 nm (Fig 4.3 (B)), Table 4.1. The blue shift is evidence of strong interaction between the porphyrin and GQDs **[71].** A slight blue shift on the Soret band of **2**-B-NGQDs compared to complex **2** alone was also observed and this could be due to close packing attributed to the orientation of metalloporphyrins on the surface of the nanoparticles **[73-75]**. Conjugates **3**-B-NGQDs, **3Q**-B-NGQDs, **5**-B-NGQDs, and **5Q** -B-NGQDs showed the presence of B-NGQDs at 331 nm. For **3**-B-NGQDs and **5**-B-NGQDs the Soret bands were red shifted when compared to the porphyrins only with complex **3** from 432 nm to 437 nm **3**-B-NGQDs (Fig 4.3 (C)), and complex **5** from 427 nm to 430 nm **5**-B-NGQDs (Fig 4.3 (D)). Red shifting could be due to J- aggregation which is associated with red shifting in porphyrins and can also observed for distorted porphyrins **[76,77].** The Soret band for **3Q**-B-NGQDs and **5Q**-B-NGQDs showed blue shifting when compared to their complexes only which suggest strong interaction between the porphyrin and B-NGQDs. The Soret band of complex **3**-FA-NGQDs was observed at 437 nm resulting in a red shift by 5 nm compared to complex **3** alone**.** Complex **3Q**-FA-NGQDs Soret band absorbed at 419 nm resulted in blue shift by 16 nm compared to complex **3Q** alone, and blue shift suggest strong interaction between complex **3Q** and FA-NGQDs (Fig 4.3 (E)).

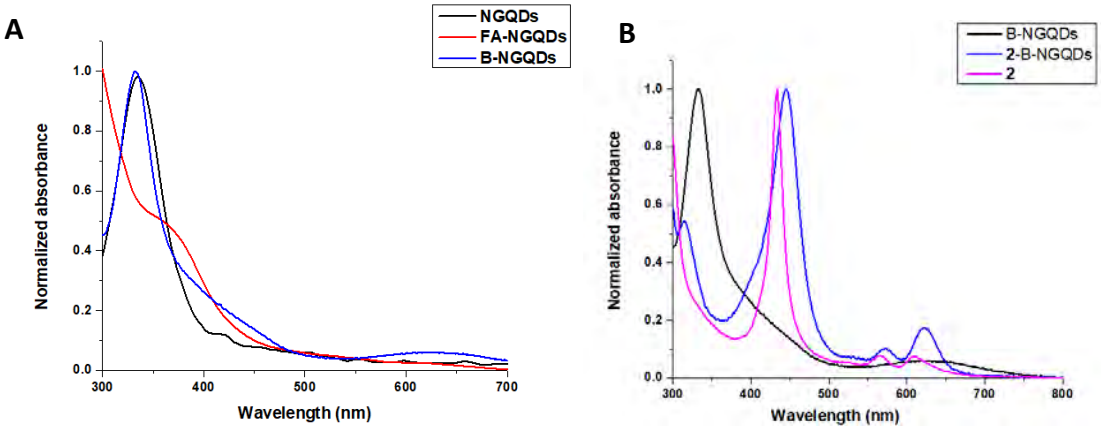

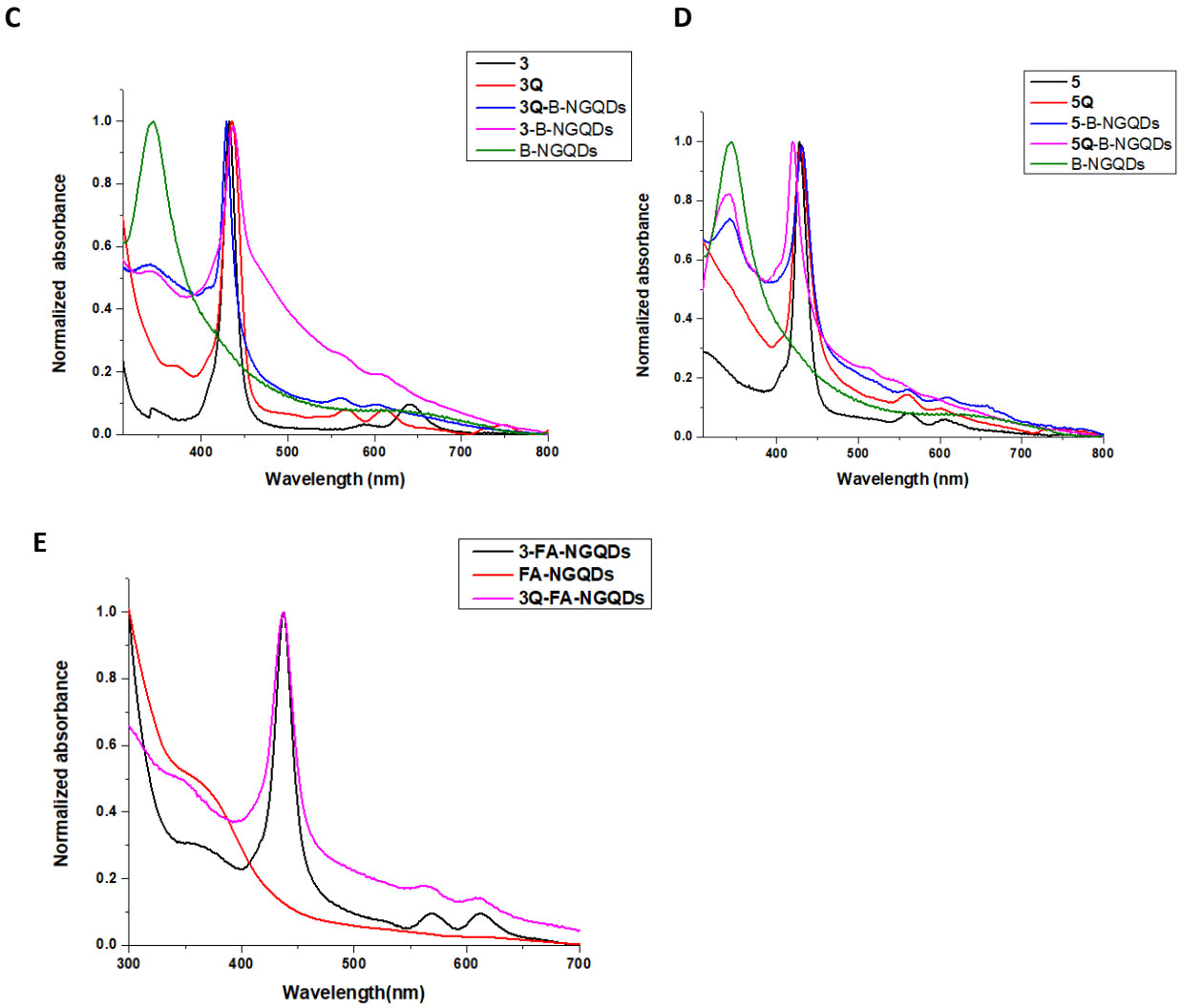

Fig 4.3. UV-Vis spectra (DMSO) of (A) NGQDs, B-NGQDs, FA-NGQDs, (B) **2** and its conjugates, (C) **3** and its B-NGQDs conjugates, (D) **5** and its conjugates and (E) **3** and its conjugates.

4.3.2 Energy dispersive X-ray (EDX)

EDX spectra analysis was used to determine the elemental compositions for complexes and conjugates, Fig 4.4. For the NGQDs all the expected elements were observed which are carbon, nitrogen, and oxygen, but there was also presence of Na which was from sodium hydroxide that was used in the synthesis to neutralize the pH of the NGQDs. The decoration of NGQDs with biotin (B-NGQDs) resulted in the appearance of the S peak which confirms the presence of biotin in NGQDs. FA-NGQDs also showed all the expected elements. Complex **2** and the conjugate showed the expected elemental peaks, and Sn peak. In the conjugate (**2**-B-NGQDs) all the peaks observed in complex **2** and in B-NGQDs were observed. In complex **3** the presence of Zn was observed with other expected elements, and for complex **3Q** there was presence of all elements observed in **3** and sulfur which is from the quaternizing reagent. It was observed that both the elements observed in FA-NGQDs alone and **3** were observed in **3**-FA-NGQDs. All the expected elements in **3Q**-FA-NGQDs were observed.

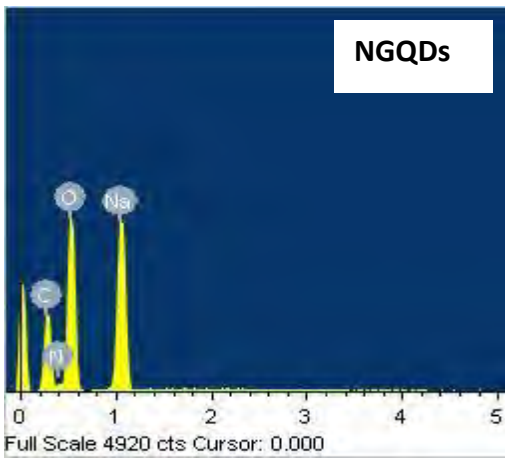

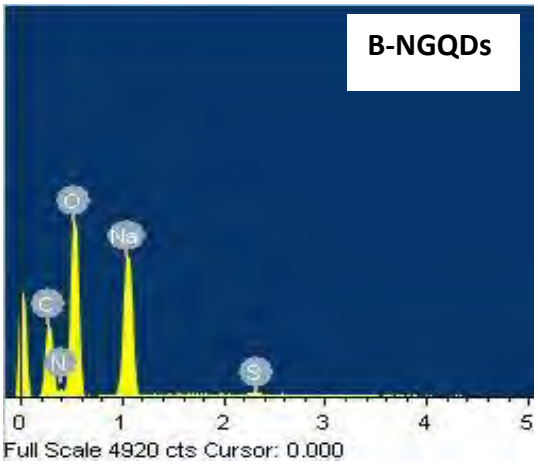

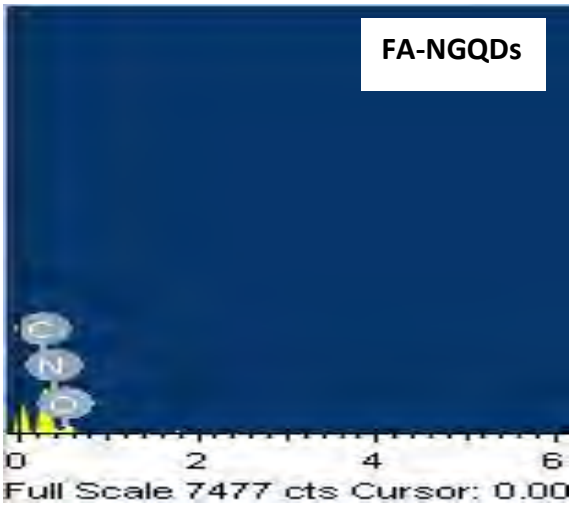
FA-NGQDs
C
N
O
0
2
4
6
Full Scale 7477 cts Cursor: 0.00

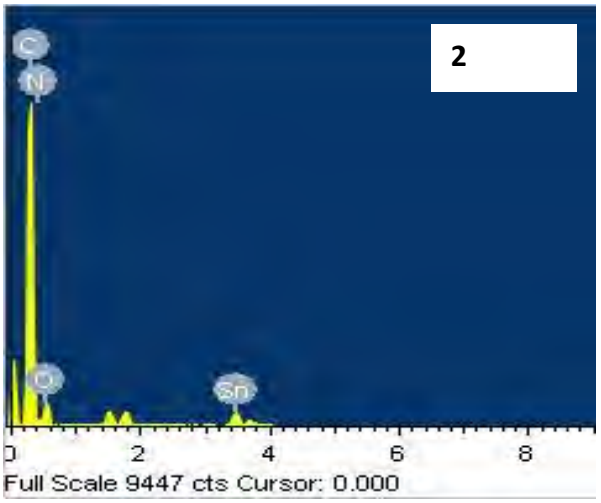
2
C
N
O
Sn
0
2
4
6
8
Full Scale 9447 cts Cursor: 0.000

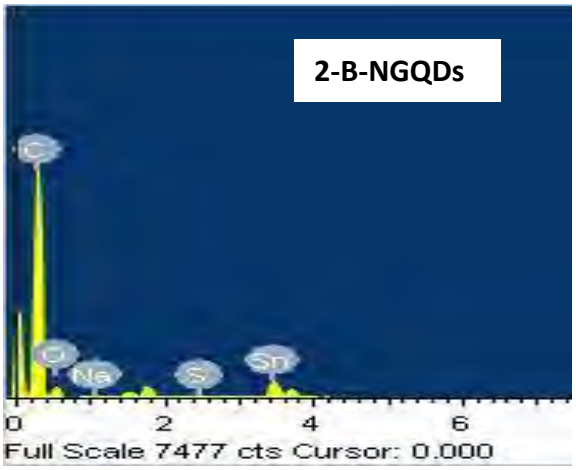
2-B-NGQDs
C
O
Na
S
Sn
0
2
4
6
Full Scale 7477 cts Cursor: 0.000

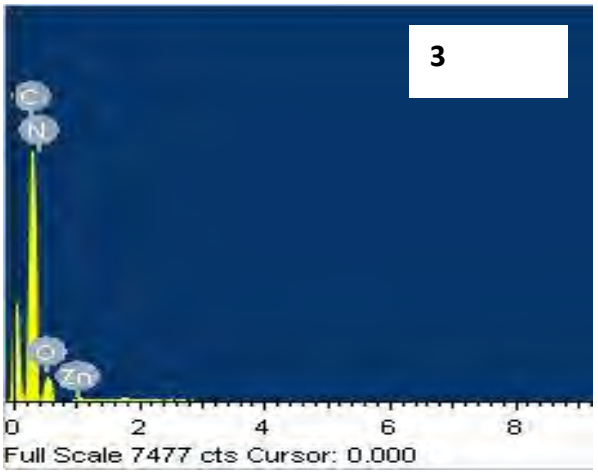
3
C
N
O
Zn
0
2
4
6
8
Full Scale 7477 cts Cursor: 0.000

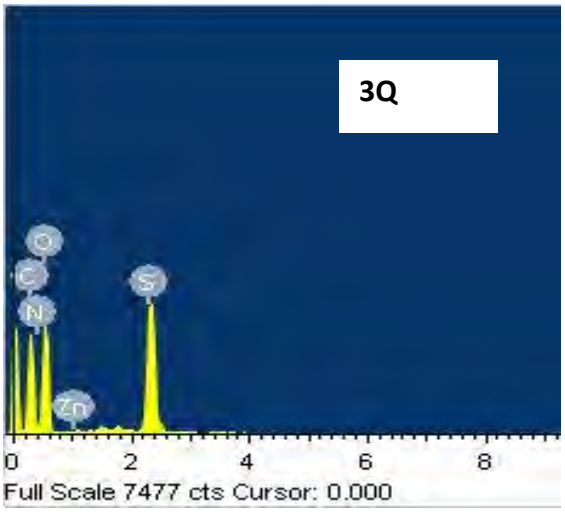
3Q
O
C
N
S
Zn
0
2
4
6
8
Full Scale 7477 cts Cursor: 0.000

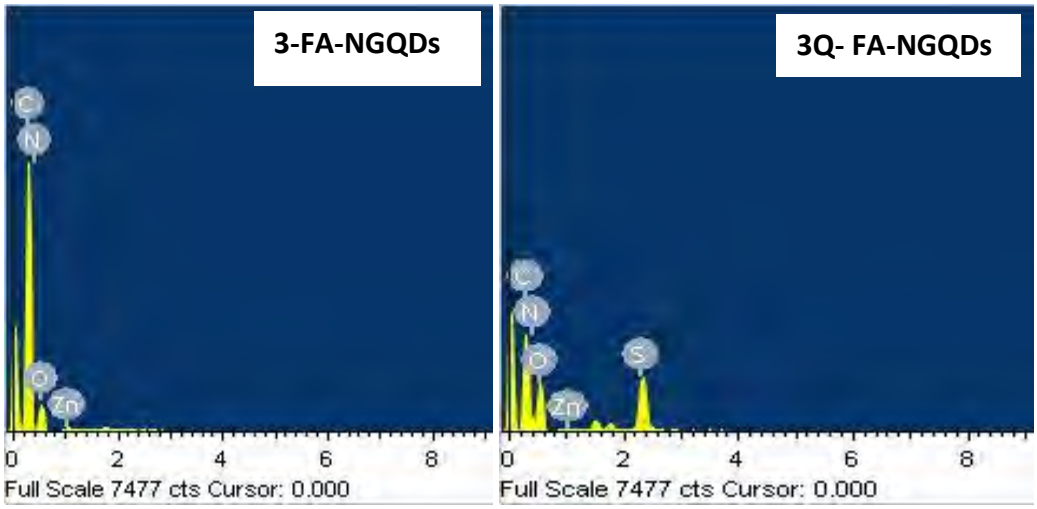

Fig 4.4. EDX spectra analysis of NGQDs, B-NGQDs, FA-NGQDs and their conjugates.

4.3.3 Transmission electron microscopy (TEM)

Transmission electron microscopy (TEM) was used for morphological analysis and to estimate the shape, size distribution and particle sizes, Fig 4.5. It was observed that the NGQDs were circular in shape, and there was size increase upon the covalent linking of biotin and NGQDs (B-NGQDs) and upon conjugation with the porphyrin (**2**-B-NGQDs) as well. The TEM images for FA-NGQDs showed well defined spherical shapes with an average diameter for 14.2 nm, for **3**-FA-NGQDs, and **3Q**-FA-NGQDs the average sizes are 14.6 nm, and 16.1 nm, respectively (Table 4.2). An increase for all compared to NGQDs at 4.2 nm. A huge increase in size upon the conjugation could be due to aggregation, because porphyrins are known to aggregate.

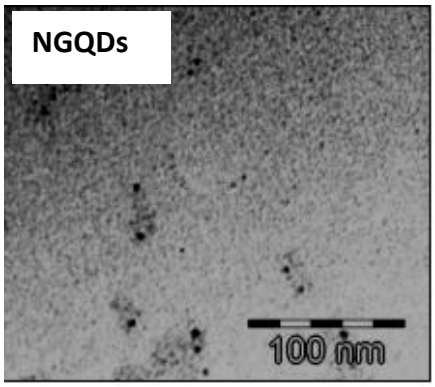

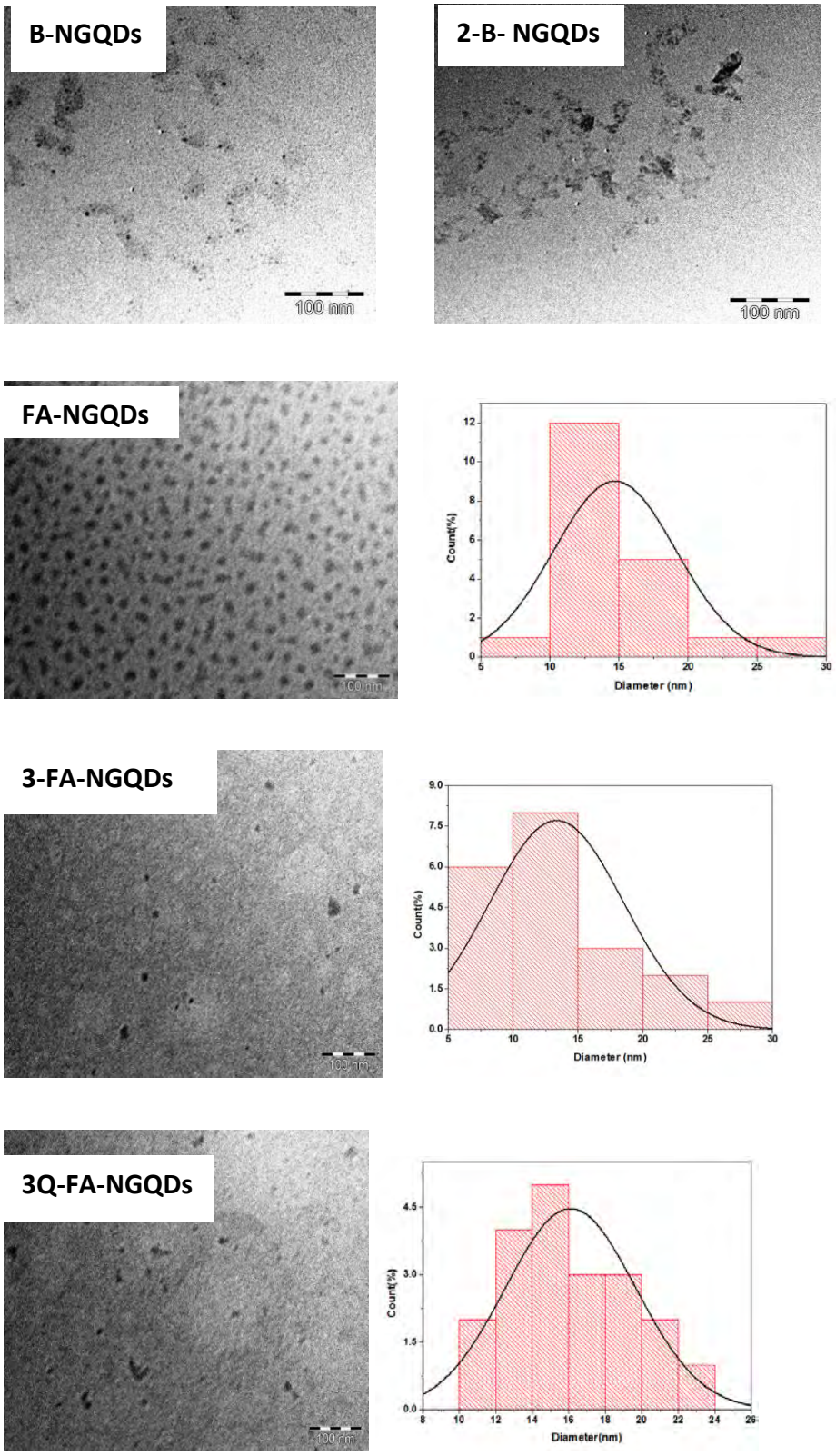

Fig 4.5. Transmission electron microscopy (TEM) micrographs and corresponding histogram size distribution curve of NGQDs, FA-NGQDs, B-NGQDs and their conjugates.

4.3.4 Dynamic Scattering Light (DLS) and Zeta potential measurements

Dynamic light scattering (DLS) was used to determine the average particle distribution. The average diameter of NGQDs obtained was 4.2 nm, for B-NGQDs was 8.7 nm and for **2**-B-NGQDs was 28.0 nm, (Fig 4.6 (A), Table 4.2). Upon the conjugation of **2** to B-NGQDs there was a huge increase in size, and this is probably due to interactions between the porphyrins on adjacent B-NGQDs. It was observed that the unquaternized porphyrin conjugates (**5**-B-NGQDs and **3**-B-NGQDs) resulted in bigger sizes when compared to cationic conjugates (**5Q**-B-NGQDs and **3Q**-B-NGQDs) (Fig 4.6 (B)), Table 4.2. This is due to that the study was performed in water and the unquaternized porphyrins were not soluble which resulted in bigger size. The average diameters in (Fig 4.6 (C)), Table 4.2 are 15.7 nm, 24.3 nm, and 32.2 nm for FA-NGQDs, **2**-FA-NGQDs, and **3**-FA-NGQDs respectively. The increase in size of the conjugates compared to NGQDs alone shows the formation of supramolecular assemblies of NGQDs and the porphyrin. Discrepancies in particle size determined by TEM and DLS could be attributed to interference of the dispersant into hydrodynamic diameter, resulting in higher values for DLS **[78]**.

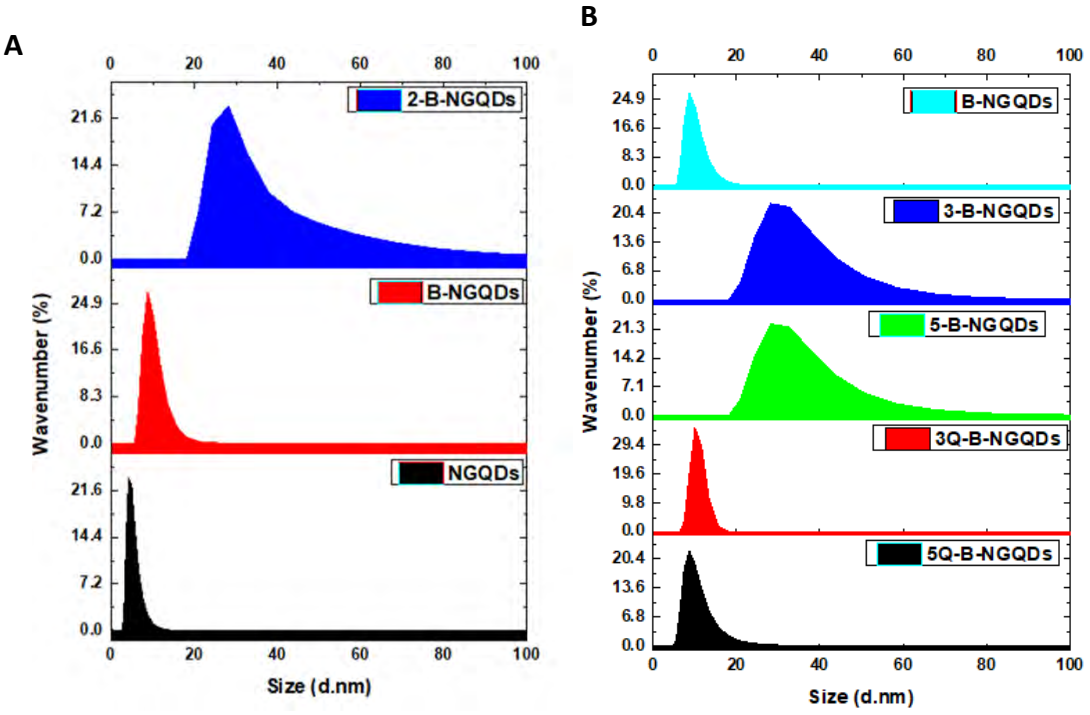

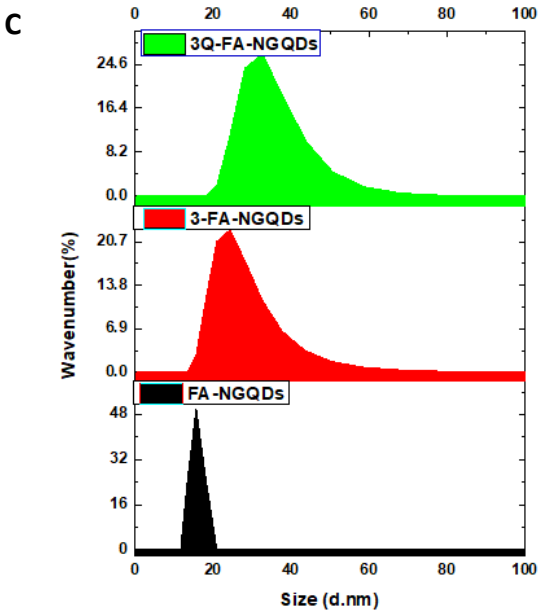

Fig 4.6. Dynamic light scattering (DLS) distribution curve for (A) NGQDs and its conjugates, (B) B-NGQDs and its conjugates, and (C) FA-NGQDs and its conjugates.

Different properties of nanoparticles and nanoconjugates such as size, polydispersity index (PDI), and zeta potential play an important role in their physicochemical and biological properties **[79].** The zeta potential and PDI of the NGQDs and conjugates were measured using DLS (Table 4.2). Zeta potential (ζ) is a measure of charge carried by particles suspended in a liquid, it indicates the stability of colloidal dispersion. The degree of electrostatic repulsion between adjacent particles is indicated by the magnitude of zeta potential**.** The high zeta potential value (regardless of charge) indicates the stability, and the smaller value indicates that attractive forces exceed repulsion which results in aggregation **[80-84]**, the zeta potentials of NGQDs obtained was (-7.1 mV), B-NGQDs (-21.0 mV), and **2**-B-NGQDs (-23.0 mV). Thus, an increase was observed following the conjugation of biotin to NGQDs and of **2** to B-NGQDs, implying improved stability. The negative zeta potential values for B-NGQDs, **3**-B-NGQDs and **2**-B-NGQDs originate from dissociated carboxyl groups of the B-NGQDs. The positive zeta potentials for **3Q**-B-NGQDs and **5Q**-B-NGQDs could be a result of the quaternization of porphyrins. Compounds with a positive zeta potential (**3Q**-B-NGQDs and **5Q**-B-NGQDs) will bind to negatively charged surface of the cell and this is important for this study. FA-NGQDs (-18.5 mV) is more stable than NGQDs (-7.1 mV) and the stability of the

former is reduced in the presence of porphyrins. Poly dispersity index (PDI) is a representation of the distribution of size populations within a given sample **[85]**, and the PDI values (Table 4.2) obtained for NGQDs, FA-NGQDs, B-NGQDs, **3**-B-NGQDs, **3Q**- B-NGQDs, and **5Q**-B-NGQDs signify broad particle size distribution. The values of **2**-B-NGQDs, **5**-B-NGQDs, **3**-FA-NGQDs, and **3Q**-FA-NGQDs signify monomodal dispersions.

Table 4.2 Nanoparticle, and nanoconjugates sizes and Zeta potential values.

Complex/conjugate	**DLS size (nm)**	**TEM size (nm)**	**ζ (mV)**	**PDI**	**Raman (I_D/I_G)**
NGQDs	4.2	3.0	-7.1	1.00	0.86
B-NGQDs	8.7	5.5	-21.0	0.75	0.93
FA-NGQDs	15.7	14.2	-18.5	0.92	0.73
2-B-NGQDs	28.0	13.4	-23.0	0.63	2.57
3-B-NGQDs	28.5	-	-7.4	1.00	0.33
3Q-B-NGQDs	10.2	-	0.6	1.00	0.36
5-B-NGQDs	28.5	-	-3.4	0.31	0.64
5Q-B-NGQDs	9.9	-	0.01	1.00	0.22
3-FA-NGQDs	24.3	14.6	-13.5	0.64	0.85
3Q-FA-NGQDs	32.2	16.1	7.6	0.49	0.51

"-" not determined

4.3.5 X-ray photoelectron spectroscopy (XPS)

X-ray photoelectron spectroscopy (XPS) analysis was carried out to probe the structural compositions of the NGQDs and functionalised biotin, Fig. 4.7.

Wide scan XPS spectrum of NGQDs in (Fig.4.7 (A)) shows C1s, N1s, and O1s signals at 285.2, 396.9 eV and 531.9 and, respectively. Na auger peak at 494.4 eV as the result of NaOH employed in the NGQDs synthesis. The O (1s) peak is related to ester and hydroxyl groups bonded to aromatics which is the case on the NGQDs and B-NGQDs **[86]**. The C 1s peak of NGQDs can be deconvoluted into peaks centred at 284.5 (C=C, C-N, C-O), 285.0 (C-OH), 286.4 (C-N) and 288.2 eV (C=O) **[87]**. The C-N peak at 286.4 eV indicates that N is covalently bonded to C which suggest successful doping **[88]**. The C 1s peak of B-NGQDs can be deconvoluted into peaks centred at 284.5 eV (C-C, C-N, C-O), 285.9 eV (C-OH), 287.9 eV (C-O-C) **[87]**. The N 1s peaks of NGQDs can be deconvoluted into peaks centred at 398.0, and 399.1, corresponding to pyridinic (398.0 eV) **[88]**, amino (399.1) **[89].** The XPS N 1s peak for B-NGQDs can be deconvoluted into peaks centred at 398.0, 399.4, and 401.2 eV, corresponding to pyridinic **[89]**, O=C-N **[90]**, and N-H **[91,92],** respectively, Fig. 4.7 (C).

The pyridinic composition is dominant relative to amino functional group for NGQDs. The disappearance of primary amine functional groups NH_2 (for NGQDs) to NH (for B-NGQDs) confirm the successful formation of the amide bond and the formation of B-NGQDs. The O 1s peak of NGQDs can be deconvoluted into peaks centred at 590.0 eV (metal oxide from Na auger), 530.4 eV (C=O), and 533.1 eV (C-O-C), and the O 1s peaks of B-NGQDs can deconvoluted into peaks centred at 528.9 eV (metal oxide from Na auger), 530.2 eV (C=O), and 533.1 (C-O-C).

A

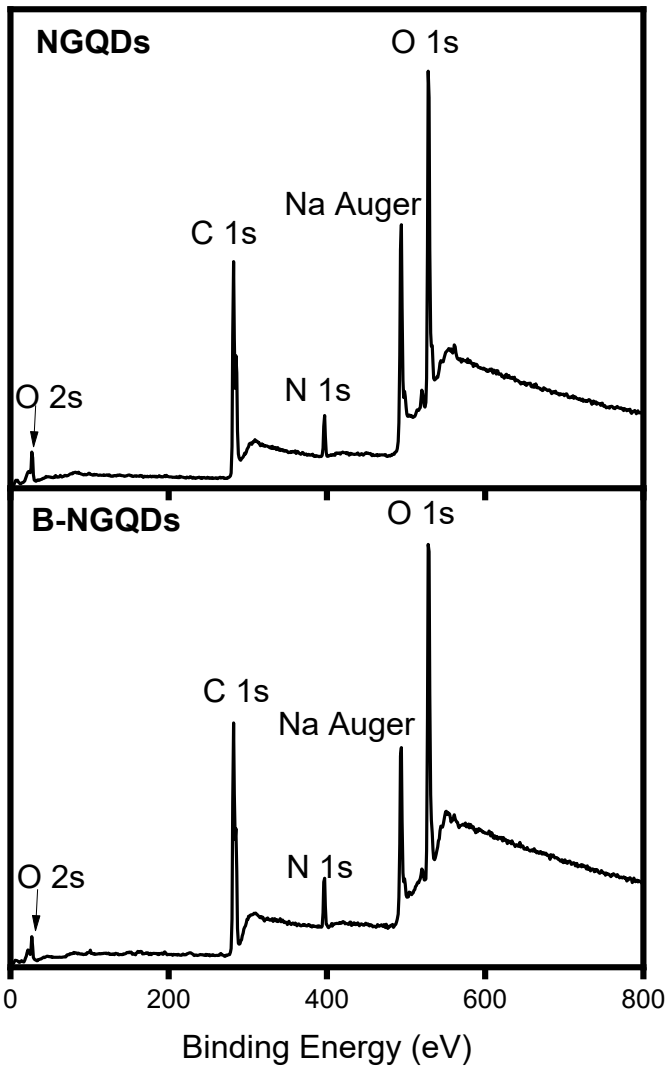
NGQDs
O 1s
Na Auger
C 1s
O 2s
N 1s
B-NGQDs
O 1s
C 1s
Na Auger
O 2s
N 1s
0
200
400
600
800
Binding Energy (eV)

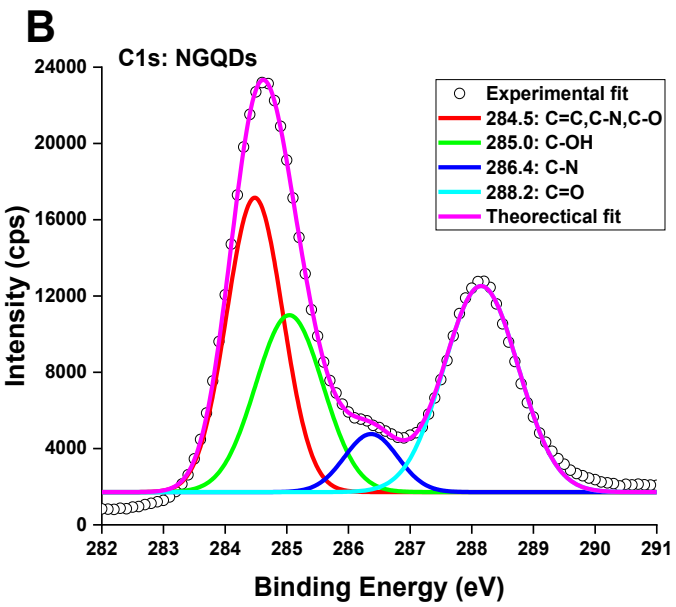
B
C1s: NGQDs
Experimental fit
284.5: C=C,C-N,C-O
285.0: C-OH
286.4: C-N
288.2: C=O
Theorectical fit
Intensity (cps)
Binding Energy (eV)

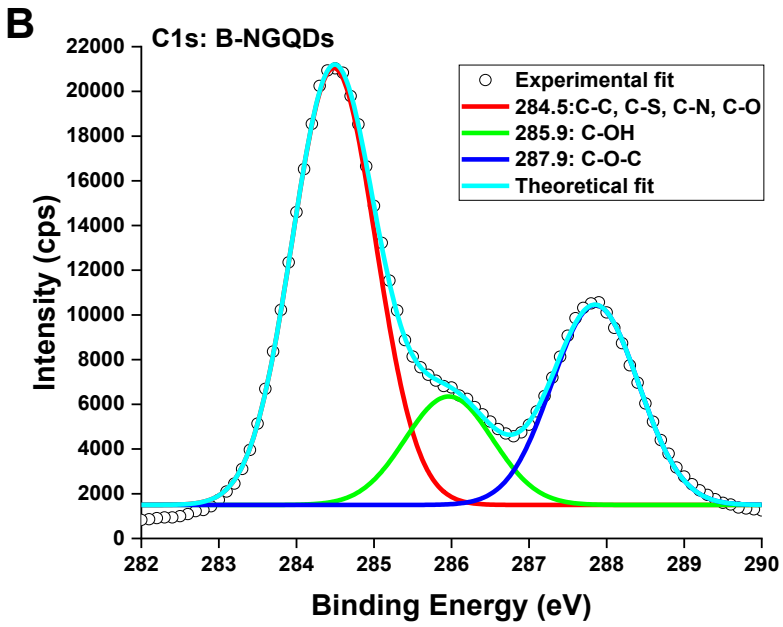
B
C1s: B-NGQDs
Experimental fit
284.5:C-C, C-S, C-N, C-O
285.9: C-OH
287.9: C-O-C
Theoretical fit
Intensity (cps)
Binding Energy (eV)

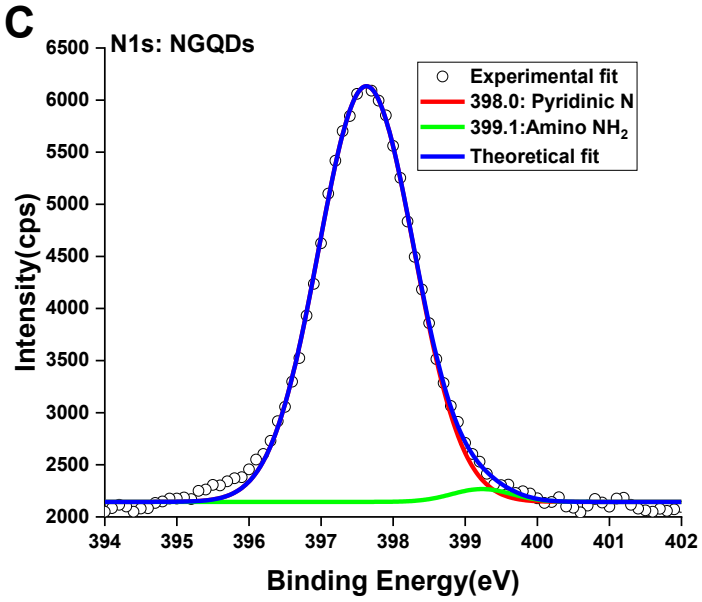
C
N1s: NGQDs
Experimental fit
398.0: Pyridinic N
399.1:Amino NH2
Theoretical fit
Intensity(cps)
Binding Energy(eV)
6500
6000
5500
5000
4500
4000
3500
3000
2500
2000
394
395
396
397
398
399
400
401
402

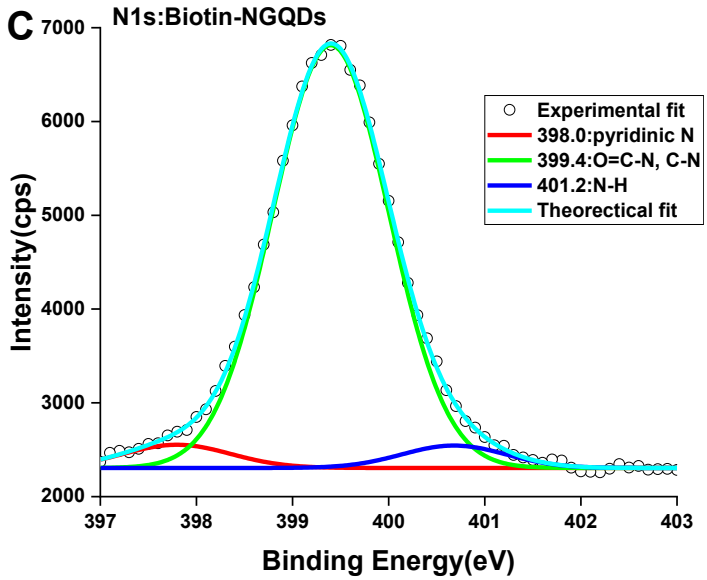
C
N1s:Biotin-NGQDs
Experimental fit
398.0:pyridinic N
399.4:O=C-N, C-N
401.2:N-H
Theorectical fit
Intensity(cps)
Binding Energy(eV)
7000
6000
5000
4000
3000
2000
397
398
399
400
401
402
403

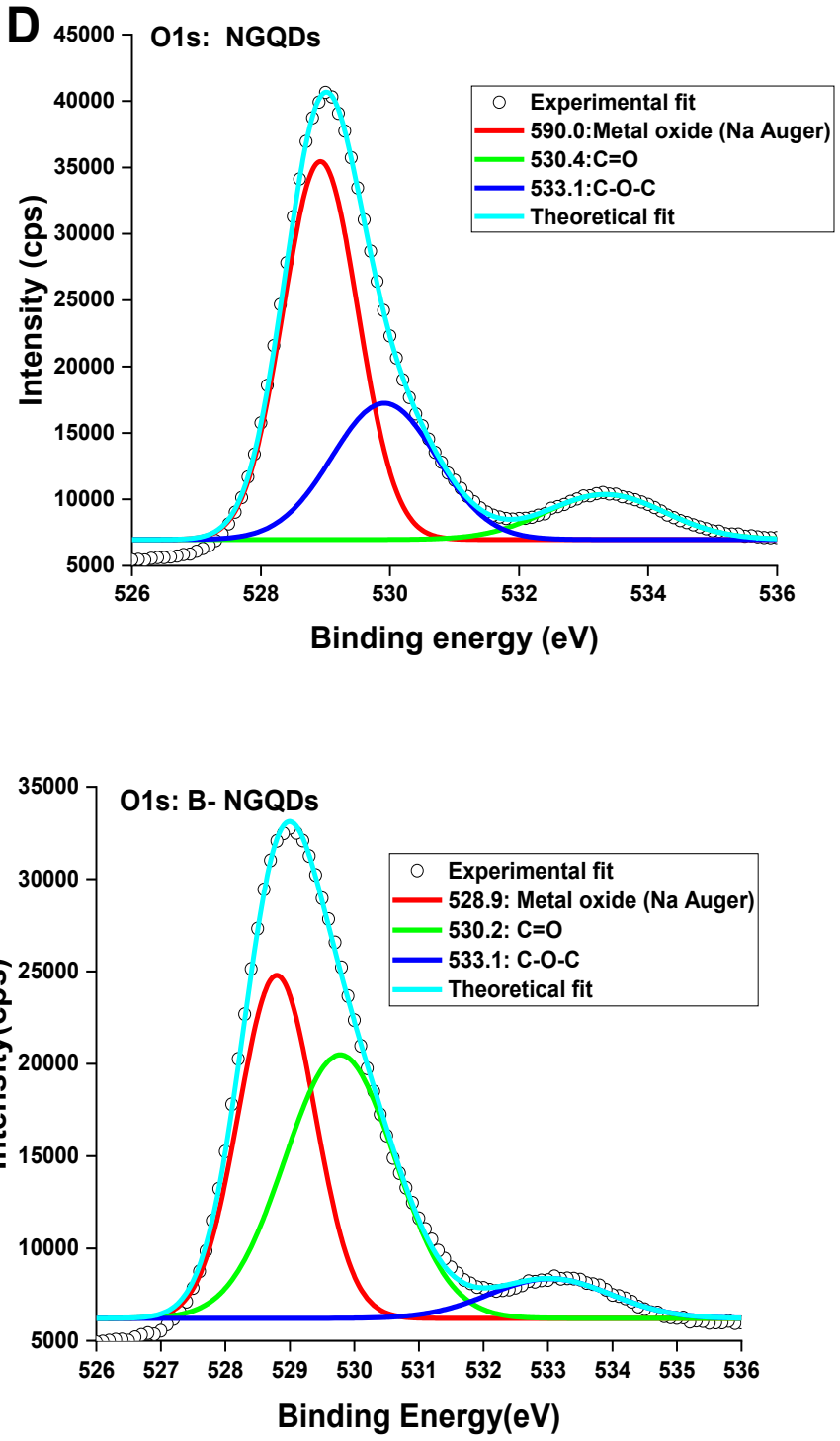

Fig. 4.7 XPS Wide scans of (A) NGQDs, B-NGQDs. XPS high resolution spectra for NGQDs and B-NGQDs: (B) C1s, (C) N1s and (D) O1s.

4.3.6 X-ray diffraction analysis (XRD)

XRD was used for phase identification of NGQDs and their conjugates. NGQDs exhibited a broad diffraction at 2θ= 30° which is ascribed to Bragg's reflection of the carbon in the graphene layers **[93],** Fig. 4.8. The B-NGQDs exhibited a diffraction at 2θ=17°, thus the presence of biotin in NGQDs caused a shift. Complex **2** exhibited a broad peak at 2θ = 28° due to the amorphous nature of the porphyrin **[94]**. The conjugates (**2**-B-NGQDs) showed a peak at 2θ =19° which blue shifted again when compared to B-NGQDs peak with 2 units. Blue shifts in the XRD patterns of graphene materials have been associated with the formation of new material **[95].** FA-NGQDs was also blue shifted when compared to NGQDs alone, and the peak was also less broad.

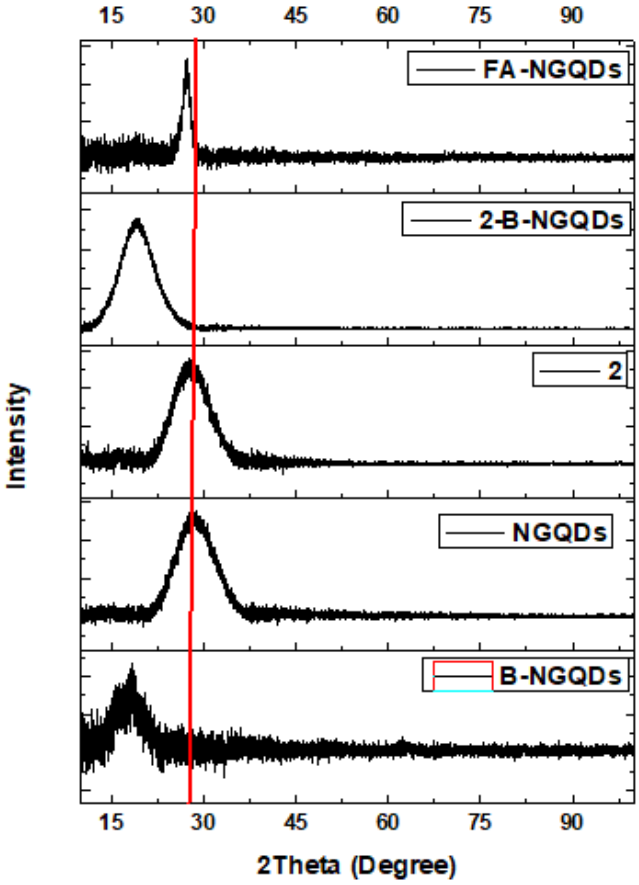

Fig 4.8. XRD analysis for the NGQDs and its conjugates

4.3.7 Fourier -transform infrared spectroscopy (FT-IR)

FTIR was used to analyse change in functional groups of the compounds, Fig 4.9**.** The covalent linking of biotin and NGQDs (to form B-NGQDs) was confirmed by the presence of the amide vibration at 1645 cm^{-1} and an OH from the NGQDs at 3319 cm^{-1}, Fig 4.9. The successful covalent linking of folic acid to NGQDs was confirmed by an amide bond at 1657 cm^{-1} with a less intense peak, (Fig 4.9). The spectra of NGQDs alone showed OH peak at 3308 cm^{-1} and C-N at 1558 cm^{-1}, but upon covalently linkage with FA the OH became more intense and amide bond was observed. Upon covalent conjugation of B-NGQDs to complex **2** (Fig 4.9), there is a shift of NH strech (for B-NGQDs at 1645 cm^{-1}) to 1656 cm^{-1} and there is a presence of C=O peak at 1472 which confirms succesful conjugation of complex **2** and B-NGQDs through the ester bond. The vibrational peak shifts suggesting presence of molecular interactions **[96].**

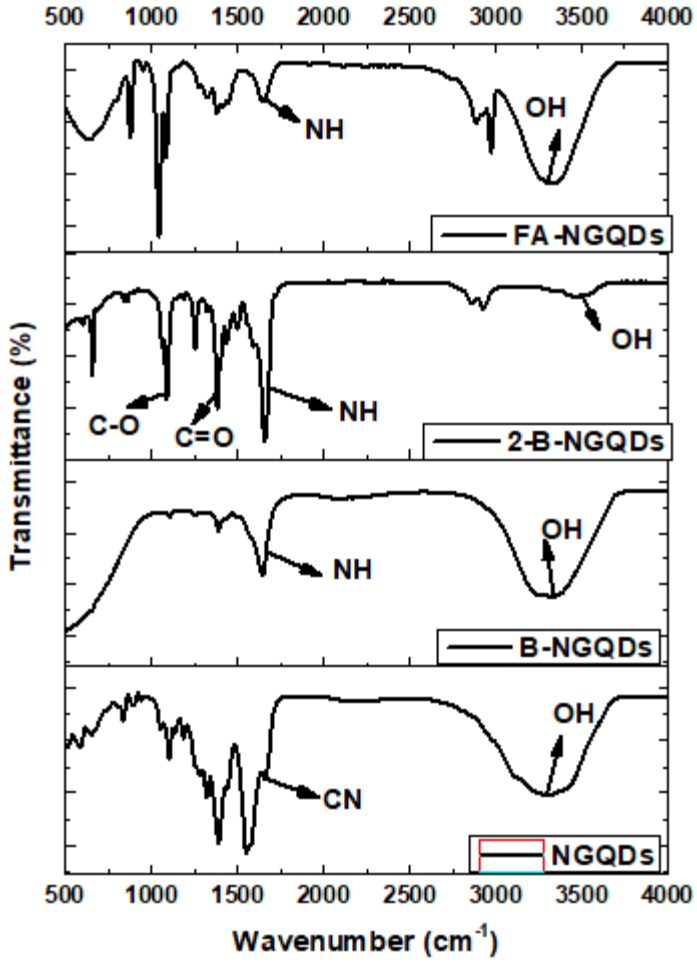

Fig 4.9. FT-IR spectra of NGQDs and their conjugates

4.3.8 Raman spectroscopy

Raman spectroscopy was used to determine the degree of structural defects introduced on the surface of the NGQDs upon conjugation to biotin or folic acid and porphyrin complexes. The G-band is a representation of in-plane vibration of sp^2 bonded carbon atoms, and D band is due to out of plane vibration sp^3 attributed to the presence of structural defects **[97]**. The disorder (D, sp^3) defects and graphitic (G, sp^2) bands were observed respectively at (1374;1570 cm^{-1}) for NGQDs, (1286;1574 cm^{-1}) for B-NGQDs, (1291; 1602 cm^{-1}) for **2**-B-NGQDs, (1046,1423 cm^{-1}) for FA-NGQDs, (1045, 1421 cm^{-1}) for **3**-FA-NGQDs and (1043,1420 cm^{-1}) for **3Q**-FA-NGQDs, (1053, 1420 cm^{-1}) for **5Q** -B-NGQDs, (1043, 1419 cm^{-1}) for **5**-B-NGQDs, (1050, 1422 cm^{-1}) for **3Q**-B-NGQDs, and (1018, 1419 cm^{-1}) for **3**-B-NGQDs. The shifts in the D and G band are an indication of strong interaction between porphyrins and graphitic sheets due to a charge transfer **[98]**, and Raman shifts have been attributed to factors such as nature, diameter and strain of nanoparticles **[99-102]**. The ratio intensity of the D and G bands (I_D/I_G) values obtained for NGQDs was 0.86, for B-NGQDs it increased to 0.93 and it increased drastically upon the conjugation of B-NGQDs to form (**2**-B-NGQDs) to 2.57. The I_D/I_G ratio (Table 4.2) of FA-NGQDs, **3**-FA-NGQDs and **3Q**-FA-NGQDs were 0.73, 0.85, and 0.51 respectively, and the ratio for FA-NGQDs is surprisingly lower than for NGQDs. The decrease could be due to the additional sp^2 carbons from folic acid in FA-NGQDs compared to NGQDs. It was also not expected for **3**-FA-NGQDs to result in higher I_D/I_G ratio compared to FA-NGQDs, since it is generally expected that $\pi - \pi$ conjugation will not affect the NGQDs structure as much as covalent bonding. The I_D/I_G ratio of **5Q**-B-NGQDs, **5**-B-NGQDs, **3Q**-B-NGQDs, and **3**-B-NGQDs obtained were 0.22, 0.64, 0.36, and 0.33 respectively. Increases or decreases in I_D:I_G ratios of GQDs have been previously reported to be due to size-dependent edge-state variations of GQDs **[102].**

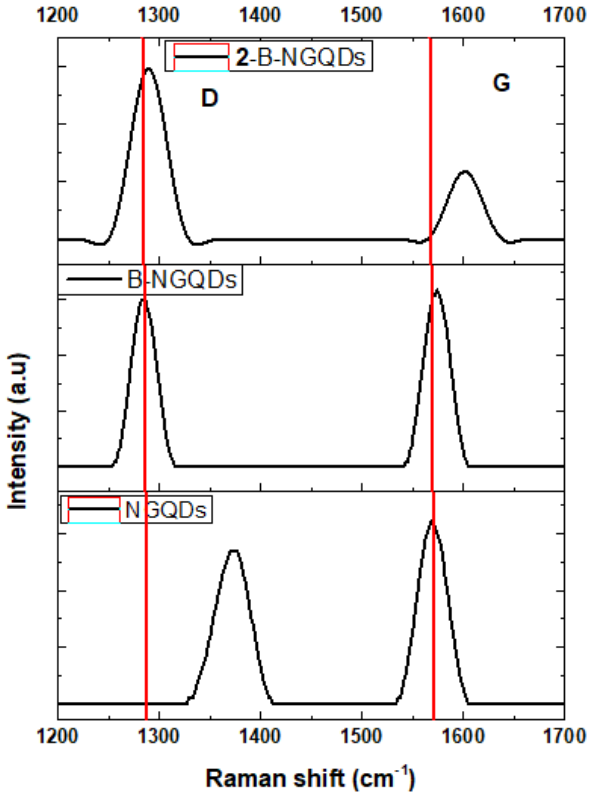

Fig 4.10. Raman spectra of NGQDs, B-NGQDs, and **2**-B-NGQDs as example.

4.4. Photophysical and photochemical parameters

All photophysical and photochemical parameters were studied in DMSO and results are presented in Table 4.3.

Table 4.3 Photophysical parameters in DMSO

Complex/ Conjugates	$\boldsymbol{\Phi_F}$	$\boldsymbol{\tau_F}$**(ns)**	$\boldsymbol{\Phi_\Delta}$	$\boldsymbol{\tau_T}(\boldsymbol{\mu s})$
NGQDs	0.70	5.02	-	-
B-NGQDs	0.10	2.27	-	-

FA-NGQDs	0.04	0.58	-	-
2	< 0.01	0.01	0.59	20
2-B-NGQDs	< 0.01	0.01	0.79	31
3	0.08	1.77	0.24	21
3-FA-NGQDs	0.06	1.39	0.97	117
3Q	0.03	1.28	0.56	83
3Q-FA-NGQDs	< 0.01	0.001	0.99	336
3-B-NGQDs	0.02	0.10	0.53	283
3Q-B-NGQDs	0.01	0.05	0.61	107
5	< 0.01	0.05	0.40	121
5-B-NGQDs	< 0.01	0.06	0.84	164
5Q	< 0.01	0.03	0.60	177
5Q-B-NGQDs	< 0.01	0.04	0.90	383

4.4.1 Fluorescence quantum yield (ϕ_F) and life-times (τ_F)

Fluorescence quantum yield (ϕ_F) were obtained using ZnTPP as a standard (ϕ_F^{std}=0.030) as a standard **[30]** in DMSO for porphyrins complexes, following the comparative methods reported in literature **[29]**. Quinine sulfate in 0.05M in H_2SO_4 solution (ϕ_F =0.52) **[103]**, as the NGQDs standard. It was observed that symmetric porphyrins **3** and **3Q** had higher ϕ_F when compared to asymmetric complexes **5** and **5Q**, and these low yields can be accounted by the presence of bromide which favors the intersystem crossing rather than fluorescence **[104]**. Complex **2** had lower ϕ_F when compared to complex **3** and **3Q** this is due to the fact that tin in **2** is a heavier metal when compared to zinc which influences the intersystem crossing. NGQDs had ϕ_F of 0.70 but upon decorating with biotin and folic acid ϕ_F values were 0.01 and

0.04, respectively (with the emission spectra shown (Fig 4.11 (A)). This suggests that the biomolecules folic acid and biotin quench fluorescence of NGQDs, the conjugates also resulted in lower yields compared to porphyrins. The fluorescence life-times (τ_F) of complexes and conjugates were studied using TCSPC analysis by excitation at emission maxima. The fluorescence life-time values followed the same trend as the fluorescence quantum yields, since τ_F are directly proportional to ϕ_F. Fig 4.11 (B) shows the fluorescence lifetime decay curve fitting for FA-NGQDs in DMSO as an example.

A

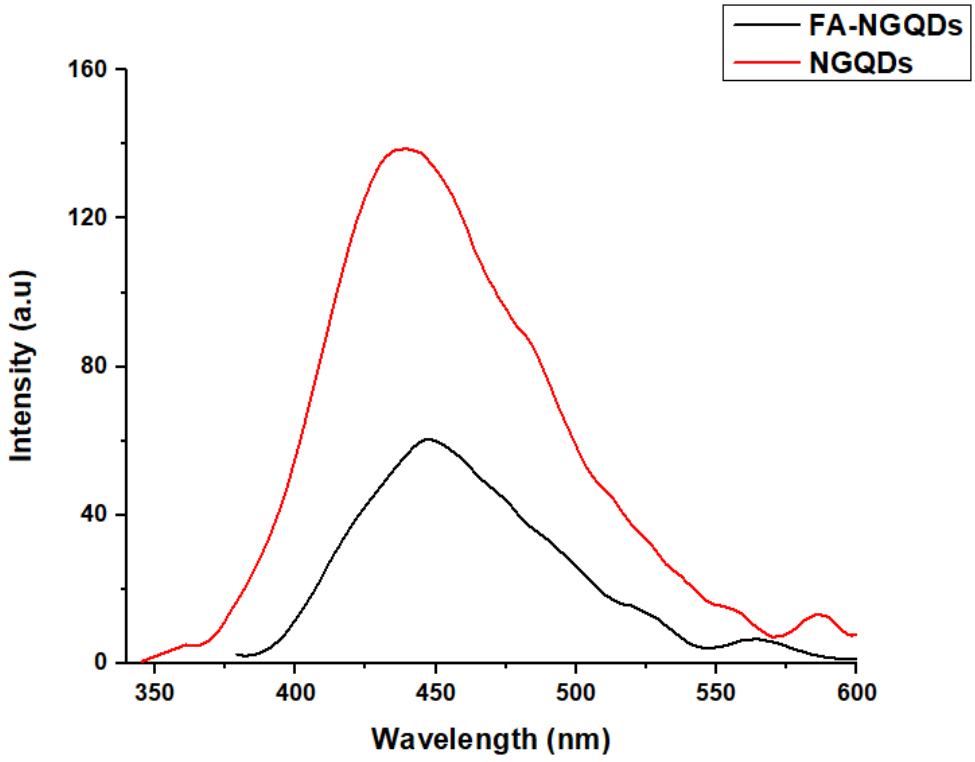

B

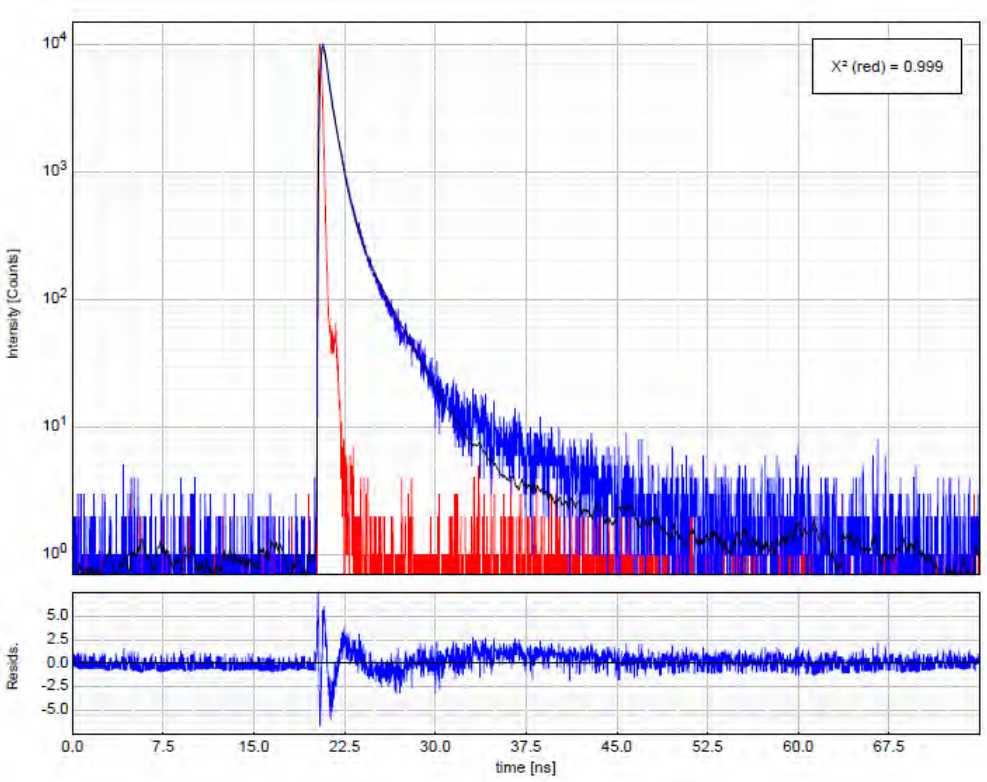

Fig 4.11. Emission spectra of FA-NGQDs (A), and fluorescence lifetime decay curve fitting (B) for FA-NGQDs in DMSO, using LUDOX HS-40 colloidal silica as a scatter sample.

4.4.2. Singlet oxygen quantum yields and triplet lifetimes

Singlet oxygen is generated through an energy transfer between the excited triplet state of photosensitizer and ground state in molecular oxygen **[4]**. In this study, the ϕ_Δ value were determined by monitoring chemical degradation of DMA as a singlet oxygen quencher and ZnTPP (ϕ_Δ^{std} =0.53) as a standard in DMSO **[33]**. The degradation of DMA was observed, (Fig. 4.12) and the values of ϕ_Δ were calculated using the equation reported in literature **[32]**. The Soret and Q bands of the porphyrin complexes remained stable confirming their photostability. The conjugates **2**-B-NGQDs (ϕ_Δ = 0.79), **3**-B-NGQDs (ϕ_Δ = 0.53), **3Q**-B-NGQDs (ϕ_Δ= 0.61), **5**-B-NGQDs (ϕ_Δ= 0.84), and **5Q**-B-NGQDs (ϕ_Δ = 0.90) resulted in higher ϕ_Δ when compared to their respective porphyrin complexes only, and this is due to the presence of heavy atom sulfur from biotin which enhances the intersystem crossing to the triplet state. Dyes with sulfur are reported to have internal heavy atom effect **[105]**, and they show larger increase in the rate of intersystem crossing which leads to higher oxygen yield **[106]**. It was

also observed that FA-NGQDs porphyrin conjugates **3**-FA-NGQDs (ϕ_Δ = 0.97) and **3Q**-FA-NGQDs (ϕ_Δ = 0.99) had higher ϕ_Δ when compared to their porphyrin complexes only (Table 4.3), thus FA improves singlet oxygen quantum yields of porphyrins as has been observed before **[107]**. It was also observed that **3**-FA-NGQDs and **3Q**-FA-NGQDs had larger ϕ_Δ when compared to **3**-B-NGQDs and **3Q**-B-NGQDs, as it is reported that the introduction of folic acid changes the photophysical properties which also result in an increase in ϕ_Δ **[107]**.

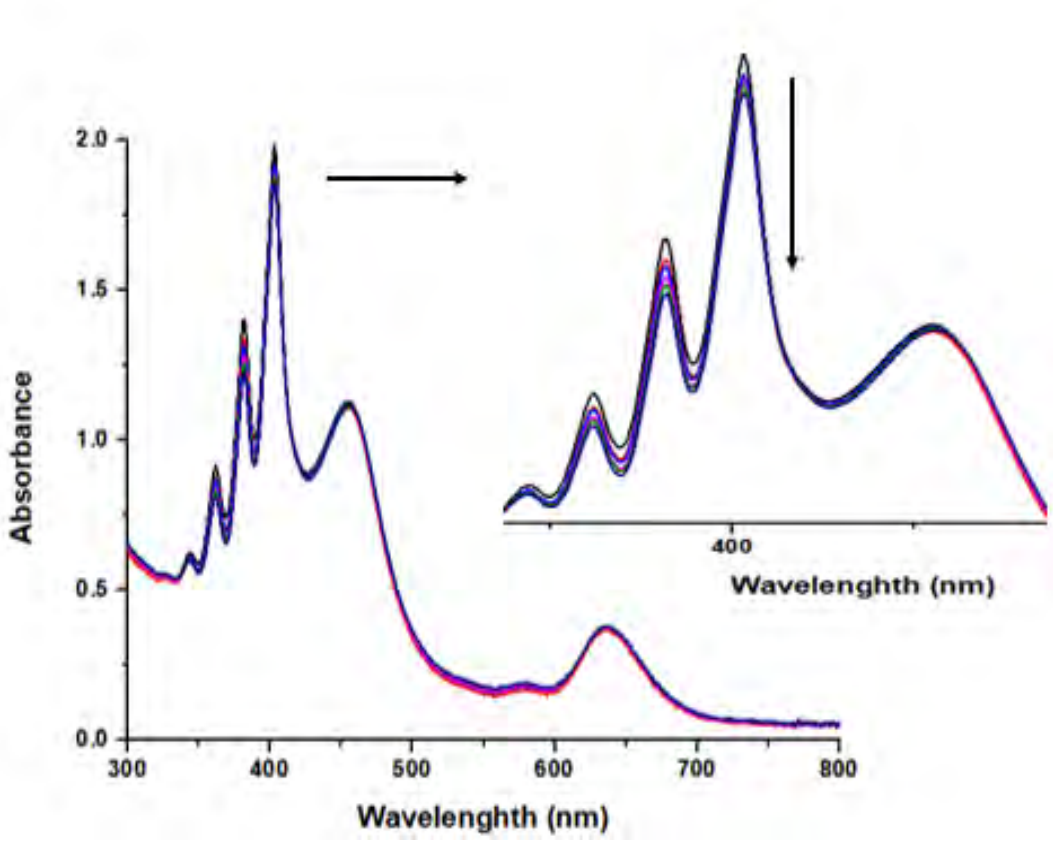

Fig 4.12. Degradation of 9,10-dimethylanthracene (DMA) in the presence of complex **2** using DMSO as a solvent as an example**.**

The triplet decay curves (Fig 4.13) were fitted exponentially on ORIGIN® 8 Professional software to obtain the triplet lifetimes. The triplet lifetime (τ_T) for **3Q**-FA-NGQDs is longer than for **3Q** alone, the same applies for complex **3** and its conjugate. Thus the FA-NGQDs improves the triplet lifetime for porphyrins, hence the improved singlet oxygen quantum yield of porphyrins in the presence of FA-NGQDs, since singlet oxygen is generated from the triplet state. It was also observed that B-NGQDs improved the triplet lifetimes of the porphyrin

complexes since upon conjugation high τ_T values were obtained, (Table 4.3). The triplet decay curve (for complex **5** as an example) is shown in Fig 4.13.

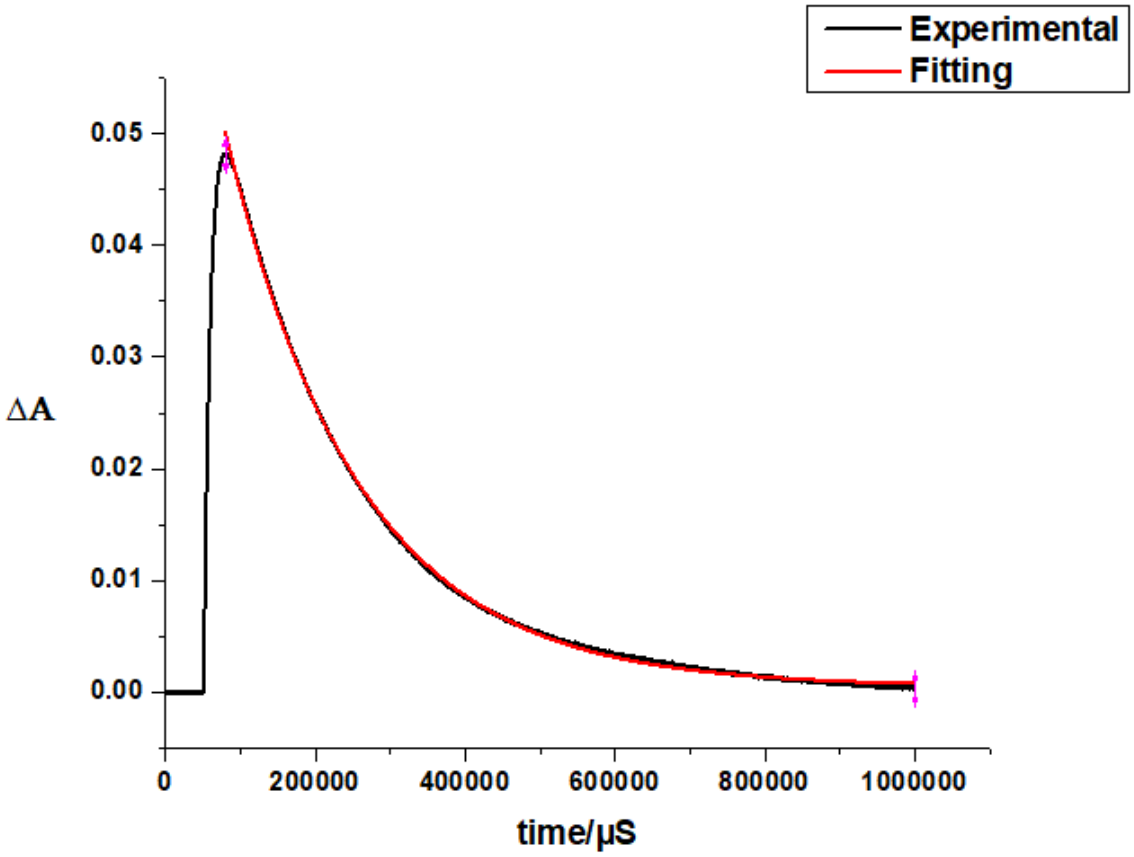

Fig 4.13 Triplet decay curve of **5** as an example in DMSO.

4.4. Summary of the chapter

Symmetric (**2, 3,** and **3Q**) and asymmetric (**5** and **5Q**) substituted porphyrins were synthesized as potential photosensitisers for PDT. NGQDs were also synthesized and decorated with different biomolecules; biotin and folic acid and conjugated to the porphyrin complexes. The conjugates and porphyrin complexes were fully characterized by different characterizing techniques. The conjugation of **2**-B-NGQDs was done through an axial ligand forming an ester bond, and all other conjugation was through π-π stacking. The photophysiochemical

properties of compounds were studied, and it was observed that the ϕ_F of porphyrins decreased upon conjugation to NGQDs complexes along with τ_F. However, upon conjugation of porphyrin complexes to B-NGQDs,FA-NGQDs there was an increase in ϕ_Δ.

Chapter 5

5.1 Cell studies

The MCF-7 cells were grown to 100% confluency, and the stock concentration of all complexes was prepared by dissolving each complex in 1% DMSO and making the volume up with supplemented media. DMSO (1%) used had a negligible effect on the cells (Appendix A15).

5.1.1 *In vitro dark cytotoxicity*

The MCF-7 cells were treated with porphyrin complexes and their conjugates at concentrations ranging from 2.5 µg/mL to 40 µg/mL and incubated in dark for 24h. The percentage of live cells were calculated relative to untreated cell samples that is at 0 µg/mL concentration of complex/ conjugates using WST-1 cell proliferation assay. At all concentrations the cell viability of all complexes and conjugates were above 90% which is negligible and not harmful. *In vitro dark cytotoxicity* is undesirable for photosensitizers aimed for use in PDT **[5]**, Fig 5.1.

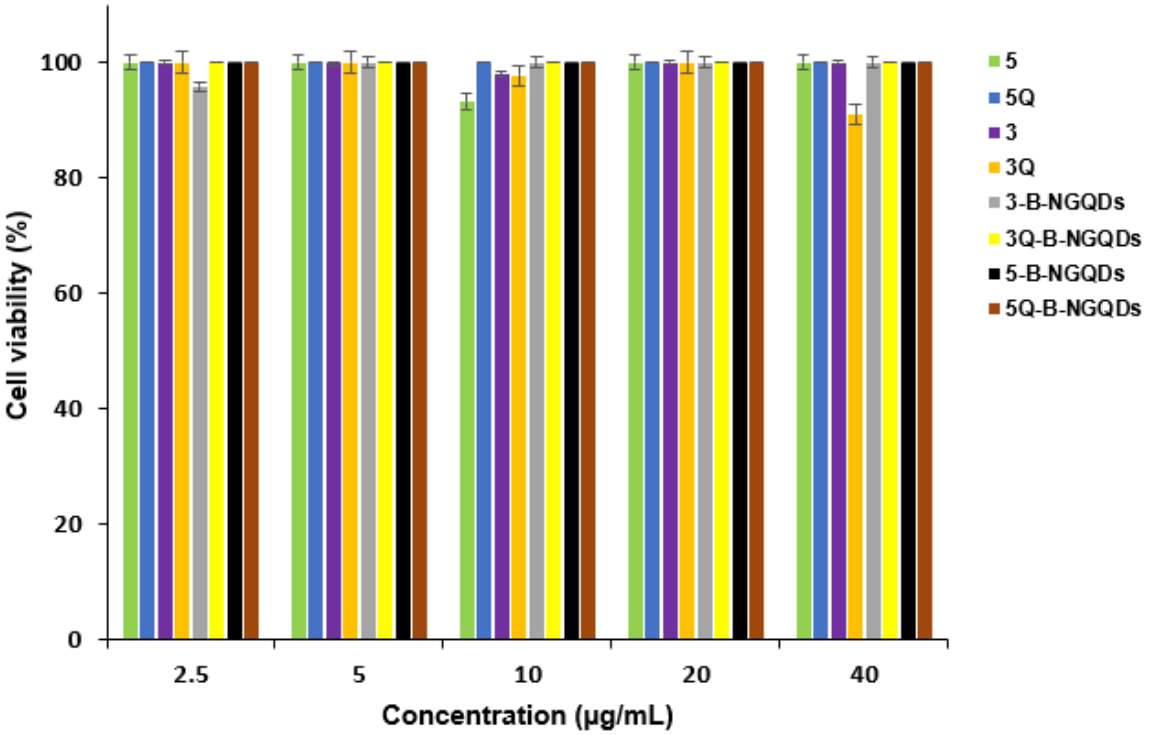

Fig 5.1. Histograms showing the MCF-7 cells cell viability (%) when incubated in the dark in the presence of complexes **3, 3Q, 5, 5Q**, and their conjugates.

5.1.2 Photodynamic therapy

The MCF-7 cells were treated with same range of concentrations as used for dark cytotoxicity studies. The cells were then incubated for 24h, they were then irradiated with Thorlabs M625 LED (625 nm) for 30 min. Upon irradiation, the phototoxicity of all photosensitizer against MCF-7 cells increased with an increase in concentrations. It was observed that the symmetric porphyrins (**3** and **3Q**) performed poorly when compared to asymmetric porphyrins (**5** and **5Q**), and this is due to the high singlet oxygen quantum yields of asymmetric porphyrins (Fig 5.2 (A)). Charged porphyrins **5Q** and **3Q** had better performance when compared to their respective uncharged porphyrins **5** and **3**, and this is due to that positively charged porphyrins can penetrate the tumor cells membranes easily giving better PDT results **[61]**. At the highest concentration of 40 µg/mL, conjugates **5**-B-NGQDs and **5Q**-B-NGQDs were the best performing with cell viability of 17% and 14%, respectively (Table 5.1). Also, at a highest concentration of 40 µg/mL complex **2** had a cell viability of 31% and complex **3** had cell viability of 45% (Table 5.1) and this is due to high singlet oxygen quantum yield of **2** (Fig 5.2 (B)) when compared to **3**, and singlet oxygen is the main cytotoxic species in PDT. **3Q**-FA-NGQDs exhibited higher PDT effect with cell viability of 28% at 40 µg/mL compared to **3Q** alone which exhibited cell viability of 37%, this suggest that the FA-NGQDs enhanced the PDT effect of complex **3Q**. The same trend was observed with **3**-FA-NGQDs when is compared to **3** alone, **3**-FA-NGQDs exhibited cell viability 31% and complex **3** exhibited cell viability of 45% also suggesting that FA-NGQDs improved the PDT effect of complex **3** (Fig 5.2 (C), Table 5.1). Conjugates performed better as expected because the biomolecules (biotin and folic acid) on the NGQDs have high selectivity, and nanoparticles are reported to enhance the delivery of the photosensitizer dye and selective accumulation in cancer tumors due to enhanced solubility in aqueous solvents and the enhanced permeability and retention effect **[108]**. It was also observed that **3**-FA-NGQDs and **3Q**-FA-NGQDs had better PDT activity with cell viability of (31% and 28%), respectively when compared to **3**-B-NGQDs (33%) and **3Q**-B-NGQDs (37%), and this concludes that FA enhanced PDT activity better than biotin. The IC_{50} values (Table 5.1) were used to determine the concentration that is required for the conjugates/ complexes to eradicate 50% of the cells and were determined as shown in Fig. 5.3. Lower IC_{50} value is favourable as it entails the need for low concentration of a sensitizer for therapy to yield effective cell inhibition **[109]. 5Q**-B-NGQDs had a lowest IC_{50} value of 1.4

μg/mL. All the conjugates had the lowest IC_{50} values when compared to their complexes alone.

A

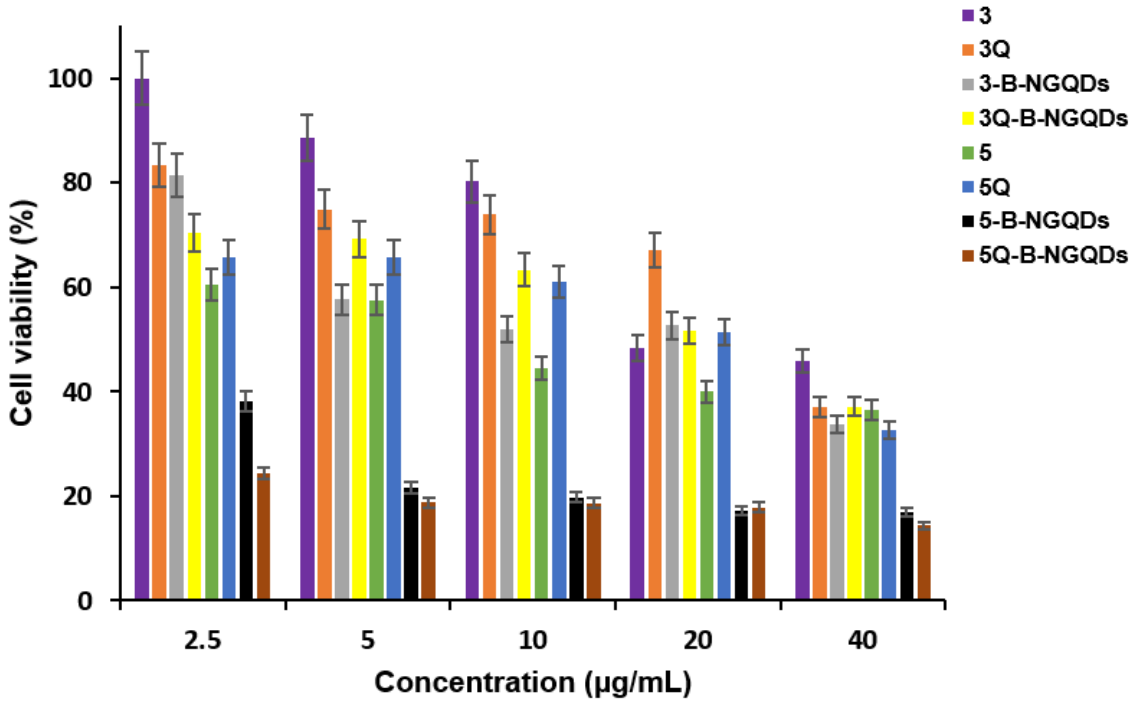

B

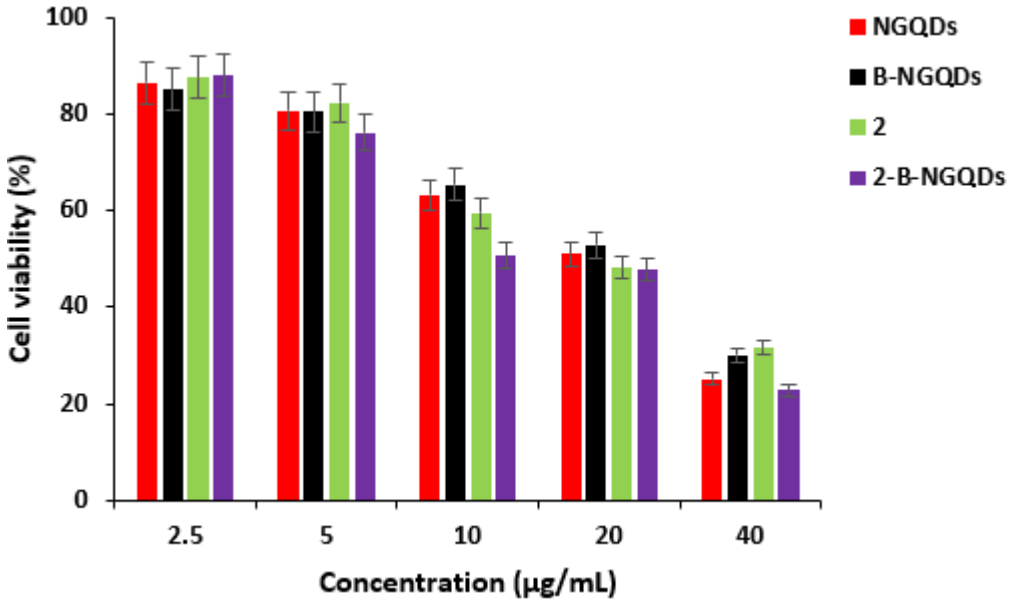

C

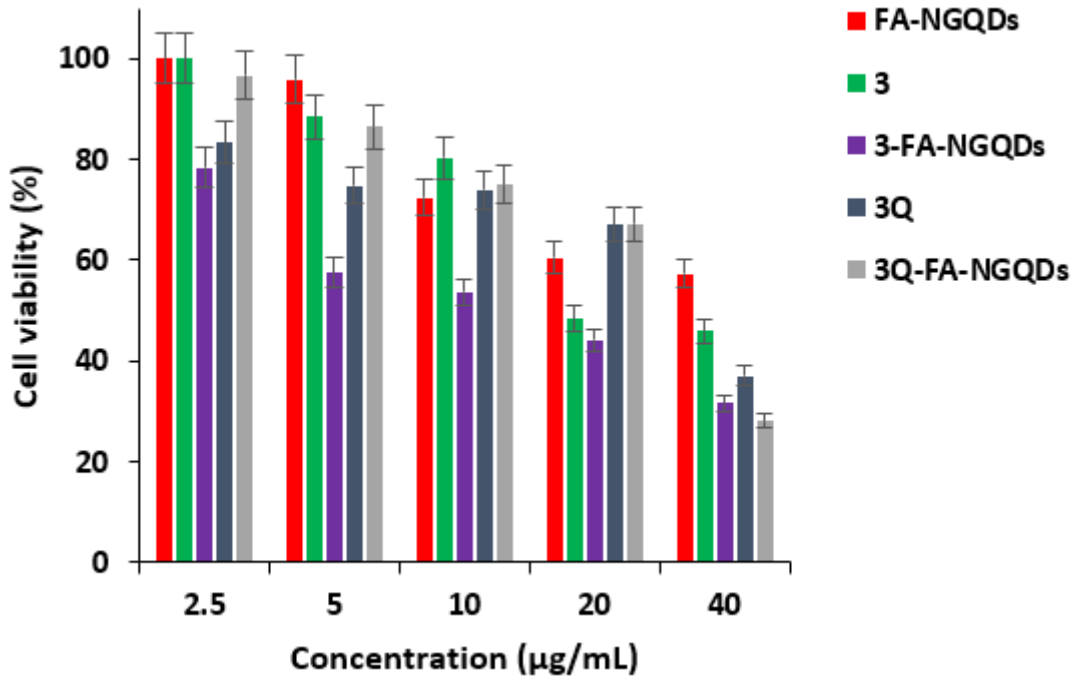

Fig 5.2. Histograms showing PDT activity of (A) complex **3**, **5**, **3Q**, **5Q**, and their B-NGQDs conjugates. (B) **2** and its conjugates, and (C) **3**, **3Q** and their FA-NGQDs conjugates.

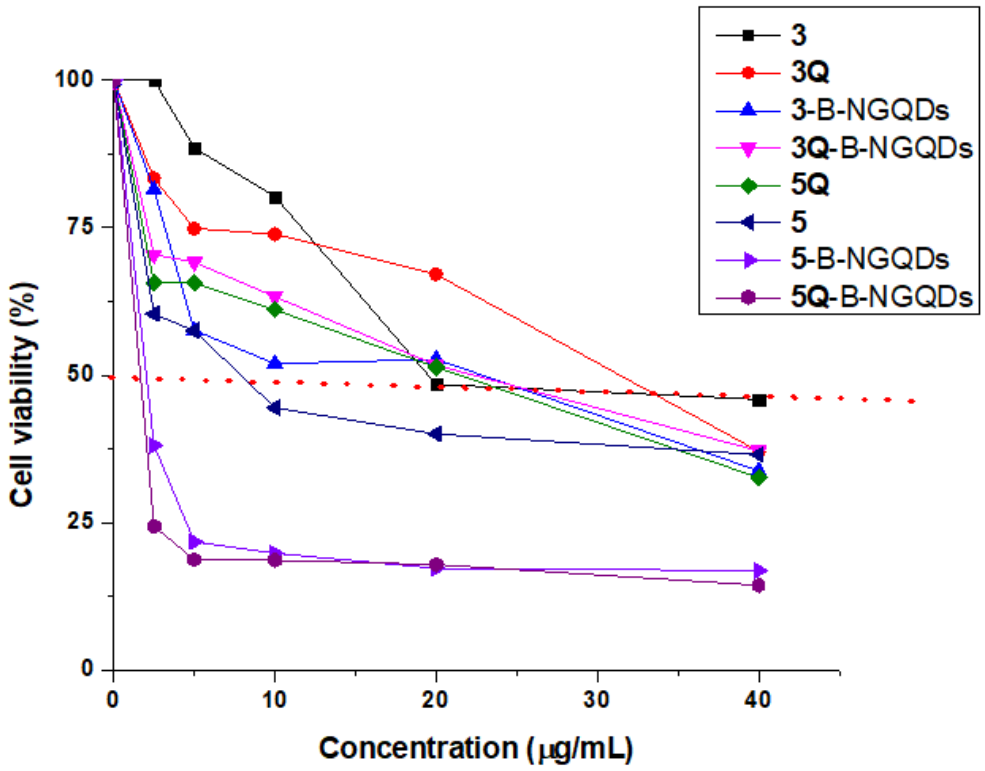

Fig 5.3 Cytotoxic plot was used to calculate IC_{50} values, using complexes **3, 5** and their conjugates as an example.

Table 5.1: IC_{50} values of complexes and conjugates

Complex/ Conjugate	**IC_{50} value (**μg/mL)	**Cell viability (%) at 40μg/mL**	**Cellular uptake(absorbance) at 40μg/mL**
NGQDs	14.2	25	0.42
B-NGQDs	14.4	30	0.45
2	11.2	31	0.43
2-B-NGQDs	10.4	22	0.48
3	14.5	45	0.23
3Q	5.8	37	0.26
3-B-NGQDs	4.4	34	0.28
3Q-B-NGQDs	3.2	37	0.31
5	10.7	36	0.85
5Q	7.5	33	0.91
5-B-NGQDs	4.4	17	0.89
5Q-B-NGQDs	1.4	14	0.96
FA-NGQDs	8.2	57	0.39
3-FA-NGQDs	5.87	31	0.38
3Q-FA-NGQDs	3.9	28	0.49

The change in cellular morphology of the MCF-7 breast cells before and after treatment were obtained from the microscope, Fig 5.4. Healthy MCF-7 cells have an eye-like shape and are surface adherent as shown in Fig 5.4. However, upon PDT treatment the overall size reduces, forming circular shapes as observed below and the cells ultimately die **[109]**.

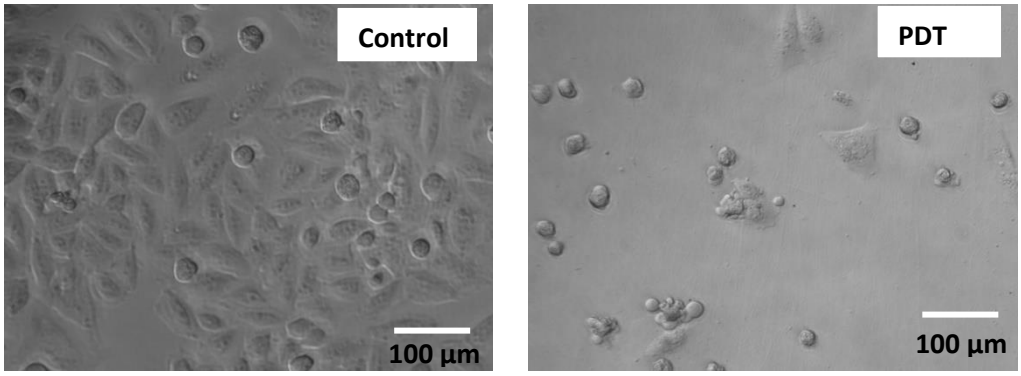

Fig 5.4. The cytograms on MCF-7 cells for control (1% DMSO), and after being treated with **5Q**-B-NGQDs in presence of light.

5.1.3 Cellular uptake

The cellular uptake of all complexes and conjugates was determined by measuring absorbance of internalized photosensitizer drug after incubating with MCF-7 cells for 24h. The cellular uptake plays an important role in the PDT activity of the photosensitizer **[110]**. Fig. 5.5 (A) shows that B-NGQDs has better cellular uptake (especially at low concentrations) compared to NGQDs, and this due to the fact that cancer cells are known to overexpress biotin receptors **[111].** The asymmetric complexes (**5** and **5Q**) were compared with symmetric complexes (**3** and **3Q**) in Fig. 5.5 (B), and it was observed that at lower concentrations (and in the absence of B-NGQDs), the symmetric complexes have higher uptake, but at a higher concentration the asymmetric have higher uptake. In the presence of B-NGQDs, there was a higher increase in the uptake for the asymmetrical porphyrins (Fig 5.5 (C)). At a highest concentration of 40 µg/ mL, the uptake absorbance intensity of the compounds and their conjugates are listed in Table 5.1. Conjugates of B-NGQDs had better uptake when compared to the porphyrin complexes alone and this is due to the high selectivity from B-NGQDs, and tumor targeting properties of biotin **[110]**. At higher concentrations, **3**-FA-NGQDs had higher cellular uptake compared to **3** alone as shown in Table 5.1, Fig 5.5 (D). The same applies to **3Q**-FA-NGQDs compared to **3Q**. Therefore, it can be concluded that FA-NGQDs improved the uptake efficacy of **3** and **3Q** due to the tumor targeting properties of folic acid **[50]**. **3Q**-FA-NGQDs had the highest cellular uptake at highest concentrations, and this is attributed by cationic charges and high selectivity from FA-NGQDs which makes it to easily penetrate the

cancer cells. At a highest concertation of 40 µg/ mL **3**-FA-NGQDs (0.38) and **3Q**-FA-NGQDs (0.49) had higher cellular uptake when compared to **3**-B-NGQDs (0.28) and **3Q**-B-NGQDs (0.31) and this confirms that FA is better at targeting.

A

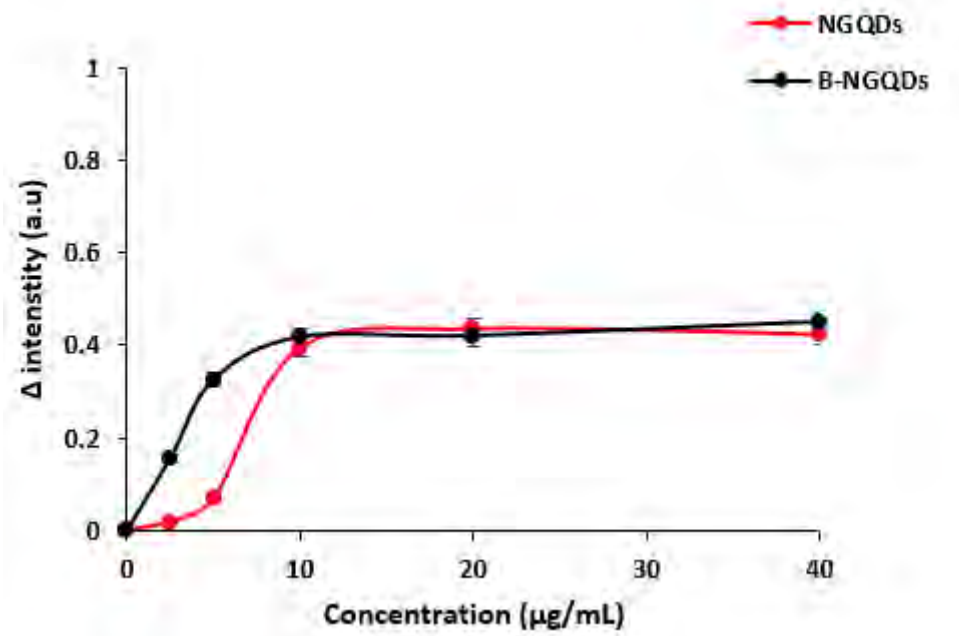

B

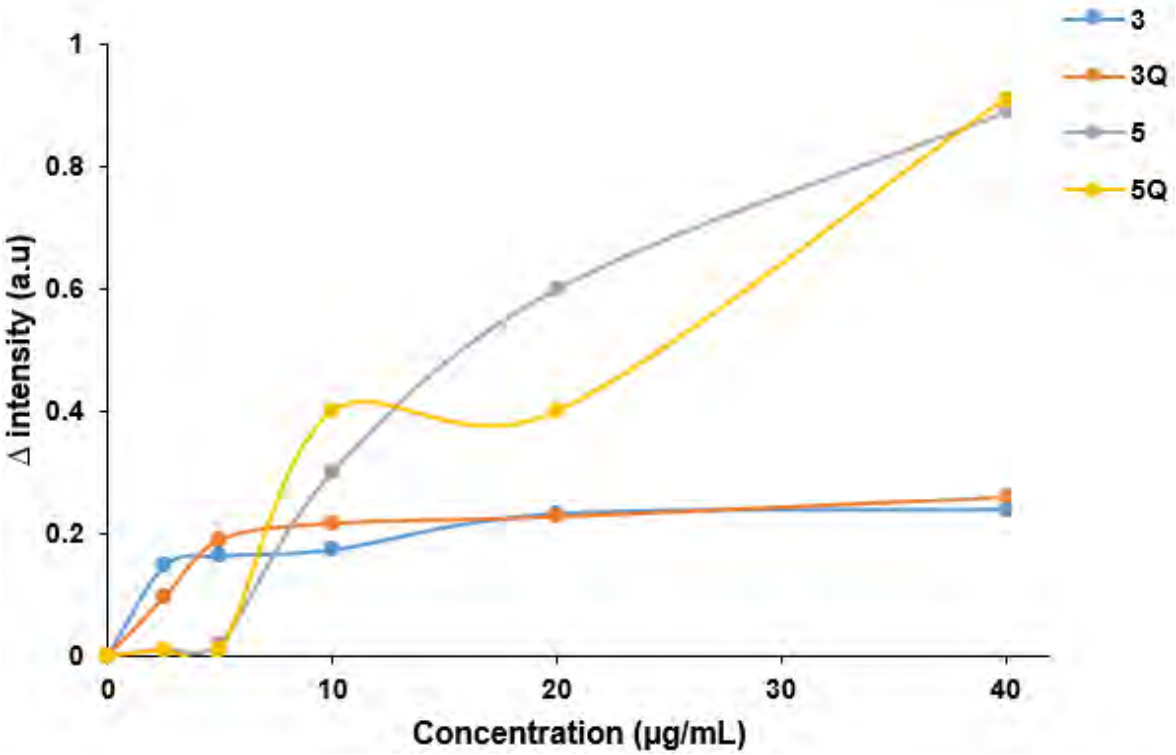

C

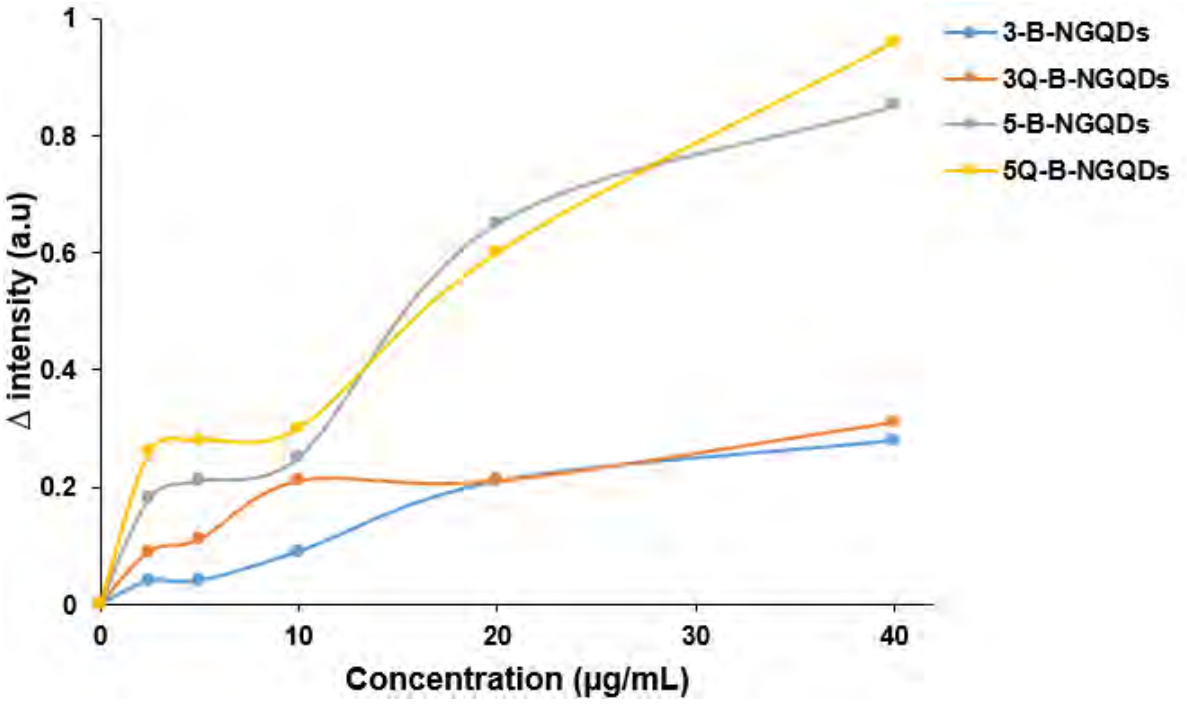

D

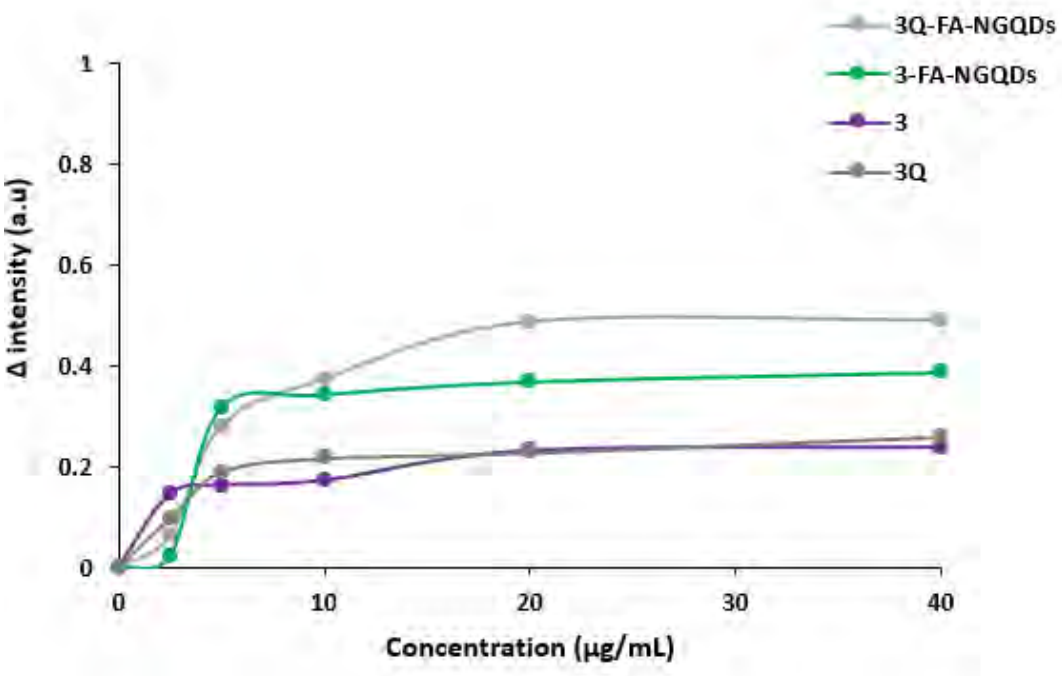

Fig 5.5 MCF-7 cellular uptake over 24h at different concentration for (A) NGQDs and B-NGQDs, (B) **3**, **3Q**, **5**, and **5Q**, (C) **3**, **5**, and their B-NGQDs conjugates, and (D) **3** and their FA-NGQDs conjugates.

5.3 Summary of the chapter

It was observed that all complexes and conjugates had no dark toxicity. B-NGQDs and FA-NGQDs enhanced the PDT effect of the porphyrin complexes, as it was observed that upon conjugation there was an increase in PDT activity (low number of viable cells). Biotin and folic acid enhanced the cellular uptake of NGQDs when attached to them. Upon quaternization, it was observed that **3Q** and **5Q** had an increase in cellular uptake when compared to their respective complexes **3** and **5**.

Chapter 6

6.1 General conclusion

This thesis reports for the first time asymmetrical and symmetrical morpholine substituted porphyrins conjugated to B-NGQDs and FA-NGQDs, through either covalent or non-covalent attachment for PDT. The porphyrins were quaternized to improve their water solubility. NGQDs exhibited high ϕ_F but it decreased upon conjugation with biotin, and it was due to the presence of a heavy atom sulfur. Complexes **2** and **3** had the same substituents but different central metals however, the singlet oxygen quantum yield for **2** was (ϕ_Δ = 0.59) and (ϕ_Δ = 0.24) for **3.** This is due to that Sn in **2** is heavier metal than Zn in **3**. Asymmetric porphyrins (**5**) exhibited higher singlet oxygen quantum yield when compared to the symmetric porphyrins (**3**), and this because asymmetry and bromine enhances intersystem crossing. These higher singlet oxygen quantum yields corresponded to high PDT activity against MCF-7 cells. The conjugates resulted in enhanced PDT activity and cellular uptake when compared to the porphyrin complexes alone. It was also observed that the cationic porphyrins (**3Q** and **5Q**) had better cellular uptake when compared to their respective neutral complexes, because cationic porphyrins penetrate the cell walls easily.

6.2 Future prospects

- Try other alternative methods to synthesize ABAB porphyrin (Fig 6.1) and expand on the study of asymmetry by comparing it with complex **3** and **5**

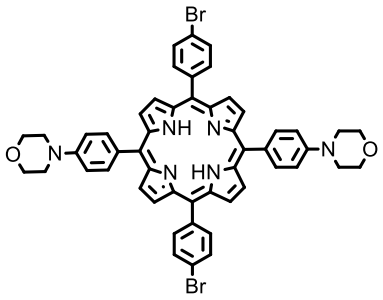

Fig 6.1. ABAB porphyrin structure

- Follow the method in **[112]** to calculate singlet oxygen quantum yield of NGQDs, since it was observed in the study that it enhances the singlet oxygen quantum yields of porphyrin complexes.

REFERENCES

[1] Chen, J., Fan, T., Xie, Z., Zeng, Q., Xue, P., Zheng, T., Chen, Y., Luo, X., Zhang, H. Advances in nanomaterials for photodynamic therapy applications: Status and challenges. Biomaterials, 237 (2020) 119827.

[2] Dolmans, D.E., Fukumura, D, Jain, R.K., 2003. Photodynamic therapy for cancer. Nat. Rev. Canc., 3 (2003) 380.

[3] Juarranz, Á., Jaén, P., Sanz-Rodríguez, F., Cuevas, J., González, S. Photodynamic therapy of cancer. Basic principles and applications. Clin. Transl. Oncol., 10 (2008) 148.

[4] Castano, A.P., Demidova, T.N., Hamblin, M.R. Mechanisms in photodynamic therapy: part one—photosensitizers, photochemistry and cellular localization. Photodiagnosis. Photodyn. Ther., 1 (2004) 279.

[5] Detty, M.R., Gibson, S.L. and Wagner, S.J. Current clinical and preclinical photosensitizers for use in photodynamic therapy. J. Med. Chem., 47 (2004) 3897.

[6] Norvaiša, K., Kielmann, M. and Senge, M.O. Porphyrins as colorimetric and photometric biosensors in modern bioanalytical systems. Chem. Bio. Chem., 21 (2020) 1793.

[7] Battersby, A.R. Tetrapyrroles: the pigments of life. Nat. Prod. Rep., 17 (2000) 507.

[8] Chen, Z., Lohr, A., Saha-Möller, C.R., Würthner, F. Self-assembled π-stacks of functional dyes in solution: structural and thermodynamic features. Chem. Soc. Rev., 38 (2009) 564.

[9] Lindsey, J.S. Synthesis of meso-substituted porphyrins. The porphyrin handbook. (2000). Kadish K.M, Smith, K.M., Guilard R. Academic press: San Diego, CA, USA. 45-118

[10] Wainwright, M. Photodynamic antimicrobial chemotherapy (PACT). J. Antimicrob. Chemother., 42 (1998) 13.

[11] Zucca, P., Neves, C.M., Simões, M.M., Neves, M.D.G.P., Cocco, G., Sanjust, E. Immobilized lignin peroxidase-like metalloporphyrins as reusable catalysts in oxidative bleaching of industrial dyes. Molecules, 21 (2016) 964.

[12] Du, Y., Zhang, S., Jiang, X., Zhu, K., Geng, Z., Fang, Y., Huo, P., Liu, C., Song, Y. Wang, G. Synthesis and Optical Properties of Poly (aryl ether ketone) s Incorporating Porphyrins in the Backbones. J. Polym. Sci., Part A: Polym. Chem., 52 (2014) 1282.

[13] Rothemund, P. Formation of porphyrins from pyrrole and aldehydes. J. Am. Chem. Soc.,57 (1935) 2010.

[14] Rothemund, P. A new porphyrin synthesis. The synthesis of porphin1. J. Am. Chem. Soc.,58 (1936) 625.

[15] Adler, A.D., Longo, F.R. and Shergalis, W. Mechanistic investigations of porphyrin syntheses. I. Preliminary studies on ms-tetraphenylporphin. J. Am. Chem. Soc., 86 (1964) 3145.

[16] Adler A.D., Longo F.R., Finarelli J.D., Goldmach J., Assour J., Korsakof L. A simplified synthesis for Meso-Tetraphenylporphine. J. Org. Chem., 32(1967)476.

[17] Vicente, M.G.H. Smith, K.M. Porphyrins and Derivatives Synthetic Strategies and Reactivity Profiles. Curr. Org. Chem., 4 (2000) 139.

[18] Lindsey J.S., Schreiman I.C., Hsu H.C., Kearney P.C., Margueretta A.M. Rothemund, Adler-Longo Reactions Revisited: Synthesis of Tetraphenylporphyrins under Equilibrium Conditions. J. Org. Chem., 52 (1987) 827.

[19] Lindsey, J.S. Synthetic routes to meso-patterned porphyrins. Acc. Chem. Res., 43 (2010) 300.

[20] Faugeras P., Vergnaud J., Lucas R., Boe B., Teste K., Zerrouki R., Iodine-catalyzed one-pot synthesis of unsymmetrical meso-substituted porphyrins. Tetrahedron, 66 (2010) 1994.

[21] Nascimento, B.F., Pineiro, M., Rocha Gonsalves, A.M.D.A., Ramos Silva, M., Matos Beja, A. and Paixão, J.A. Microwave-assisted synthesis of porphyrins and metalloporphyrins: a rapid and efficient synthetic method. J. Porphyr. Phthalocyanines, 11 (2007) 77.

[22] Kappe C.O., Stadler A., Dalinger D. In Microwaves in Organic and Medicinal Chemistry. R. Mannhold R., Kubinyi H., Folkers G. John Wiley & Sons, Germany, 52 (2012).

[23] Feng X., Senge M.O., An efficient synthesis of highly functionalized asymmetric porphyrins with organolithium reagents, J. Chem. Soc., Perkin Trans., 1 (2001) 1030.

[24] Milanesio E., Chiacchiera S.M., Silber J.J., Durantini E.N., Synthesis of Asymmetrical Porphyrins Substituted in the meso-position from Dipyrrolomethanes, Molecules, 5 (2000) 531.

[25] Lu, H., Kobayashi, N. Optically active porphyrin and phthalocyanine systems. Chem. Rev., 116 (2016) 6184.

[26] Weiss, C., Kobayashi, H., Gouterman, M. Spectra of porphyrins: Part III. Self-consistent molecular orbital calculations of porphyrin and related ring systems. J. Mol. Spectrosc., 16 (1965) 415.

[27] Matarazzo, A., Hudson, R.H. Fluorescent adenosine analogs: a comprehensive survey. Tetrahedron, 11 (2015) 1627.

[28] Hell, S.W. and Kroug, M. Ground-state-depletion fluorscence microscopy: A concept for breaking the diffraction resolution limit. Appl. Phys. B., 60 (1995) 495.

[29] Fery-Forgues, S., Lavabre, D. Are fluorescence quantum yields so tricky to measure? A demonstration using familiar stationery products. J. Chem. Educ., 76 (1999) 1260.

[30] Taniguchi, M., Lindsey, J.S., Bocian, D.F. Holten, D. Comprehensive review of photophysical parameters (ε, Φf, τs) of tetraphenylporphyrin (H2TPP) and zinc tetraphenylporphyrin (ZnTPP)–Critical benchmark molecules in photochemistry and photosynthesis. J. Photochem. Photobiol. C: Photochem. Rev., 46 (2021) 100401.

[31] Lyubimtsev A., Semeikin A., Zheglova N., Sheinin V., Kulikova O., Syrbu S. Synthesis and photophysical properties of low symmetrical porphyrin-amino acid conjugates and their Zn complexes, Macroheterocycles, 11 (2018) 103.

[32] Nyokong T., Antunes E. The Handbook of Porphyrin Science. Kadish K.M., Smith R.M., Guilard R.M. World Scientific, Singapore, 7 (2010).

[33] Redmond R.W., Gamlin J.N. A compilation of singlet oxygen yields from biologically relevant molecules, Photochem. Photobiol., 70 (1999) 391.

[34] B. Babu, R.C. Soy, J. Mack, T. Nyokong. Non-aggregated lipophilic water-soluble tin porphyrins as photosensitizers for photodynamic therapy and photodynamic antimicrobial chemotherapy. New J. Chem., 44 (2020) 11006.

[35] Ohulchanskyy T.Y., Donnelly D.J., Detty M.R., Prasad P.N. Heteroatom substitution induced changes in excited-state photophysics and singlet oxygen generation in chalcogenoxanthylium dyes: Effect of sulfur and selenium substitutions. J. Phys. Chem. B., 108 (2004) 8668.

[36] Oliveira, A.S., Licsandru, D., Boscencu, R., Socoteanu, R., Nacea, V., Vieira Ferreira, L.F. A singlet oxygen photogeneration and luminescence study of unsymmetrically substituted mesoporphyrinic compounds. Intern. J. Photoenergy., 2009 (2009) 1.

[37] Zhou, Y., Sun, H., Wang, F., Ren, J., Qu, X., 2017. How functional groups influence the ROS generation and cytotoxicity of graphene quantum dots. Chem. Comm., 53 (2017) 10588.

[38] De Souza, T.G.B., Vivas M.G., Mendonca, C.R, Plunkett, S., Filatov, M.A., Senge, M.O., De Boni L.J. Studying intersystem crossing rate and triplet quantum yield of meso substituted porphyrins by means of pulse train fluorescence technique, J. Porphyr. Phthalocyanines, 20 (2016) 282.

[39] Li L., Wu G., Yang G., Peng J., Zhao J., Zhu J. Focusing on luminescent graphene quantum dots: current status and future perspectives, Nanoscale, 10 (2013) 4015.

[40] Zhu S., Song Y., Zhao X., Shao J., Zhang J., Yang B. The photoluminescence mechanism in carbon dots (graphene quantum dots, carbon nanodots, and polymer dots): current state and future perspective, Nano Res., 2 (2015) 355.

[41] Iannazzo D., Ziccarelli I., Pistone A. Graphene quantum dots: multifunctional nanoplatforms for anticancer therapy, J. Mater. Chem. B., 5 (2017) 6471.

[42] Kelarakis A. From highly graphitic to amorphous carbon dots: A critical review. MRS Energy Sustain, 1 (2014) 1.

[43] Kaur M., Kaur M., Sharma, V.K. Nitrogen-doped graphene and graphene quantum dots: A review onsynthesis and applications in energy, sensors and environment. Adv. Colloid Interface Sci., 259 (2018) 44.

[44] Khojasteh H., Salavati-Niasari M., Safajou H., Safardoust-Hojaghan H. Facile reduction of graphene using urea in solid phase and surface modification by N-doped graphene quantum dots for adsorption of organic dyes. Diam. Relat. Mater., 79 (2017) 133.

[45] Hu C., Liu Y., Yang Y., Cui J., Huang Z., Wang Y., Yang L., Wang H., Xiao Y., Rong J. One-step preparation of nitrogen-doped graphene quantum dots from oxidized debris of graphene oxide. J. Mater. Chem. B., 1 (2013) 39.

[46] Naik J.P., Sutradhar P., Saha M. Molecular scale rapid synthesis of graphene quantum dots (GQDs). J. Nanostructure Chem., 7 (2017) 85.

[47] Jin L., Wang Y., Yan F., Zhang J., Zhong F. The Synthesis and Application of Nitrogen-Doped Graphene Quantum Dots on Brilliant Blue Detection. J. Nanomater., 2019 (2019) 1.

[48] Ojima I., Zuniga E.S., Berger W.T., Seitz J.D. Tumor-targeting drug delivery of new-generation toxoids, Future. Med. Chem., 4 (2012) 33.

[49] Li, D., Wang, X.Z., Yang, L.F., Li, S.C., Hu, Q.Y., Li, X., Zheng, B.Y., Ke, M.R. and Huang, J.D. Size-tunable targeting-triggered nanophotosensitizers based on self-assembly of a phthalocyanine–biotin conjugate for photodynamic therapy. ACS Appl. Mater. Interfaces, 11 (2019) 36435.

[50] Pinhassi R.I., Assaraf Y.G., Farber S., Stark M., Ickowicz D., Drori S., Domb A.J., Livney Y.D. Arabinogalactan− folic acid− drug conjugate for targeted delivery and target-activated release of anticancer drugs to folate receptor-overexpressing cells. Biomacromolecules, 11 (2010) 294.

[51] Kadian S., Manik G. Targeted bioimaging and sensing of folate receptor-positive cancer cells using folic acid-conjugated sulfur-doped graphene quantum dots. Microchim. Acta., 187 (2020) 458.

[52] Hilgenbrink A.R., Low P.S. Folate receptor-mediated drug targeting: from therapeutics to diagnostics. J. Pharm. Sci., 94 (2005) 2135.

[53] Choi Y., Thomas T., Kotlyar A., Islam M.T., Baker J.R. Synthesis and functional evaluation of DNA-assembled polyamidoamine dendrimer clusters for cancer cell-specific targeting. Chem. Biol., 12 (2005)35.

[54] Managa M., Ngoy B.P., Nyokong, T. Photophysical properties and photodynamic therapy activity of a meso-tetra (4-carboxyphenyl) porphyrin tetramethyl ester–graphene quantum dot conjugate. New J. Chem., 43 (2019) 4518.

[55] Li D., Diao J., Wang D., Liu J., Zhang J. Design, synthesis and biological evaluation of folate-porphyrin: A new photosensitizer for targeted photodynamic therapy. J. Porphyr. Phthalocyanines, 14 (2010) 547.

[56] Purushothaman B., Choi J., Park S., Lee J., Samson A.A.S., Hong, S., Song, J.M. Biotin-conjugated PEGylated porphyrin self-assembled nanoparticles co-targeting mitochondria and lysosomes for advanced chemo-photodynamic combination therapy. J. Mater. Chem. B., 7 (2019) 65.

[57] Managa M., Achadu O.J., Nyokong, T. Photophysical studies of graphene quantum dots-Pyrene-derivatized porphyrins conjugates when encapsulated within Pluronic F127 micelles. Dyes Pigm., 148 (2018) 405.

[58] Santos C.I., Rodríguez-Pérez L., Gonçalves G., Dias C.J., Monteiro F., Faustino M.D.A.F., Vieira S.I., Helguero L.A., Herranz M.A., Martin N., Neves, M.G.P. Enhanced Photodynamic Therapy Effects of Graphene Quantum Dots Conjugated with Aminoporphyrins. ACS. Appl. Nano. Mater., 4 (2021) 13079.

[59] Menilli, L., Monteiro A.R., Lazzaratto, S., Morais, F.M.P., Gomes, A.T.P.C, Moura, N.M.M., Fateixa, S., Faustino, M.A.F., Neves, M.G.P.M.S., Trindade, T., Miolo, G. Graphene oxide and graphene quantum dots as delivery systems of cationic porphyrins: Photo-antiproliferative activity evaluation towards T24 human bladder cancer cells. Pharmaceutics, 13 (2021) 1512.

[60] Cao, Y., Dong, H., Yang, Z., Zhong, X., Chen, Y., Dai, W., Zhang, X. Aptamer-conjugated graphene quantum dots/porphyrin derivative theranostic agent for intracellular cancer-related microRNA detection and fluorescence-guided photothermal/photodynamic synergetic therapy. ACS App. Mater. Interfaces, 9 (2017) 159.

[61] Jensen, T.J., Vicente, M.G.H., Luguya, R., Norton, J., Fronczek, F.R., Smith, K.M. Effect of overall charge and charge distribution on cellular uptake, distribution and phototoxicity of cationic porphyrins in HEp2 cells. J. Photochem. Photobiol. B: Biol., 100(2010) 100.

[62] Achadu, O.J., Nyokong, T. Interaction of graphene quantum dots with 4-acetamido-2,2,6,6-tetramethylpiperidine-oxyl free radicals: A spectroscopic and fluorimetric study, J. Fluoresc. 26 (2016) 283.

[63] Nene, L.C., Managa, M., Nyokong, T. Photo-physicochemical properties and in vitro photodynamic therapy activity of morpholine-substituted Zinc(II)-Phthalocyanines π-π stacked on biotinylated graphene quantum dots, Dyes Pigm., 165 (2019) 488.

[64] Feng, S., Pan, J., Li, C., Zheng, Y. Folic acid-conjugated nitrogen-doped graphene quantum dots as a fluorescent diagnostic material for MCF-7 cells. Nanotechnology, 31(2020)135701.

[65] Wang, A., Song, J., Jia, D., Yu, W., Long, W., Song, Y., Cifuentes, M.P., Humphrey, M.G., Zhang, L., Shao, J., Zhang, C. Functionalization of reduced graphene oxide with axially-coordinated metal-porphyrins: Facile syntheses and temporally-dependent nonlinear optical properties, Inorg. Chem. Front., 3 (2016) 296–305.

[66] Dolušić, E., Ngo, H.T., Maes, W., Dehaen, W. Efficient synthesis of aryldipyrromethanes in water and their application in the synthesis of corroles and dipyrromethenes. Arkivoc, 10 (2007) 307.

[67] Nakamura Y., Aratani, N., Furukawa, K., Osuka, A. Synthesis and characterizations of free base and Cu(II) complex of a porphyrin sheet, Tetrahedron, 64 (2008) 11433.

[68] Arnold, D.P., Blok, J. The coordination chemistry of tin porphyrin complexes, Coord. Chem. Rev., 248 (2004) 299.

[69] Duerr, K., Troeppner, O., Olah, J., Li, J., Zahl, A., Drewello, T., Jux, N., Harvey, J.N. and Ivanović-Burmazović, I. Solution behavior of iron (III) and iron (II) porphyrins in DMSO and reaction with superoxide. Effect of neighboring positive charge on thermodynamics, kinetics and nature of iron-(su) peroxo product. Dalton Trans., 41(2012) 546.

[70] Atwater, B.W. Substituent effects on the excited-state properties of platinummeso-tetraphenylporphyrins. J. Fluoresc., 2 (1992) 237.

[71] Giovannetti, R. The Use of Spectrophotometry UV-Vis for the Study of Porphyrins. in Macro To Nano Spectroscopy, ed. J. Uddin, Intech, Open Science. 6 (2012) 92.

[72] Reddy, M.V.H., Al-Shammari, R.M., Al-Attar, N., Lopez, S., Keyes, T.E., Rice, J.H. Optical properties of porphyrin – graphene oxide composites, Proc. SPIE., 9172 (2014) 91720.

[73] Lee, K.S., El-Sayed, M.A. Gold and silver nanoparticles in sensing and imaging: Sensitivity of plasmon response to size, shape, and metal composition, J. Phys. Chem. B., 110 (2006) 19220.

[74] Majles Ara, M.H., Dehghani, Z., Sahraei, R., Daneshfar, A., Javadi, Z., Divsar, F. Diffraction patterns and nonlinear optical properties of gold nanoparticles, J. Quant. Spectrosc. Radiat. Transfer., 113 (2012) 366.

[75] Soy R.C., Babu, B., Oluwole, D.O., Nwaji, N., Oyim, J., Amuhaya, E., Prinsloo, E., Mack, J., Nyokong, T. Photophysicochemical properties and photodynamic therapy activity of chloroindium(III) tetraarylporphyrins and their gold nanoparticle conjugates, J. Porphyrins Phthalocyanines, 23 (2019) 34.

[76] Calik, M., Sharapa, D., Soni, H.R., Zehetmaier, P.M, Rager, S., Auras, F., Jakowetz, A.C., Görling, A., Clark, T., Bein, T. Enforcing extended porphyrin J-Aggregate stacking in covalent organic frameworks, J. Am. Chem. Soc., 140 (2018) 16544.

[77] Takayama, S.J., Ukpabi, G., Murphy, M.E.P., Mauk, A.G. Electronic properties of the highly ruffled heme bound to the heme degrading enzyme IsdI. Proceedings of the National Academy of Sciences., 108 (2011) 13071.

[78] Souza, T.G.F., Ciminelli, V.S.T., Mohalleni, N.D.S. A comparison of TEM and DLS methods to characterize size distribution of ceramic nanoparticles. J. Phys. Conf. Ser., 733 (2016) 012039.

[79] Patrick, H., Tobias, P., Florian, A., Andre, P., Johannes, V., Daniel, V., Gregor, W., Wolfang, VR., Joachim, O., Stefan, W. Exploration of MOF nanoparticles sizes using various physical characterization methods - is what you measure what you get?, Cryst Eng. Comm., 23 (2016) 4359.

[80] Ostolska, I., Wisniewska, M. Application of the zeta potential measurements to explanation of colloidal Cr2O3 stability mechanism in the presence of the ionic polyamino acid, Colloid Polym. Sci., 292 (2014) 2453.

[81] Melendrez, M.F., Gardenas, G., Arbiol, J. Synthesis and characterization of gallium coolodial nanoparticles. J. Coll. Interf. Sci., 346 (2010) 279.

[82] Jyoti, K., Baunthiyal, M., Singh, A. Characterization of silver nanoparticles synthesized using *Urtica dioica* Linn. leaves and their synergistic effects with antibiotics. J. Radiat. Res. Appl. Sci., 9 (2016) 217.

[83] Flower, G.L., Latha, S.V, Rao, K.V.**.** Novel characterization of nanosilver fluid through ultrasonic studies supported by UV–Vis spectroscopy, DLS and TEM studies**.** J. Mol. Liq., 221 (2016)333-338.

[84] Gurunathan, S., Han, J.W., Kwon, D.N., Kim, J.H. Enhanced antibacterial and anti-biofilm activities of silver nanoparticles against Gram-negative and Gram-positive bacteria**.** Nanoscale Res. Lett., 9 (2014)1-7.

[85] Danaei, M., Dehghankhold, M., Ataei, S., Hasanzadeh davarani, F., Javanmard, R., Dokhani, A., Khorasani, S., Mozafari, M.R. Impact of particle size and polydispersity index on the clinical applications of lipidic nanocarrier systems. Pharmaceutics*,* 10 (2018) 57.

[86] Shirashi, M., Swaraj, S., Takenobu, T., Iwasu, Y., Ata, M., Unger, W.E.S. Spectroscopic characterization of single-walled carbon nanotubes carrier-doped by encapsulation of TCNQ, Phy.Rev., 71 (2005) 125419.

[87] Smith, M., Scudeiro, L., Espinal, J., McEwen, J.S., Gracia-Perez, M. Improving the deconvolution and interpretation of XPS spectra from chars by ab initio calculations, Carbon, 110 (2016) 155.

[88] Kadian, S., Manik, G., KalKal, A., Singh, M., Chauhan, R.P. Effect of sulfur doping on fluorescence and quantum yield of graphene quantum dots: an experimental and theoretical investigation, Nanotechnology, 30 (2019) 435704.

[89] Jin, L., Wang, Y., Yan, F., Zhang, J., Zhong, F. The Synthesis and Application of Nitrogen-Doped Graphene Quantum Dots on Brilliant Blue Detection, J. Nanomater., 2019 (2019) 1–9.

[90] Kuo, W.S, Chang, C.Y., Huang, K.S., Liu, J.C., Shao, Y.T., Yang, C.H., Wu, P.C. Amino-functionalized nitrogen-doped graphene-quantum-dot-based nanomaterials with nitrogen and amino-functionalized group content dependence for highly efficient two-photon bioimaging, Int. J. Mol. Sci., 21 (2020) 2939.

[91] Kang, S., Jeong, Y.K., Jung, K.H., Son, Y., Kim, W.R., Ryu, J.H., Kim, K.M. One-step synthesis of sulfur-incorporated graphene quantum dots using pulsed laser ablation for enhancing optical properties, Opt. Express, 28 (2020) 21659.

[92] Shaker, M., Riahifar, R., Li, Y. A review on the superb contribution of carbon and graphene quantum dots to electrochemical capacitors' performance: Synthesis and application, Flat Chem., 22 (2020) 100171.

[93] Jin, L., Wang, Y., Yan, F., Zhang, J., Zhong, F. The Synthesis and Application of Nitrogen-Doped Graphene Quantum Dots on Brilliant Blue Detection, J. Nanomater., 2019 (2019) 1–9.

[94] Morisue, M., Ueno, I., Nakanishi, T., Matsui, T., Sasaki, S., Shimizu, M., Matsui, J., Hasegawa, Y. Amorphous porphyrin glasses exhibit near-infrared excimer luminescence. RSC Adv., 7(2017) 22679.

[95] Alves, Z., Nunes, C., Ferreira, P. Unravelling the role of synthesis conditions on the structure of zinc oxide-reduced graphene oxide nanofillers. Nanomaterials, 11 (2021) 2149.

[96] Nikolova, V. and Galabov, B. Theoretical vs. experimental IR frequency shifts upon π-hydrogen bonding: complexes of substituted phenols with hexamethylbenzene, Contributions. Sec. Nat. Math. Biotech. Sci., 38 (2017) 33.

[97] Tang, L., Ji, R., Li, X., Teng, K.S. and Lau, S.P. Energy-level structure of nitrogen-doped graphene quantum dots. J. Mater. Chem. C., 1(2013) 4908.

[98] Bajjou, O., Khenfouch, M., Baïtoul, M., Mothudi, B., Dhlamini, M., Faulques, E. Maaza, M. Vibrational and optical properties of Meso-tetrakis (4-phenylsulfonica-acid) porphyrin decorated with graphene oxide. Mater.Sci. Eng., 186 (2017) 0012003.

[99] Kudin, K.N., Ozbas, B., Schniepp, H.C., Prud'Homme, R.K., Aksay, I.A., Car, R. Raman spectra of graphite oxide and functionalized graphene sheets. Nano. Lett., 8 (2008) 36.

[100] Batakliev, T., Petrova-Doycheva, I., Angelov, V., Georgiev, V., Ivanov, E., Kotsilkova, R., Casa, M., Cirillo, C., Adami, R., Sarno, M., Ciambelli, P. Effects of graphene nanoplatelets and multiwall carbon nanotubes on the structure and mechanical properties of poly(lactic acid) composites: a comparative study, Appl. Sci., 9 (2019) 469.

[101] Singh, D.K., Iyer, P.K., Giri, P.K. Diameter dependence of interwall separation and strain in multiwalled carbon nanotubes probed by X-ray diffraction and Raman scattering studies, Diam. Relat. Mater., 19 (2010) 1281.

[102] Kim, S., Hee Shin, D., Oh Kim, C., Seok Kang, S., Sin Joo, S., Choi, S.H., Won Hwang, S., Sone, C. Size-dependence of Raman scattering from graphene quantum dots: interplay between shape and thickness, Appl. Phys. Lett., 102 (2013) 53108.

[103] A.M. Brouwer. Standards for photoluminescence quantum yield measurements in solution (IUPAC Technical Report). Pure Appl. Chem., 83 (2011) 2213.

[104] De Simone, B.C., Mazzone, G., Russo, N., Sicilia, E., Toscano, M. Metal atom effect on the photophysical properties of Mg (II), Zn (II), Cd (II), and Pd (II) tetraphenylporphyrin complexes proposed as possible drugs in photodynamic therapy. Molecules, 22 (2017) 1093.

[105] Ohulchanskyy, T.Y., Donnelly, D.J., Detty, M.R., Prasad, P.N. Heteroatom substitution induced changes in excited-state photophysics and singlet oxygen generation in chalcogenoxanthylium dyes: Effect of sulfur and selenium substitutions. J. Phys. Chem. B., 108 (2004) 8668.

[106] Goto, S., Nitta, Y., Decarli, N.O., de Sousa, L.E., Stachelek, P., Tohnai, N., Minakata, S., de Silva, P., Data, P., Takeda, Y. Revealing the internal heavy chalcogen atom effect on the photophysics of the dibenzo [a, j] phenazine-cored donor–acceptor–donor triad. J. Mater. Chem. C., 9 (2021) 13942.

[107] Stallivieri, A., Colombeau, L., Jetpisbayeva, G., Moussaron, A., Myrzakhmetov, B., Arnoux, P., Acherar, S., Vanderesse, R., Frochot, C. Folic acid conjugates with photosensitizers for cancer targeting in photodynamic therapy: Synthesis and photophysical properties. Bioorg. Med. Chem., 25 (2017) 1.

[108] Sibani, S.A., McCarron, P.A., Woolfson, A.D., Donnelly, R.F. Photosensitiser delivery for photodynamic therapy. Part 2: systemic carrier platforms. Expert Opin. Drug Deliv., 5 (2008) 1241.

[109] Nene, L.C., Buthelezi, K., Prinsloo, E., Nyokong, T. The in vitro photo-sonodynamic combinatorial therapy activity of cationic and zwitterionic phthalocyanines on MCF-7 and HeLa cancer cell lines. J. Photochem. Photobiol. A: Chem,. 432 (2022) 114116.

[110] Maziere, J.C., Santus, R., Morliere, P., Reyftmann, J.P., Candide, C., Mora, L., Salmon, S., Maziere, C., Gatt, S., Dubertret, L. Cellular uptake and photosensitizing properties of anticancer porphyrins in cell membranes and low and high density lipoproteins. J. Photochem. Photobiol. B: Biol., 6 (1990) 61.

[111] Ren, W.X., Han, J., Uhm, S., Jang, Y.J., Kang, C., Kim, J.H., Kim, J.S. Recent development of biotin conjugation in biological imaging, sensing, and target delivery. Chem. Comm., 51 (2015) 10403.

[112] Y. Cao, H. Dong, Z. Yang, X. Zhong, Y. Chen, W. Dai, X. Zhang. Aptamer- conjugated graphene quantum dots/porphyrin derivative theranostic agent for intracellular cancer-related MicroRNA detection and fluorescence-guided photothermal/photodynamic synergetic therapy. ACS Appl. Mater. Interfaces, 9 (2017) 159.

Appendix

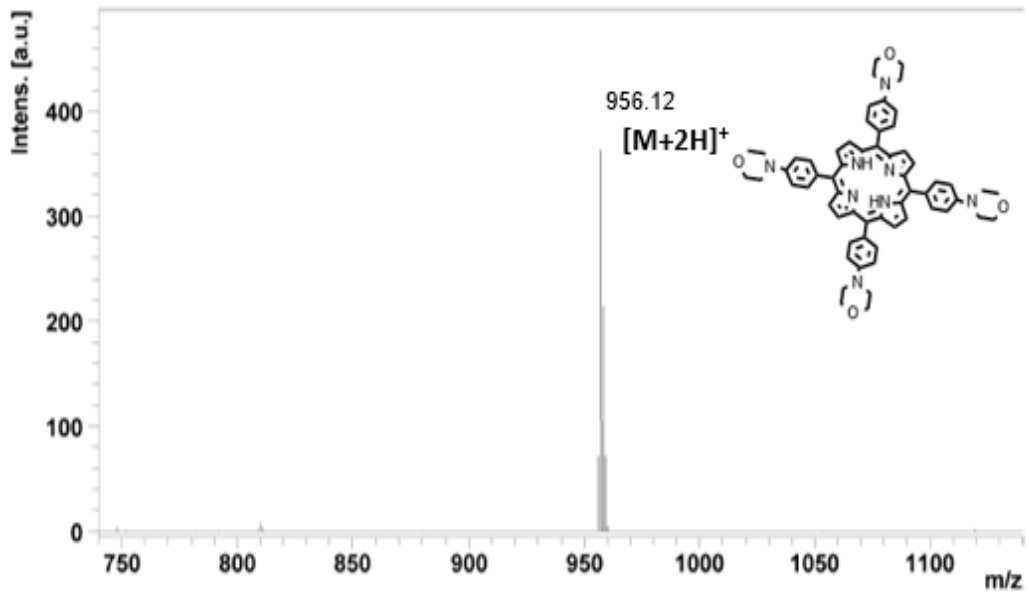

Fig. A1 MATLI-TOF mass spectra of complex **1**

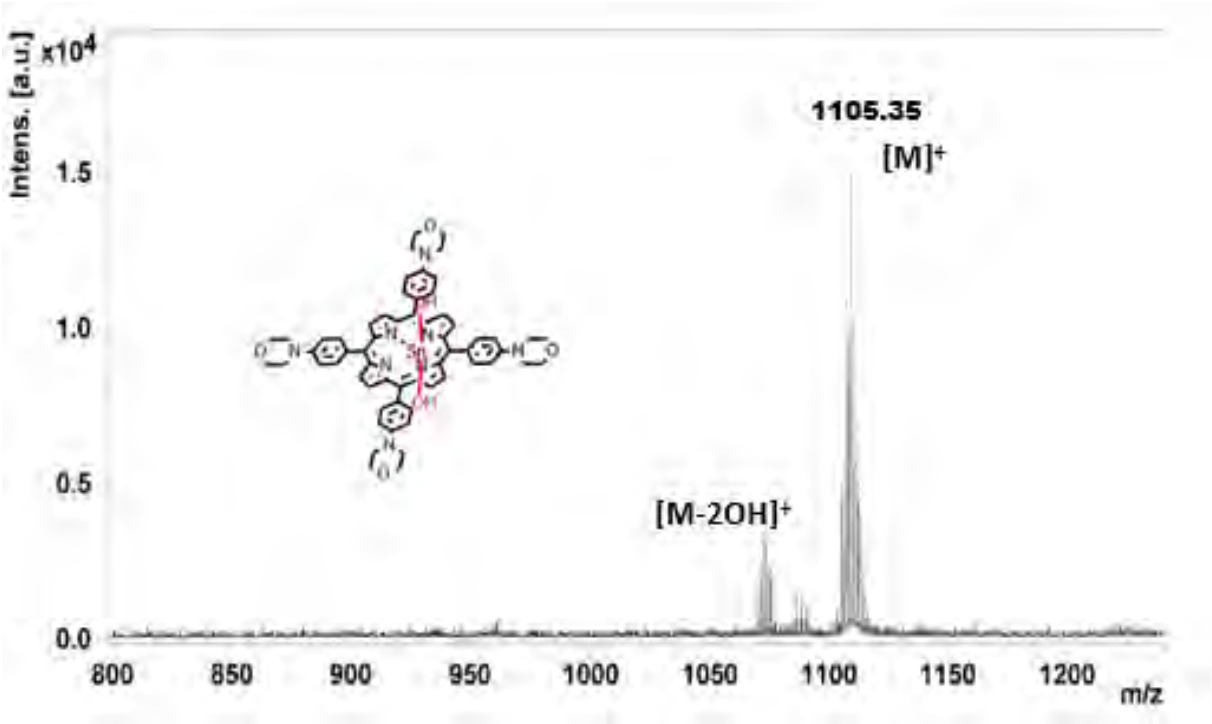

Fig. A2 MALTI-TOF mass spectra of complex **2**

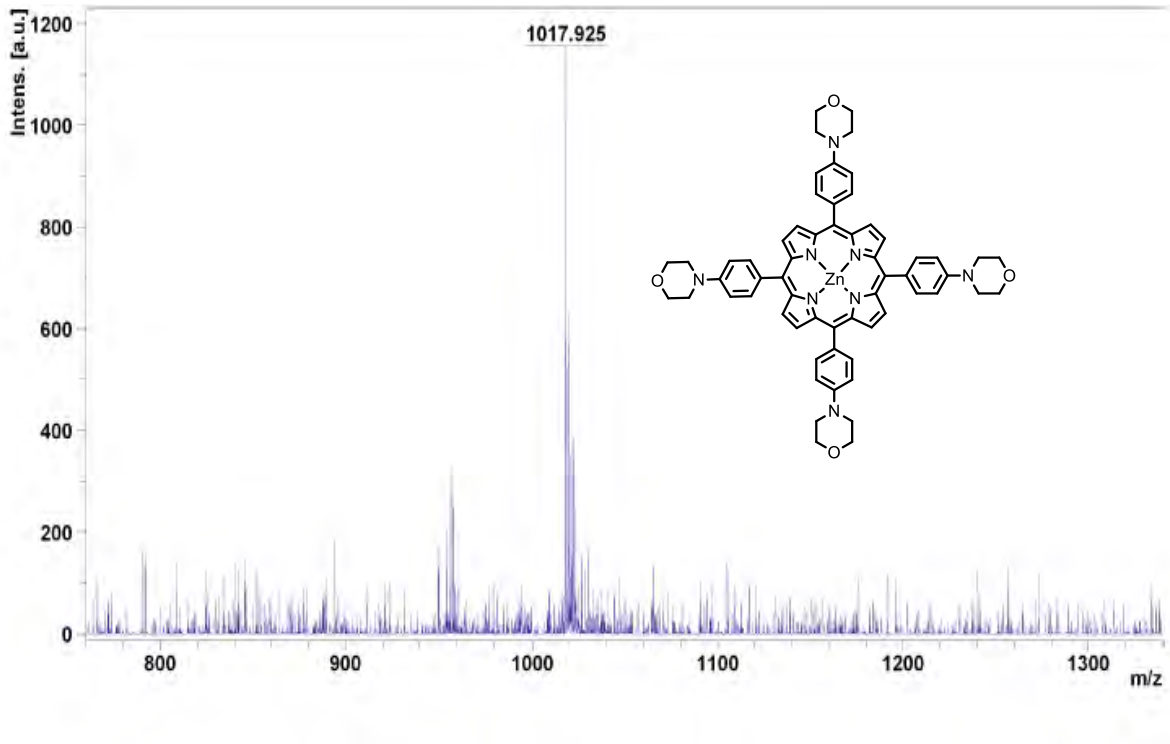

Fig. A3 MALTI-TOF mass spectral of complex **3**

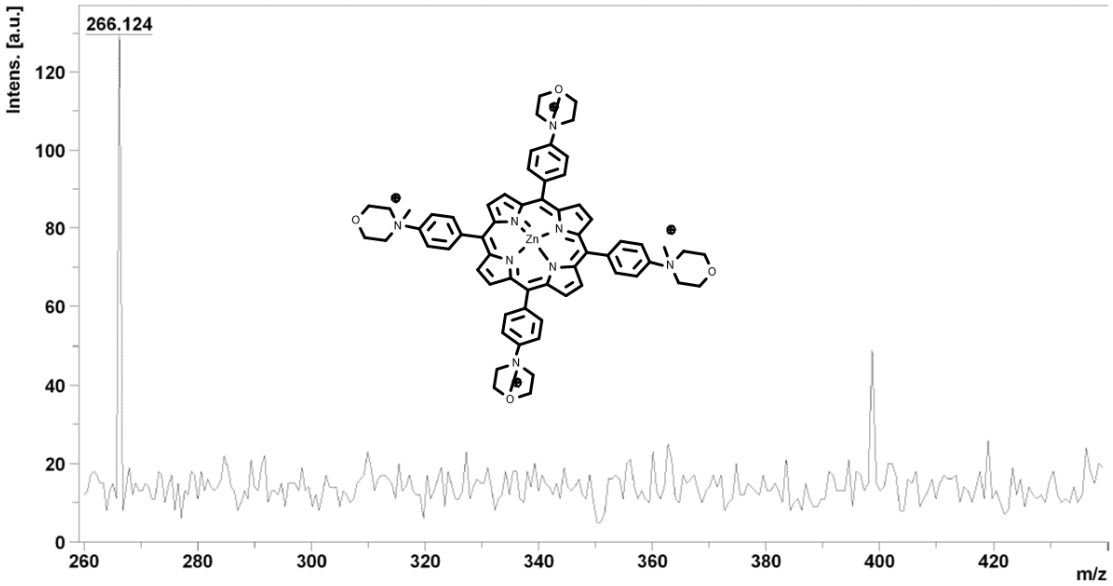

Fig. A4 MALTI-TOF mass spectral of complex **3Q**

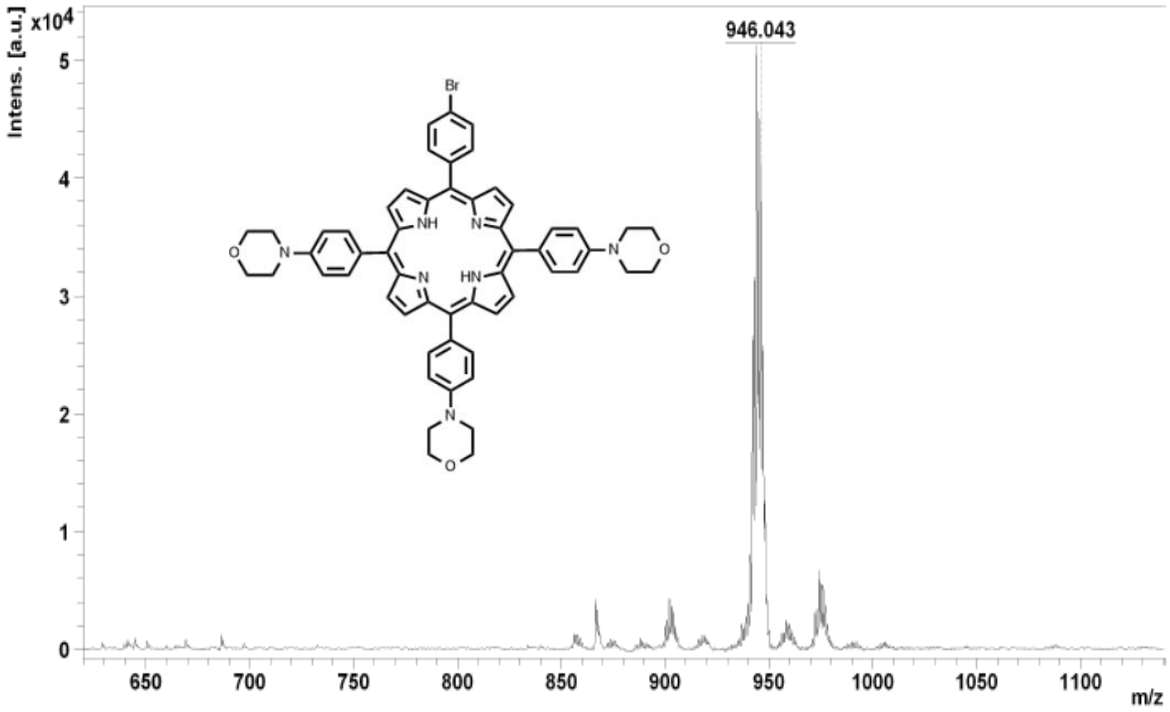

Fig. A5 MALTI-TOF mass spectral of complex **4**

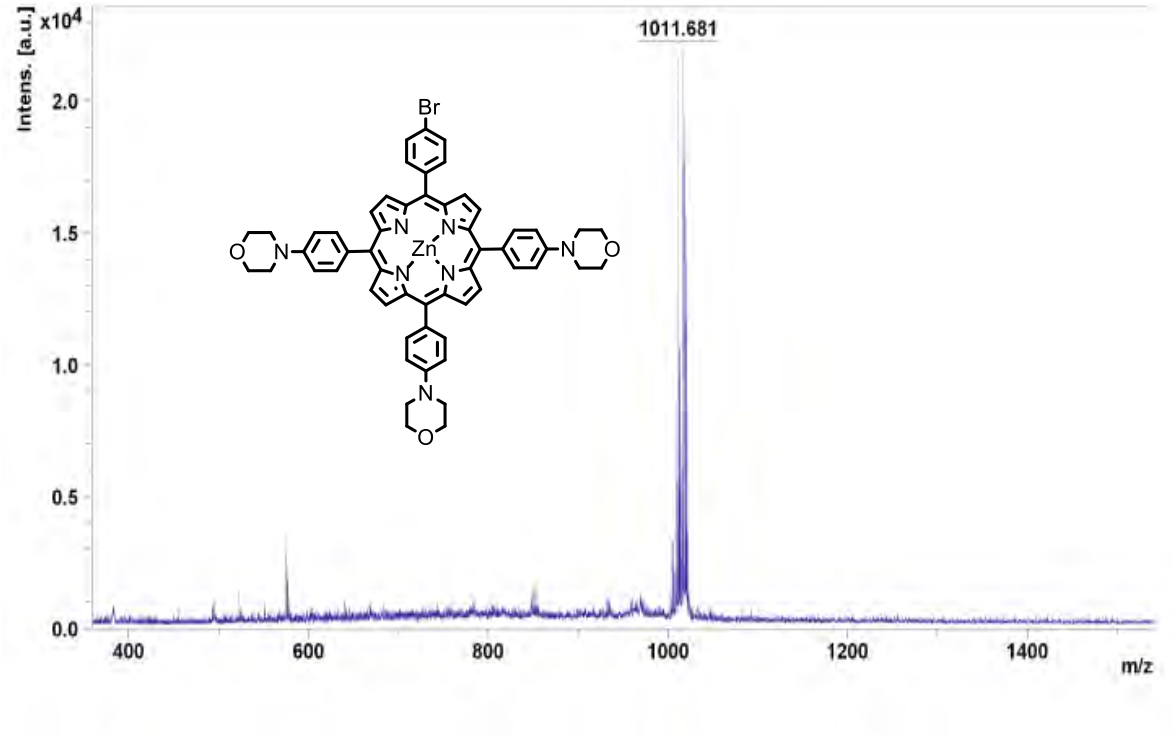

Fig. A6 MALTI-TOF mass spectral of complex **5**

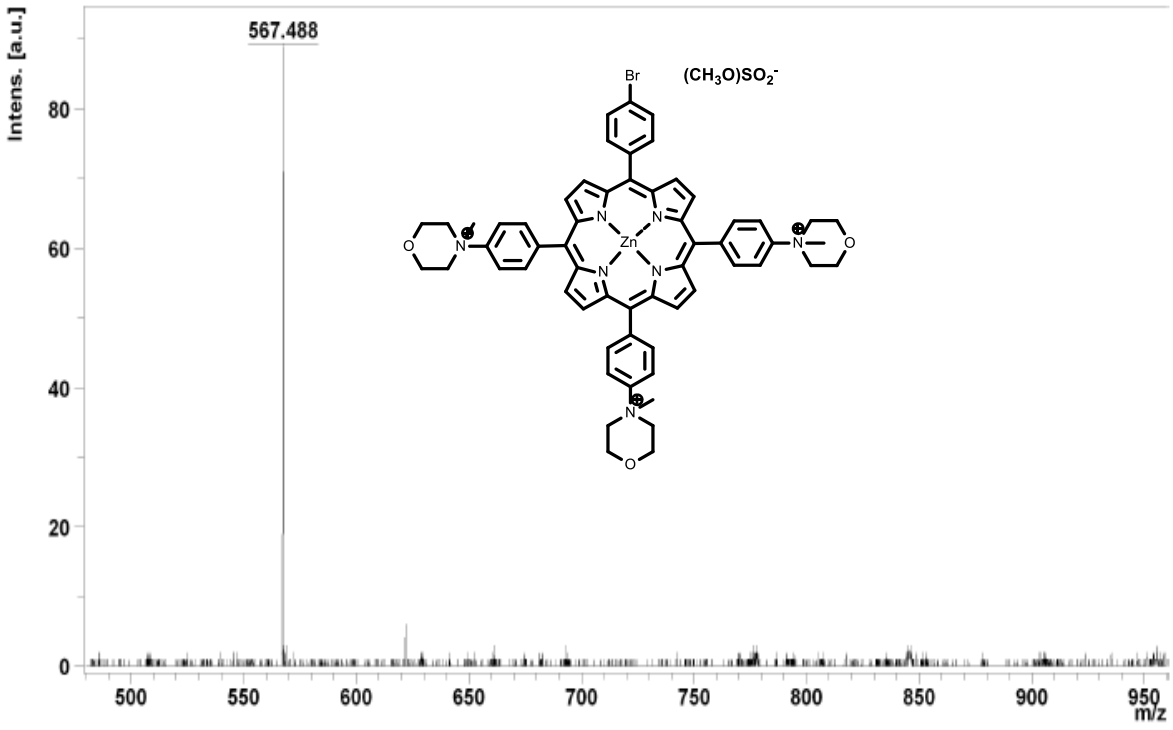

Fig. A7 MALTI-TOF mass spectral of complex **5Q**

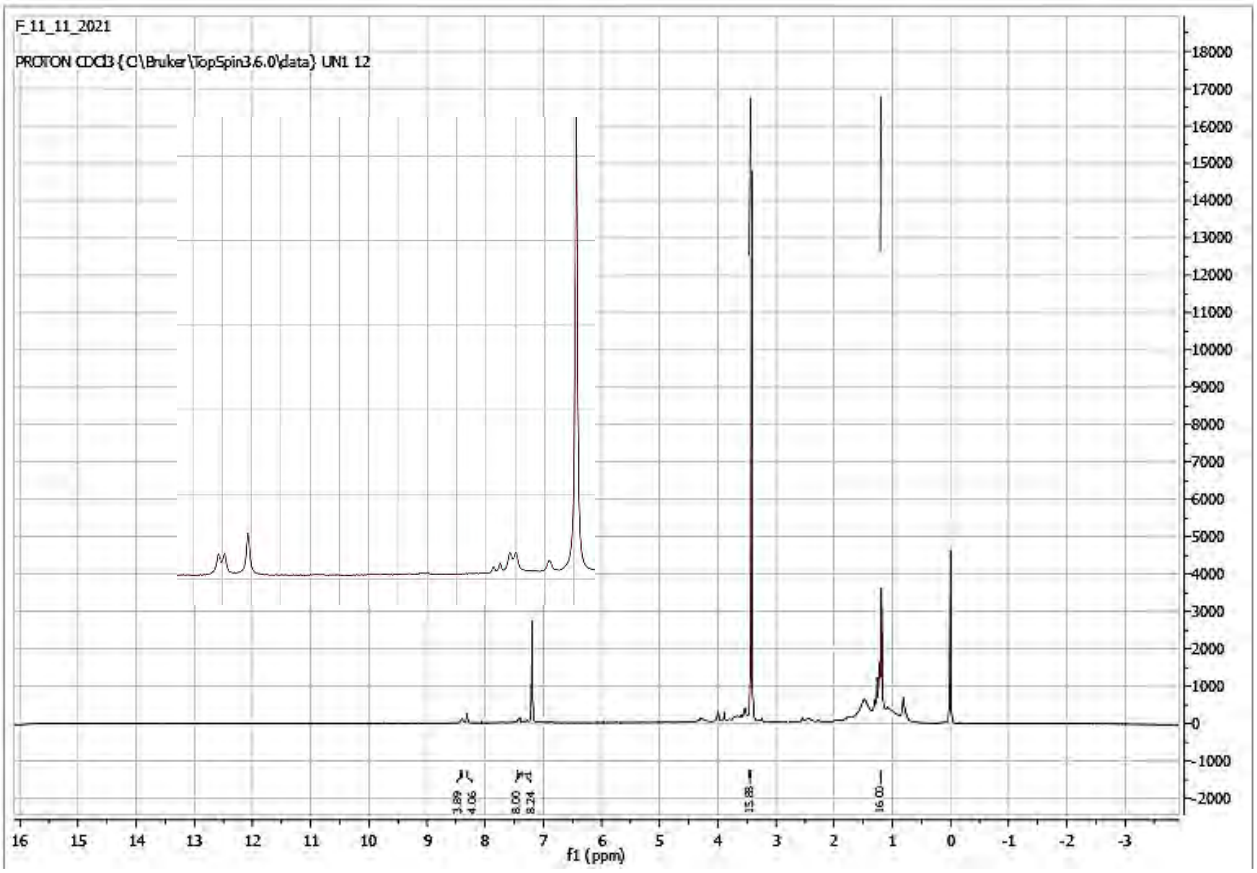

Fig. A8 ^{1}H-NMR spectra of complex **1** in $CDCl_3$

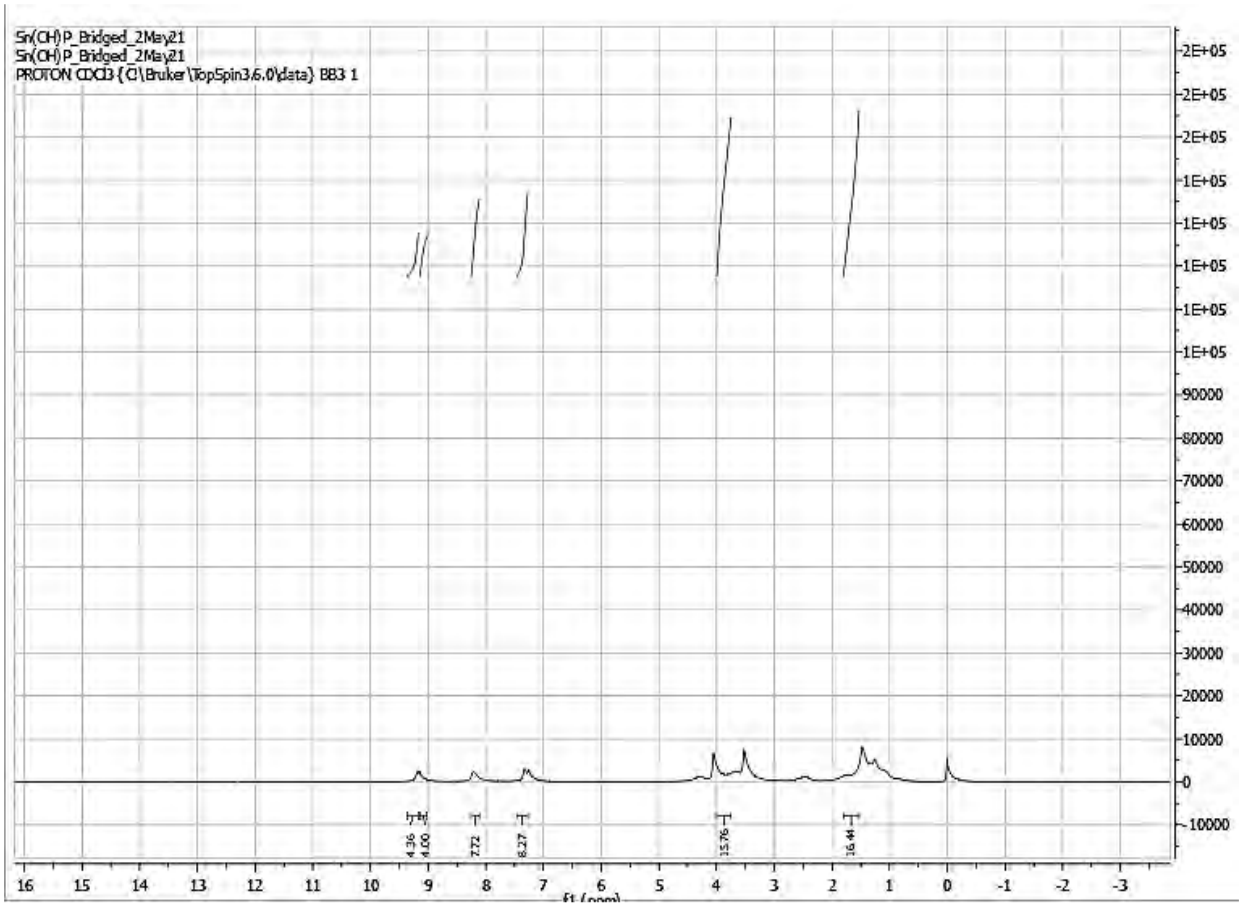

Fig. A9 ^{1}H-NMR spectra of complex **2** in $CDCl_3$

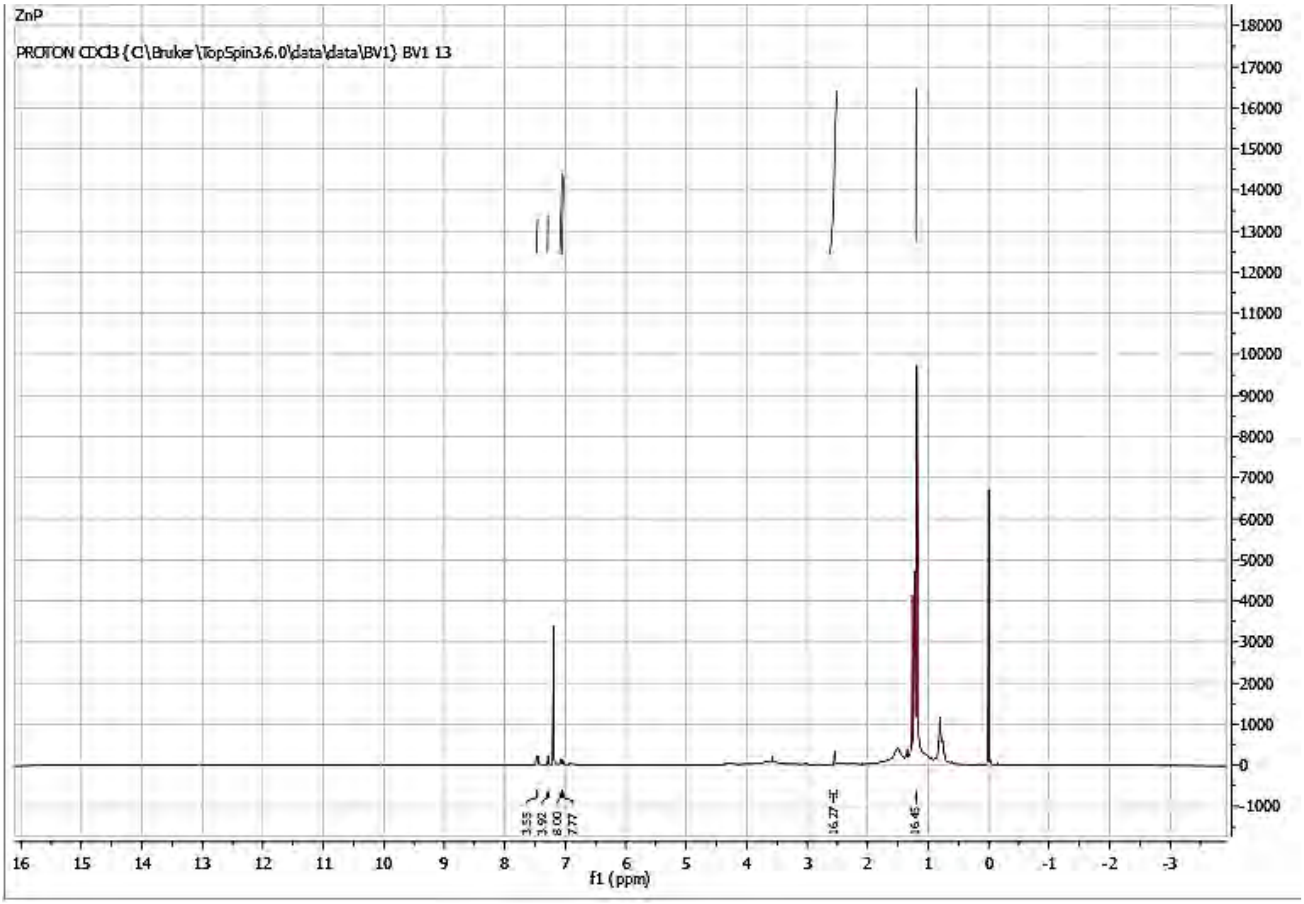

Fig. A10 ^{1}H-NMR spectra of complex **3** in $CDCl_3$

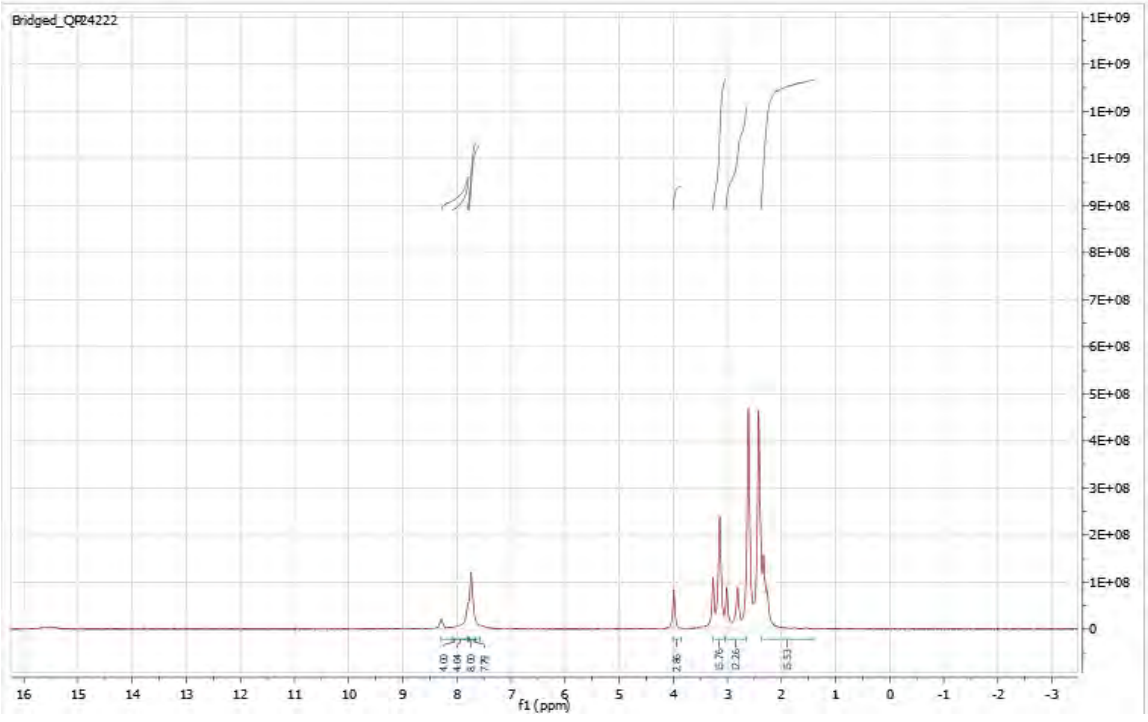

Fig. A11 ^{1}H-NMR spectra of complex **3Q** in DMF

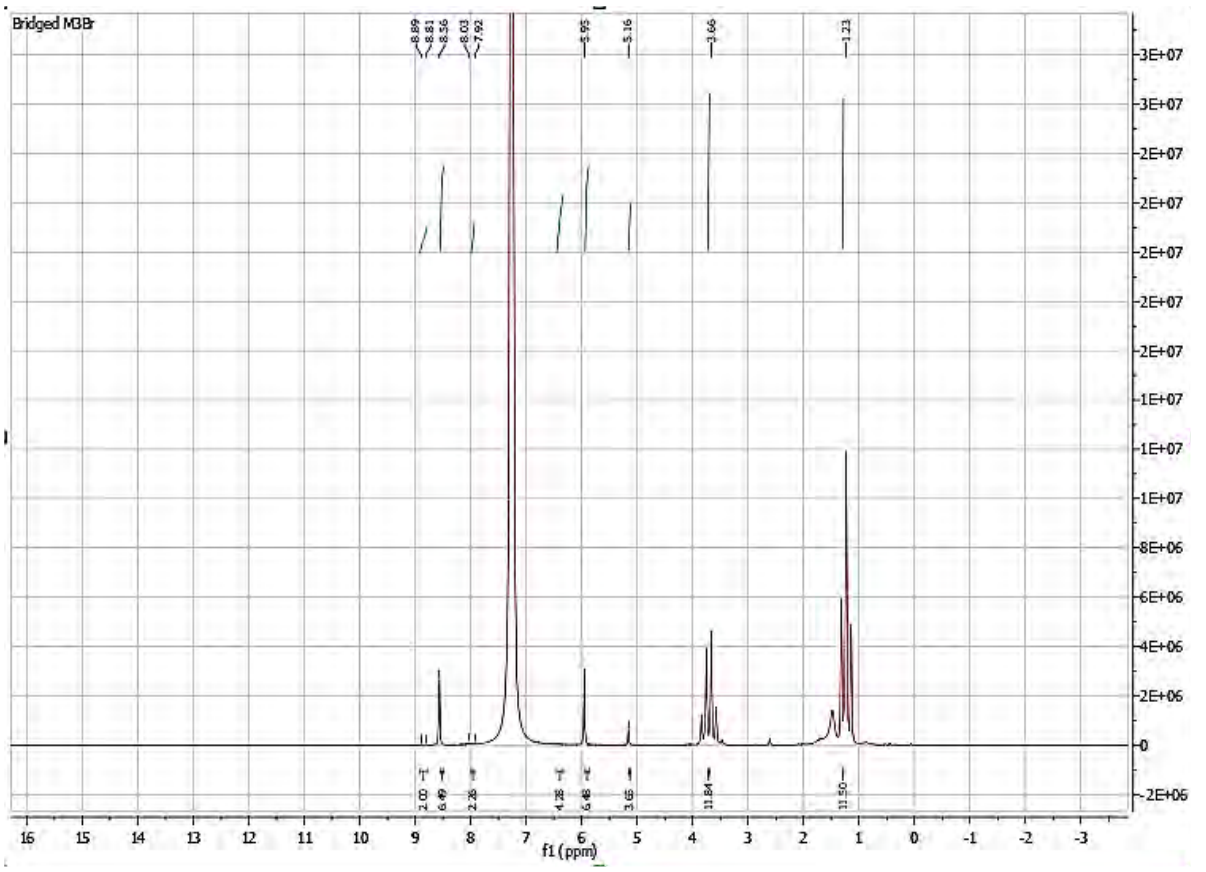

Fig. A12 ^{1}H-NMR spectra of complex **4** in $CDCl_3$

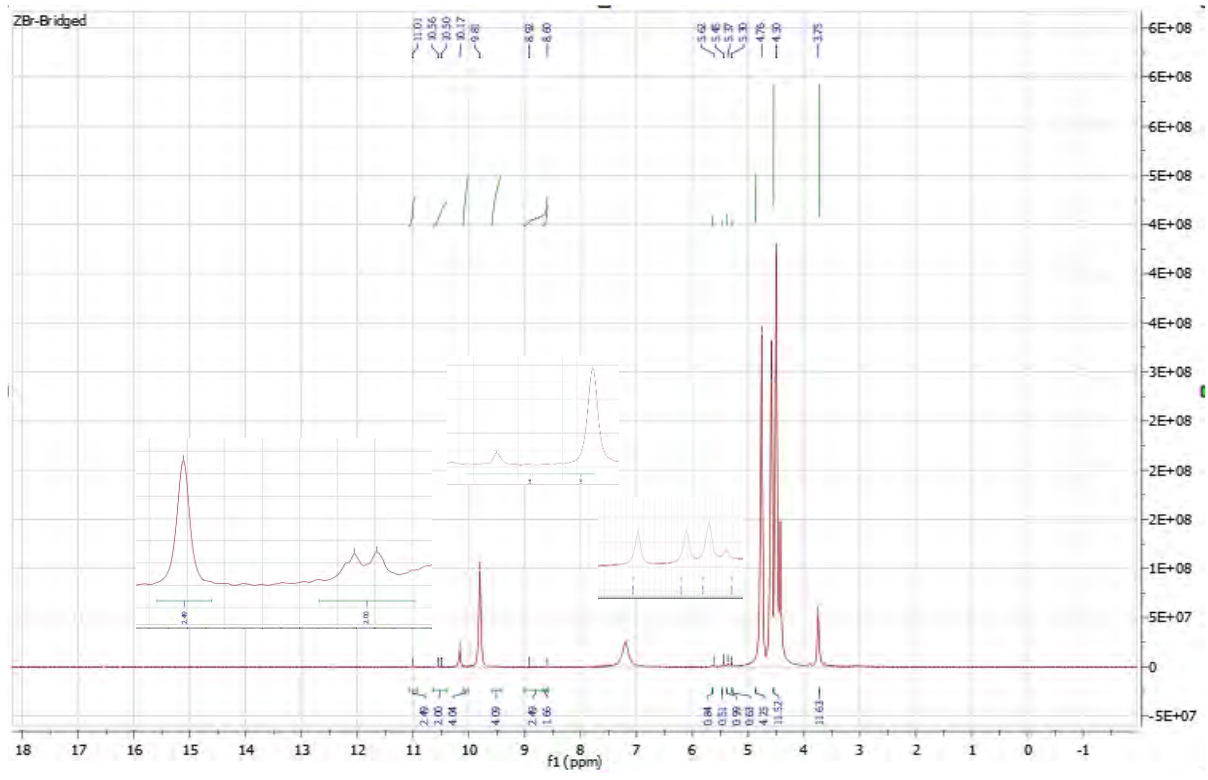

Fig. A13 ^{1}H-NMR spectra of complex **5** in $CDCl_3$

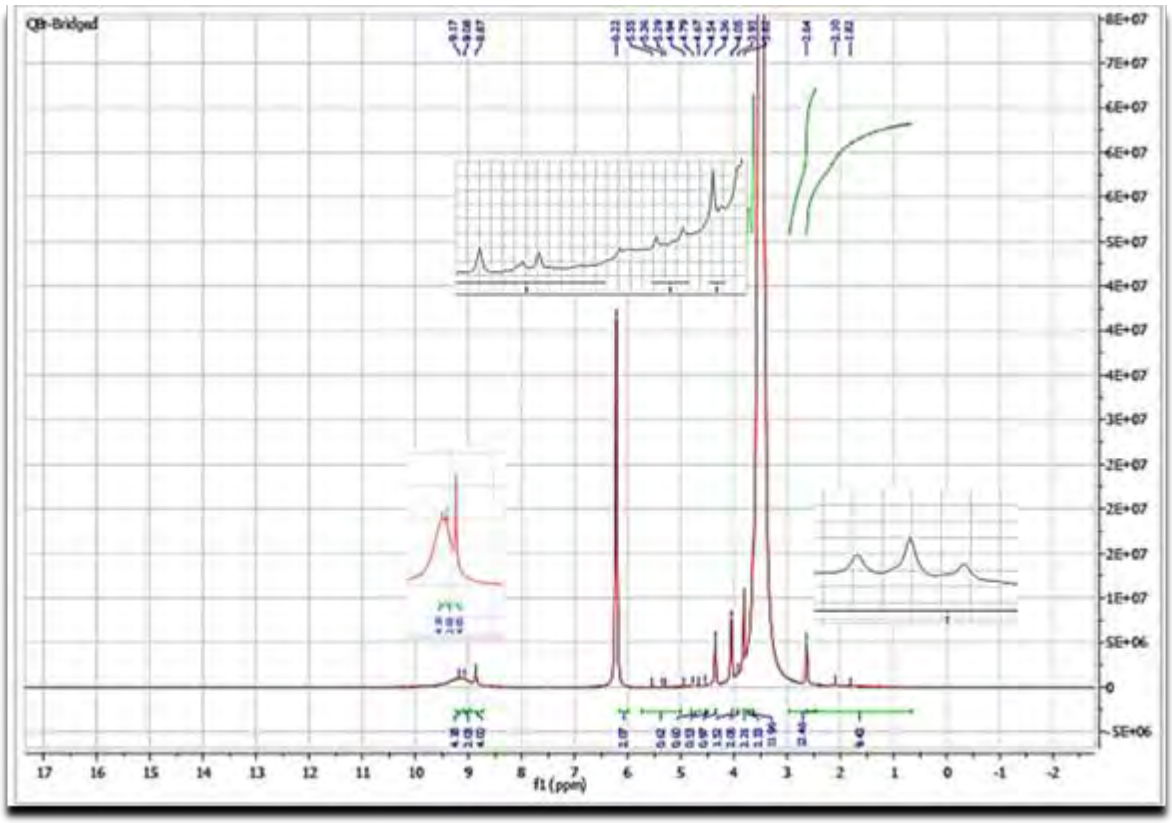

Fig. A14 ^{1}H-NMR spectra of complex **5Q** in DMSO

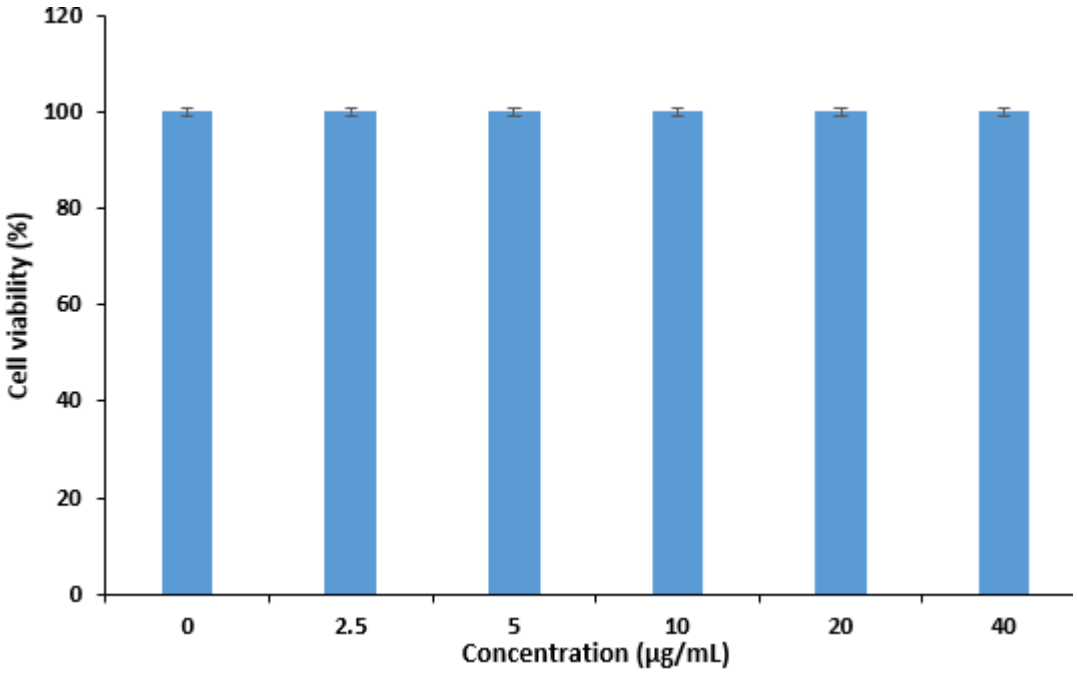

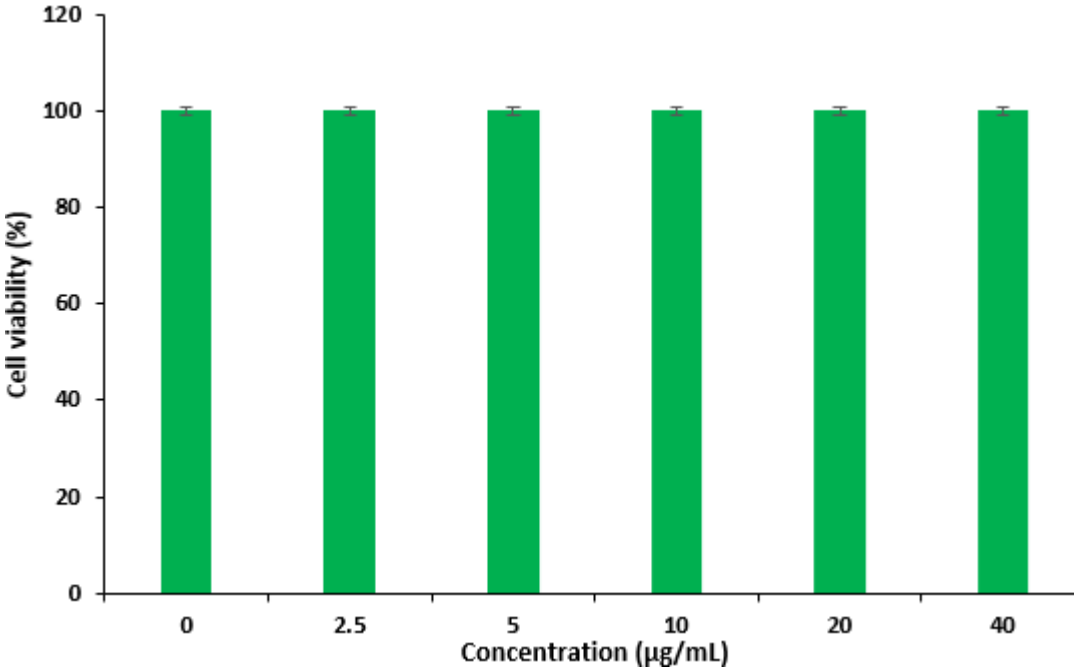

Fig. A15 Histograms showing (A) dark toxicity and (B) PDT activity of 1% DMSO in cells in the absence of photosensitizer.